Summer 7-2018

Integrated Geophysical Analysis in the Northeastern Gulf of Mexico

Mei Liu
University of Nebraska-Lincoln, mliu24@huskers.unl.edu

INTEGRATED GEOPHYSICAL ANALYSIS IN THE NORTHEASTERN GULF OF MEXICO

By

Mei Liu

A THESIS

Presented to the Faculty of

The Graduate College at the University of Nebraska

In Partial Fulfillment of Requirements

For the Degree of Master of Science

Major: Earth and Atmospheric Sciences

Under the Supervision of Professor Irina Filina

Lincoln, Nebraska

July, 2018

Integrated Geophysical Analysis in the Northeastern Gulf of Mexico

Mei Liu, M.S.

University of Nebraska, 2018

Advisor: Irina Filina

The formation of the Gulf of Mexico (GoM) relates to the breakup of Pangea and opening of the central Atlantic Ocean. The tectonic history of the basin is still being debated due to lack of geological constraints. This project addresses the crustal architecture in the northeastern GoM from integrative analysis of multiple geophysical datasets to provide constraints for the tectonic reconstruction.

The objectives of this study are: 1) to delineate various tectonic zones (continental and oceanic domains) and map the boundary between them, 2) to derive physical properties of the subsurface rocks, 3) to map the major tectonic structures in the study area, such as the pre-salt basin and the Seaward Dipping Reflectors (SDR) province in continental domain, and segments of an extinct spreading center with associated transform faults in oceanic domain, and 4) to establish the spatial and temporal relations between different tectonic zones and structures.

Three two-dimensional subsurface models were developed in the northeastern GoM by using consistent physical properties for subsurface rocks. Further, spatial analysis

was performed on gravity and magnetic grids, which allowed mapping of various tectonic zones and structures.

As a result of this study, two distinct spreading episodes of GoM formation were identified. The first one, presumably from 160 to 150 Ma, was an ultra-slow spreading event (estimated full spreading rate of 0.9 cm/yr) that produced thin (~5 km) and dense (2.95 g/cc) oceanic crust with fast seismic velocities (~7km/s) and high magnetic susceptibility (0.0075 cgs), most likely composed of gabbro. At ~150 Ma, the spreading center jumped to the south due to a change in location of the Euler pole. The second spreading episode was faster (1.1 cm/yr) and produced thicker crust (up to 9 km) composed of two layers – a basaltic layer (2-4 km thick, Vp = 6-6.5 km/s, density 2.65 g/cc and magnetic susceptibility 0.007 cgs) on top of a gabbroic one. The ridge propagation resulted in the asymmetry of the oceanic domain that needs to be accounted for during tectonic reconstruction.

Dedication

This thesis is firstly dedicated to my parents, Yilin Liu and Guangyu Shao. My mother has taught me how to be an independent woman with courage and love. My father used his patience and intelligence taught me the virtues of persistence. I would like to thank them for providing me the opportunity to study abroad even though they have never been to the U.S. before. I also would like to thank them for always being proud of me. My parents read this thesis over and over again even though they have to rely on a dictionary to understand English. These words could never express my gratitude and thanks to my beloved parents.

This work is also dedicated to my grandparents, the rest of my family, and my friends. It is your kindness, enthusiasm towards life, and love motivated me to be a better person.

Last but not least, this thesis is dedicated to Jesse A. Ash who has accompanied me through every effort of this thesis and provides me endless encouragement.

Acknowledgements

I would like to acknowledge several people have contributed to make this thesis possible. First of all, I would like to thank my advisor, Dr. Irina Filina, for her guidance and mentorship on this project. Her knowledge, patience, and enthusiasm pushed my work to where it is. I would not be able to have this achievement without her kindly assistance. I would also like to acknowledge Dr. Chris Fielding and Dr. Caroline Burberry for serving on my committee. Dr. Mindi Searls who provided a lot of valuable feedback on my work during our weekly meetings.

In addition, I would like thank Dr. Erin Betuel who has provided incredible ideas to inspire me on this project.

Lastly, I would like to acknowledge the UNL Department of Earth and Atmospheric Sciences for the financial support and numerous other professors and students for their kindness support and friendship. Thank you very much!

Table of Contents

List of Figures

List of Tables

CHPATER 1. Introduction to the Study Area

1.1 Motivation for the study

The Gulf of Mexico (GoM; Figure 1) is a semi-enclosed oceanic basin with a total area of about 1.6 million km^2. The GoM initiated during the breakup of Pangea supercontinent and has a very complex formation history with several disputed tectonic phases (Buffler and Sawyer, 1985; Pindell and Keenan, 2009; Hudec et al., 2013; Eddy et al., 2014; Christeson et al., 2014; Nguyen and Mann, 2016; Lundin, 2017). Generally, the major tectonic stages of the GoM are recognized as continental rifting, salt deposition, and seafloor spreading, followed by subsequent subsidence and sedimentation of the passive continental margin (Table 1).

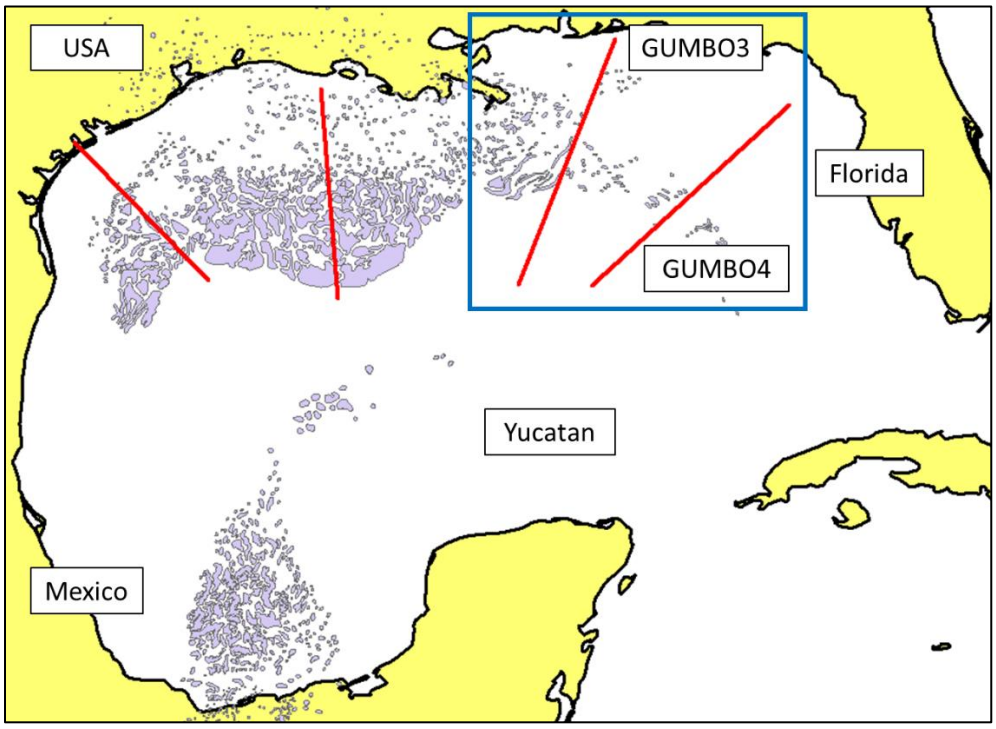

Figure 1. The location of the study area in the northeastern Gulf of Mexico (blue box). Four red lines show the transects from the GUMBO (Gulf of Mexico Basin Opening) seismic refraction experiment (Duncan, 2013). Purple polygons are the Louann salt province in the north and the Campeche salt provinces are in the south.

According to the published models, the continental rifting initiated in the Late Triassic (230 Ma, Pindell and Keenan, 2009; Hudec et al., 2013; Eddy et al., 2014; Christeson et al., 2014; Nguyen and Mann, 2016; Lundin, 2017) and provided the accommodation for deposition of the pre-salt sediments, such as the Eagle Mill Formation in the northern GoM (Pilger, 1981; Warwick, 2017) and the La Boca Formation in Mexico (Bartok, 1993). Thick salt was deposited in a short time interval in the Callovian (~166-163Ma, Salvador, 1991). The presence of multiple complex salt bodies in the sedimentary section obscures seismic imaging and challenges the study of the crustal structures within the basin. The oceanic crust formed in the Jurassic (160-140 Ma, Eddy et al., 2014) during the counterclockwise rotation of the Yucatan crustal block, leaving behind a series of extinct spreading segments offset by transform faults. As the formation of the Gulf of Mexico is closely related to the opening of the central Atlantic Ocean, any tectonic reconstruction of Pangea requires thorough understanding of the GoM's complex history. However, the pre-breakup location of the Yucatan block is still not well constrained. This study aims to provide important constraints for the basin restoration, such as the location of the Seaward Dipping Reflectors (SDRs) and pre-salt sedimentary provinces as they are supposed to match on the conjugate margins.

Many tectonic models have been developed for the GoM (Buffler and Sawyer, 1985; Pindell, 1985; Marton and Buffler, 1994; Kneller and Johnson, 2011; Hudec et al., 2013; Pindell and Keenan, 2009; Christeson et al., 2014; Nguyen and Mann, 2016, Lundin 2017). However, the location of the key tectonic structures, such as the ocean-continent boundary (OCB) and extinct spreading centers with associated transform faults, are still being debated (Figure 2). The published studies shown in Figure 2 were performed based on one or two geophysical methods. For example, Sandwell et al. (2014) and Nguyen and Mann (2016) mapped the tectonic structures based on

satellite gravity. Interpretations of Hudec et al. (2013) are based on seismic data. Pindell et al. (2016) used aeromagnetic data to determine the location of key tectonic structures. This study integrated all publically available geophysical datasets: multiple seismic refraction and reflection surveys, well logs, gravity and magnetic data.

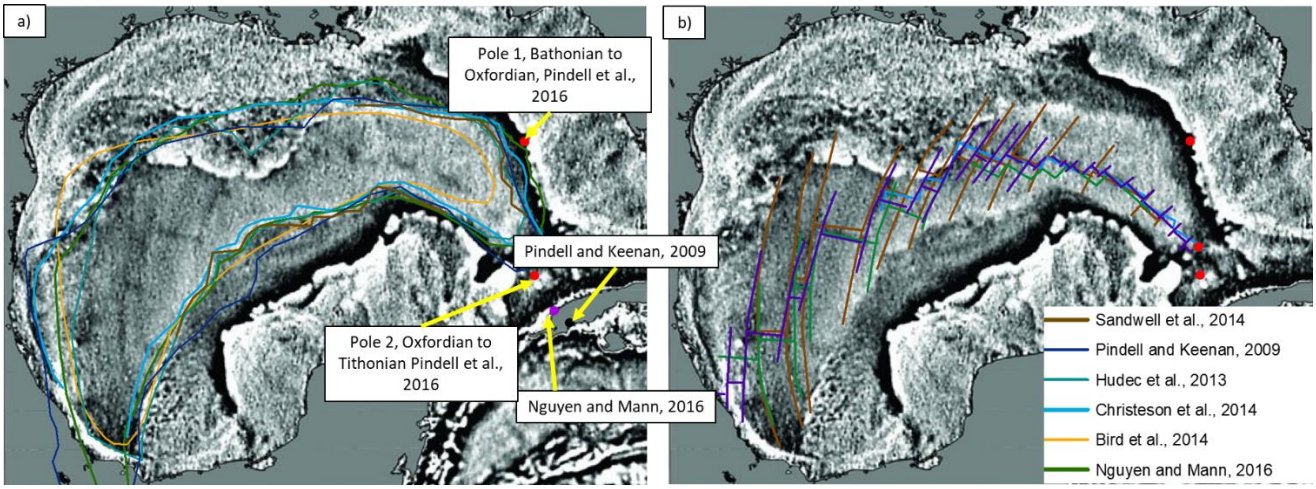

Figure 2. a) Location of the ocean-continent boundary (OCB) from various publications in the Gulf of Mexico. b) Location of published extinct spreading ridges and transform faults. The purple dot is the pole of rotation from Nguyen and Mann, 2016. The black dot is the pole of rotation from Pindell and Keenan, 2009. The background is vertical gravity gradient from Sandwell et al., 2014.

Figure 2 suggests striking asymmetry in the oceanic domain in the study area. The oceanic zone to the north of the spreading center is dramatically wider than the one to the south. This was noted by some of the authors (Hudec et al., 2013; Nguyen and Mann, 2016), but none of the previously published models discussed the reasons for such an asymmetric spreading in the GoM. This study addresses the observed high degree of asymmetry in the basin and proposes a mechanism to explain this observation in the northeastern GoM.

The Gulf of Mexico Basin Opening project (GUMBO, Duncan, 2013) provided new constraints on the structure of continental and oceanic crust in the northern part of the basin. The

four profiles of the GUMBO project targeted the northwestern (GUMBO Line 1), central (GUMBO Line 2), and eastern U.S. GoM (GUMBO Line 3 and GUMBO Line 4), as shown in Figure 1. Two recently published papers (Eddy et al., 2014; Christeson et al., 2014) presented the results of seismic refraction experiments along lines GUMBO3 and GUMBO4 in the northeastern GoM, featuring two distinct crustal zones in the oceanic domain. To date, none of the tectonic models have addressed the dramatic variations in crustal thickness and physical properties. This study provides an explanation for observed lateral variations in the oceanic crust and ties these distinct crustal zones to different spreading episodes.

The GoM comprises one of the largest petroleum provinces in the world (Whaley, 2006; Galloway, 2009). The first oil was extracted from the GoM back in 1938 (Galloway, 2009). In 2016, the total GoM production was around 4.5 MMboepd, with 80% liquid content (Erlingsen, 2017). According to the National Outer Continental shelf (OCS) program, the estimated resources on 160 million acres of the US sector contain about 48 Bbbl of undiscovered technically recoverable oil and 141 Tcf of undiscovered technically recoverable gas (WorldOil website, http://www.worldoil.com/news/2018/4/2/boem-announces-date-for-gulf-of-mexico-lease-sale-251). Despite the long exploration history, the GoM still contains huge hydrocarbon potential. In addition, the environmental regulation is the strictest in the northeastern GoM and the federal law bars drilling within 125 miles of Florida's Gulf coast (Henry, 2017). Therefore, the study area has received less attention from the petroleum industry than the rest of the US sector of the basin. This study provides important geological constraints on the tectonic architecture and crustal parameters of the northeastern GoM that are crucial for the petroleum basin modeling that guides hydrocarbon exploration.

Hartford and Filina (2018) performed similar integrative analysis of various geophysical datasets in the southern GoM and mapped the extend of the pre-salt basin along the Yucatan margin, where the pre-salt sediments are confidently imaged (Williams-Rojas et al. 2011; Sounders et al., 2017; O'Reily et al., 2017). As pre-salt petroleum exploration has gained extreme success in other basins, such as the Santos basin in Brazil (Diaz, 2018) and Kwanza basin in West Africa (Koning, 2014), pre-salt plays are emerging in the GoM (Arbouille et al., 2013). However, there are not many publically available seismic data over the pre-salt basin in the northeastern GoM. This study uses an integrative approach that combines multiple geophysical and geological datasets in order to determine the spatial extent and the thickness of the pre-salt deposits in the northeastern GoM. These are not only important for petroleum exploration, but also can be used to constrain the tectonic reconstruction of the entire basin, as they should match on the conjugate margins.

In addition, several crustal earthquakes (with the focal depths below 14 km) occurred in the middle of the oceanic domain in the study area, but far away from known tectonic structures. No current tectonic model takes these into consideration although these are large magnitude events (4.9 – 5.9 on the Richter's scale). The focal mechanisms developed for two of these earthquakes suggest compressional stress released along faults that do not correlate with any spreading centers or transform faults. Our study ties the observed seismicity in the northeastern GoM with a zone of weakness (pseudofault) between two distinct oceanic domains resulted from two spreading episodes.

The overarching goal of this study is to better understand the tectonic history of the Gulf of Mexico and provide an explanation for the several geological and geophysical observations that are not explained by any published tectonic model. These include known dramatic variations in

thickness and physical properties of the oceanic crust, the location of the ocean-continent boundary (Figure 2a), the location of extinct spreading ridges (Figure 2b), the apparent large degree of spreading asymmetry of the basin, noted by some authors, but not yet explained, and the mysterious crustal earthquakes in the center of the basin that are not aligned with any known geological structures.

1.2 Tectonic history of the Gulf of Mexico

Although the tectonic history of the GoM has been debated over decades (Buffler and Sawyer, 1985; Pindell and Keenan, 2009; Hudec et al., 2013; Eddy et al., 2014; Christeson et al., 2014; Nguyen and Mann, 2016; Lundin, 2017), most researchers agree that the opening of the Gulf of Mexico basin generally includes three stages as is shown in Figure 3:

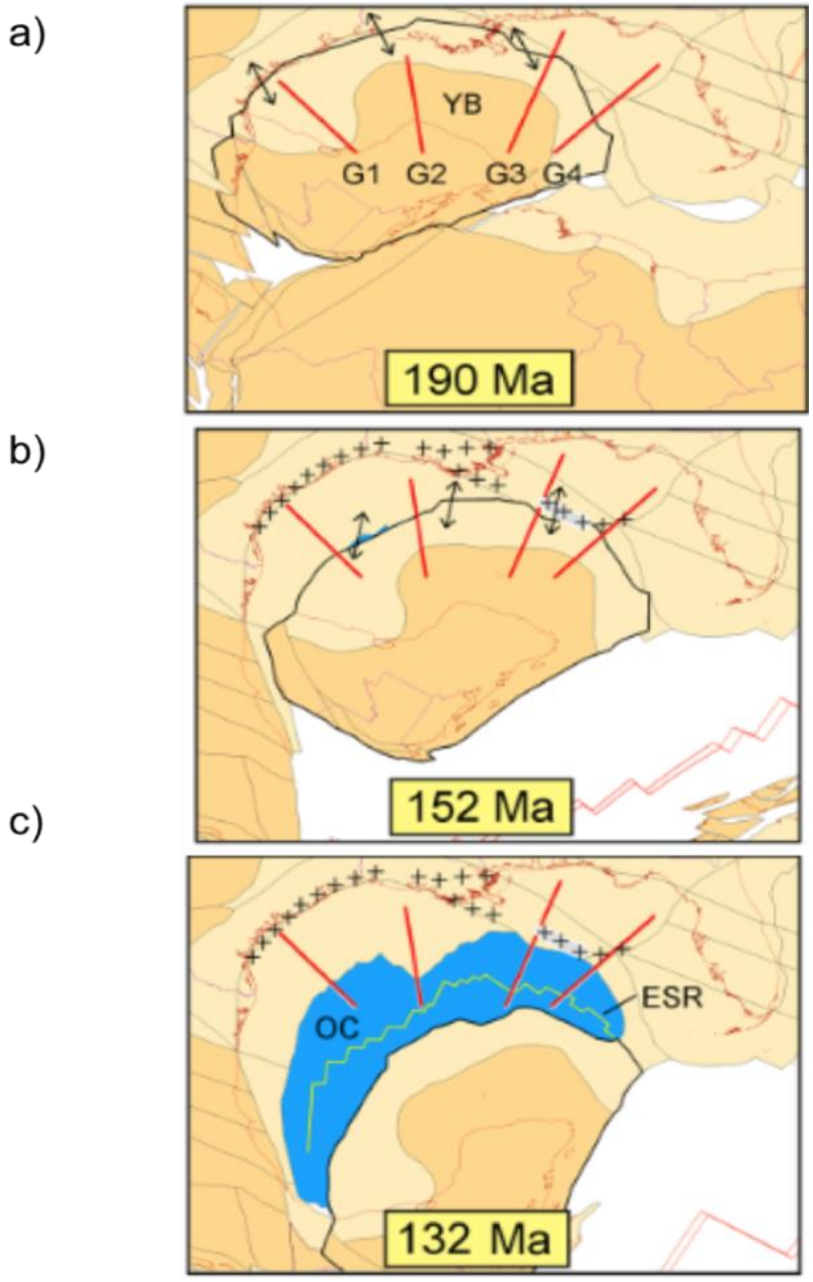

Figure 3. Brief tectonic history of the Gulf of Mexico modified from Eddy et al., 2014. Four red lines are four seismic refraction profiles (GUMBO1-4).

a) Stage 1: NW-SE continental rift, marked by black arrows. YB-Yucatan Block.

b) Stage 2: salt deposits started accumulating in the stretched continental region. The direction of continental rift changed from NW-SE to N-S.

c) Stage 3: the Yucatan block rotated counterclockwise away from North America plate during seafloor spreading and formed the GoM basin. Seafloor spreading ceased in the Early Cretaceous. Arrows indicate the rifting direction. YB-Yucatan Block. OC- Oceanic crust. ESR-Extinct spreading ridge. Plus symbols are the Gulf coast magnetic anomaly.

Stage 1: Continental rifting (Late Triassic-Middle Jurassic, 230 – 158 Ma)

The first stage comprises a continental rift in the Late Triassic to Middle Jurassic (230-158 Ma) between the Yucatan block, North America, and South America (Pindell and Keenan, 2009; Hudec et al., 2013; Eddy et al., 2014; Christeson et al., 2014; Nguyen and Mann, 2016; Lundin, 2017). However, the exact timing is still under debate (Table 1). Pindell (1985) proposed the rifting happened between 190 and 158 Ma, while Hudec et al. (2013) suggested that the rifting occurred between 240 and 166 Ma (Table 1). It is believed that this initial continental rift was caused by northwest-southeast stretching (Pindell and Keenan, 2009; Hudec et al., 2013; Eddy et al., 2014; Nguyen and Mann, 2016). The red beds, such as the Eagle Mill formation in the northeastern GoM and its equivalents (La Boca Formation) filled the extensional grabens in the rifting stage (Bartok, 1999; Hudec et al., 2013). Mickus et al. (2009) proposed that continued rifting formed a volcanic rifted margin in the northwestern part of the basin, resulting in seaward-dipping seismic reflectors (SDRs) along the Gulf coast. This conclusion is based on the presence of a pronounced magnetic anomaly along the Texas coastline, known as the Houston magnetic anomaly after Hall (1990). Volcanic rifted margins usually are formed by rapid, voluminous emplacement of lavas, dikes, sills, and plutons (Mickus et al., 2009). Pascoe et al. (2016) believe the volcanic margin interpretation is unlikely and suggest that the zone of high magnetic intensity represents a suture zone related to the late Paleozoic orogeny during formation of Pangea. A similar interpretation was proposed by Kneller and Johnson (2011) and Van Avendonk et al. (2015), who concluded that the rifting was volcanic-poor and resulted in a mantle exhumation in the northwestern GoM. Eddy et al. (2014) suggest that the SDRs along the eastern GoM margin, coincident with magnetic highs, may be a part of an “inner wedge” system of syn-rift basins, filled with basalts and volcaniclastic sediments during continental extension.

Stage 2: salt deposition (Late Jurassic, ~158 Ma)

This stage includes a short period of widespread deposition of a thick salt layer that filled in the Proto-GoM basin. Some researchers believe that this was associated with the final stage of continental rifting, so the salt was deposited on the stretched continental crust (Pindell, 1985; Bird, 2005; Galloway, 2009; Pindell and Keenan, 2009; Nguyen and Mann, 2016). According to Hudec et al. (2013), continental rifting continued another 2 Ma after the salt was deposited. However, a number of models allow salt deposition on oceanic crust (Stern and Dickson, 2010; Padilla-Sanchez, 2017). Consequently, the origin and timing of salt deposition is still being debated (Table 1). According to Bird et al. (2005), before the sea-floor spreading (next tectonic stage), the Yucatan block rotated about 22 degrees counterclockwise between 160 Ma and 150 Ma (as a part of continental rifting), which allowed intermittent seawater influx and produced massive salt deposition. Dribus et al. (2008) proposed that storm surges from the Pacific entering the Proto-GoM and eventually forming the evaporites. Pindell and Keenan (2009) suggested the salt was deposited before the Late Callovian (158 Ma). According to Hudec et al. (2013), an evaporite sump was isolated from the world ocean and became saline enough to deposit halite between 165 and 161 Ma (Callovian).

Nevertheless, the relationship and timing between the salt and the oceanic crust are still unclear. Padilla-Sanchez (2017) proposed that the salt was deposited after the oceanic crust (next stage) was already formed and ceased, i.e. the basin was opened before the salt was deposited. This study accepts the timing proposed by the majority of the models and assumes that the salt formed on the stretched continental crust before the seafloor spreading commenced.

Stage 3: Seafloor spreading and rotation of the Yucatan Block (Late Jurassic to Early Cretaceous, 162-130 Ma)

Some authors (Stern and Dickinson, 2010, Lundin, 2017) proposed that the GoM is a backarc basin (BAB, a basin formed via seafloor spreading behind an active subduction zone). According to Stern and Dickinson (2010), the GoM opened behind the 232-150 Ma old Nazas arc over an east-dipping subduction zone in Late Jurassic time, beginning ca. 165 Ma. The spreading ridges in the oceanic domain of the GoM are oriented nearly orthogonally to the Paleo-Pacific subduction direction (Stern and Dickinson, 2010; Lundin, 2017).

The exact time when the oceanic crust formed and whether the salt was formed on the oceanic crust or flowed later onto oceanic crust is still being debated (Table 1). Although the timing, the initial location of the Yucatan, the angle of rotation, and the relationship with salt are still not well constrained, there is overall agreement that the oceanic crust in the GoM formed while the Yucatan crustal block rotated counterclockwise from North America. According to Pindell and Keenan (2009), the seafloor spreading initiated in the very early Oxfordian age (158 Ma). According to Eddy et al. (2014), between Jurassic to Early Cretaceous(~152-132Ma), the Yucatan Block rotated about 40 degrees counterclockwise away from the North American plate, which lead to a separation of the initial salt basin into the northern Louann and the southern Campeche salt provinces (Figure 1).

Published tectonic reconstruction models have proposed different locations of the Euler pole, as well as various rotation angles for the Yucatan crustal block (Table 1). The proposed total angle of rotation is 43 degrees according to Pindell (1985), 37 degrees according to Nguyen and Mann (2016), and 78+/- 11 degrees according to Lundin (2017). The pole of rotation is located in

the region defined by the following coordinates at 79-84 °W, 23-30 °N (Bird et al., 2005; Pindell and Keenan, 2009; Stern and Dickson, 2010; Nguyen and Mann, 2016).

Most of the tectonic models suggest that the oceanic crust formation started in the western GoM and propagated to the east (Christeson et al., 2014; Eddy et al., 2014; Pindell and Kennan, 2009; Nguyen and Mann, 2016; Lundin 2017). This conclusion is guided by generally accepted tectonic reconstruction with the Euler pole located in the region between the Florida Straits and Northern Cuba as described above. In contrast, Hudec et al. (2013) concluded that seafloor spreading started simultaneously in the western and eastern parts of the basin and propagated toward to the center of the basin based on analysis of multiple proprietary seismic datasets in all parts of the GoM.

Seafloor spreading ceased in the Early Cretaceous~140 Ma (Christeson et al., 2014; Eddy et al., 2014; Nguyen and Mann, 2016) when the Yucatan Block docked against southern Mexico. Snedden et al. (2014) correlated seismic surfaces onlapping onto newly created oceanic crust from the onshore wells to constrain the timing of seafloor spreading as 152 - 137 Ma. Overall, the timing of seafloor spreading differs between various tectonic models as is illustrated by Table 1.

The basin began to subside as a passive continental margin during the post-rift tectonic stage. Throughout the Cenozoic, the area has been relatively stable and characterized by subsidence. Reef-building organism formed 2-3 km thick carbonate deposits near the Florida shelf (Eddy et al., 2014). Post-rift cooling and subsidence created accommodation for clastic influx from adjacent fluvial and deltaic systems, which halted carbonate production (Eddy et al., 2014; Galloway, 2008).

Table 1. Summary of published tectonic models for the Gulf of Mexico.

	Continental rift time and direction	Salt deposition time	Yucatan rotation time and angle	Euler pole location	Seafloor spreading time
Bird et al., 2005	230-160 Ma	Before 150 Ma	160-140 Ma; 42°	24 N°, 81.5° W	150 - 130 Ma
Pindell and Keenan, 2009	190-158 Ma; SE direction with minor counter-clockwise rotation	Before Late Callovian (158 Ma)	Late Jurassic to Early Cretaceous, NA	Deep SE Gulf(~-84°W24°N)	Started in early Oxfordian time (158 Ma) to 130 Ma
Stern and Dickinson, 2010	No continental rifting stage; East Mexico Arc and Nazas Arc formed	Mid to Late Jurassic	165-142Ma	79-84°W, 23-30° N	After 176 Ma to 156 Ma
Hudec et al., 2013	210-163 Ma; NE-SE	163-161 Ma	210 Ma-137Ma; 43.09°	97.18° -26.49° at 210 Ma (changed 5 times with age)	154 Ma to 149 – 137 Ma
Eddy et al., 2014	Triassic to Mid-Jurassic SW movement of the Yucatan block until 158-154 Ma	NA	158-154 Ma to 140-137 Ma	SE GoM	160 - 140 Ma
Christeson et al., 2014	NA	NA	NA	NA	152-155 Ma to 138-142 Ma
Nguyen and Mann, 2016	190-170 Ma, NW-SE	Mid-Jurassic	Late Jurassic (start in 158__Ma); 37°	Western Cuba (-84°, 23°)	162 - 132 Ma
Lundin, 2017	228.4-209.5 Ma	Callovian (166.1–163.5 Ma)	N/A; 78+/-11° CCW since Permian	Florida Straits	Ends at 145-139.4 Ma

1.3 Stratigraphy in the northeastern Gulf of Mexico

The sediments in the northeastern GoM consist of siliciclastics, carbonates, and salt (Galloway, 2009). The age of the sedimentary rocks spans from Late Triassic up to recent (Figure 4). During the first stage of the rifting in the Late Triassic, volcanic clasts and redbeds filled in the grabens developed on the stretched crust, forming the Eagle Mill Formation in the northern part (Pilger, 1981; Warwick, 2017) and La Boca Formation (Bartok, 1999) in the southern part, which are the pre-salt deposits. Goswami et al. (2017) suggest a largely clastic lithology with minor amounts of interbedded volcanics in the pre-salt package. The consequent marine transgression led to marine water being trapped in the basin, resulting in deposition of the Werner Anhydrite Formation (Salvador, 1987). During periods of marine influx and evaporation, the Louann salt was deposited in the basin (Salvador, 1991). The time of salt deposition differs slightly between the models (Table 1). Wilson (2011) believes the Louann salt was deposited in the basin from Bajocian to Callovian (~167 to 162 Ma, but an exact age was not provided in the text rather estimated from the International Chronostratigraphic Chart), while Pindell (1985) suggest the Louann salt was deposited in the basin around the Callovian (158 Ma). According to Wilson (2011), during the Early Oxfordian (~160Ma, Late Jurassic), texturally mature aeolian sands were deposited in the northeastern GoM basin forming the Norphlet Formation. These aeolian quartzose sandstone facies consist of well-rounded, well-sorted, quartz-rich, hematite-coated sands, deposited with little to no clay matrix during a Late Jurassic transgression, are also reported by Pearson (2011) and Steier (2018). The Norphlet Formation is one of the critical reservoir rocks in the northeastern GoM and is producing in present-day Mississippi, Alabama, Florida, and the deep water northeastern GoM (Godo, 2017; Steier, 2018). In Oxfordian time (~156 Ma, Late Jurassic), another marine transgression formed the carbonate unit, known as the Smackover Formation (Wilson,

2011), which is the primary source rock in the northeastern GoM. The sea level continued to rise, and the Haynesville Formation, consisting of sandstone, siltstone, and shales was deposited in the eastern Gulf region during the Kimmeridgian (~152 Ma, Salvador, 1987) time. At the beginning of the Early Cretaceous (~150 Ma), the Cotton Valley Formation formed as a primary reservoir and was intimately interbedded with source rocks in the northern GoM (Galloway, 2009). The end of the Cotton Valley Formation indicates the beginning of the modern carbonate platform accumulation (Wilson, 2011). Rimmed carbonate shelf developed during Cretaceous (Galloway, 2008). Paleogene clastic progradation resulted in the deposition of the following formations (Figure 4): Midway, Wilcox, Claiborne, Jackson, Vicksburg, and Catahoula formations. Among these formations, Wilcox group comprises a major reservoir in the northern GoM and characterized as fluvial, deltaic, and shallow marine environment (Fisher and McGowen, 1976). The Fleming group was deposited as a result of Miocene progradation in the central and northeastern Gulf (Galloway, 2008). The Neogene deposits progradated in the basin along the central Gulf margin, while a primarily aggradational carbonate platform formed along the Florida margin (Galloway, 2008).

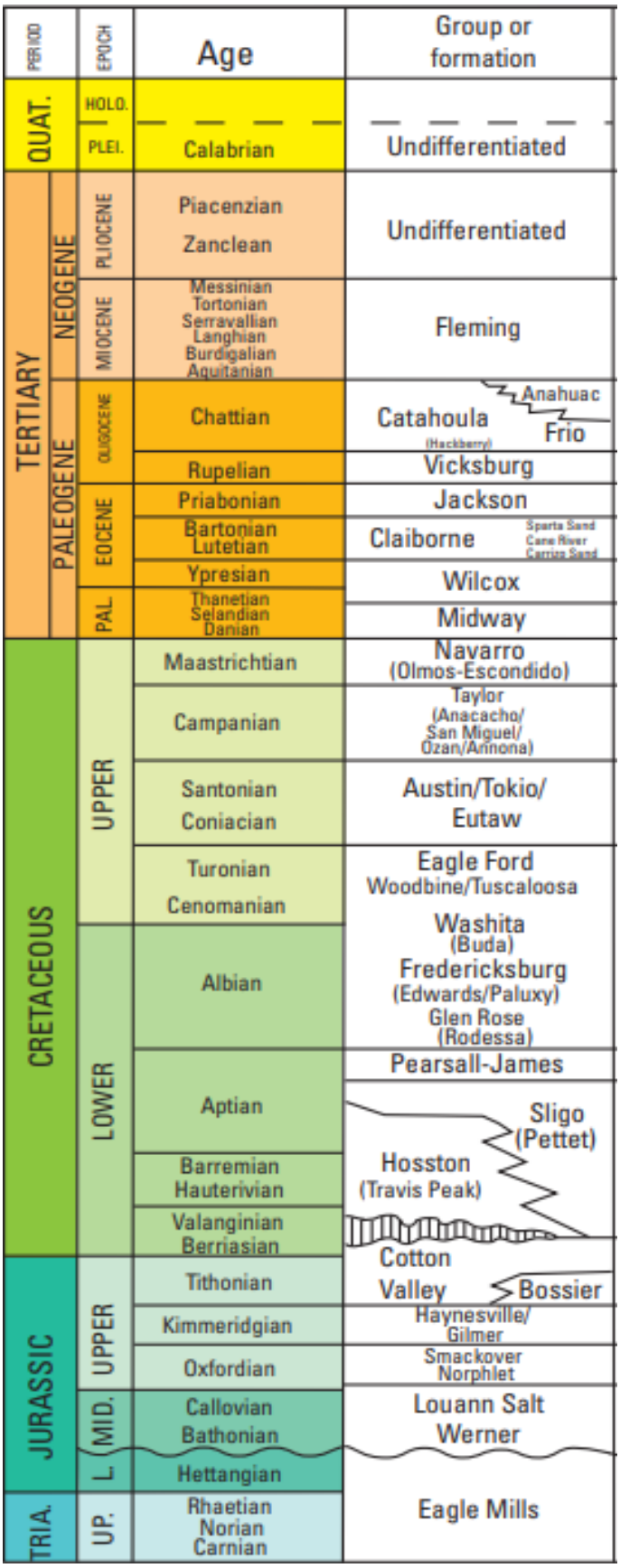

Figure 4. Stratigraphy of the northeastern Gulf of Mexico modified from Warwick, 2017.

CHAPTER 2. Geophysical Data

2.1 Seismic refraction data

In 2010, the Gulf of Mexico Basin Opening Project (GUMBO) was conducted to study the lithological composition and structural evolution of the GoM (Duncan, 2013; Eddy et al., 2014; Christeson et al., 2014). It used Ocean Bottom Seismometers (OBS) and an air-gun seismic source to collect seismic refraction data in the U.S. Gulf along four profiles (Figure 1): GUMBO1 in the northwestern GoM, GUMBO2 in the center, and GUMBO3 and 4 in the northeastern GoM. The length of GUMBO transects ranges from ~300 km to over 500 km. The OBS spacing for transects in the eastern GoM is 12 km with a time sampling interval of 5 ms and a shot spacing of 150 m (Duncan, 2013).

GUMBO3 (Figure 5) extends from offshore Florida, across De Soto Canyon, to the center of the basin. The total length of GUMBO3 is 524 km. Figure 5 shows the interpretation of seismic refraction data from Eddy et al., 2014. The three layers are defined based on velocity structure, which are sediments, crust, and mantle. Eddy et al. (2014) also interpreted a carbonate platform and several salt structures in this line. The line starts in the continental domain and ends in the oceanic domain with the OCB interpreted by Eddy et al. (2014) to be at the distance of 270-290 km. The top of the continental crust is at a depth of ~7 km, which is shallower than oceanic crust at ~ 10 km. The continental crust at the beginning of the profile is ~25 km thick, while the oceanic crust has an average thickness of ~9 km. The oceanic crust near the OCB is thinner (8 km) and its thickness increases to 10 km at 430 km along model distance. The velocity of the upper oceanic crust varies between 6 km/s to 6.5 km/s, while the velocity of the lower oceanic crust is 6.5 to 7 km/s.

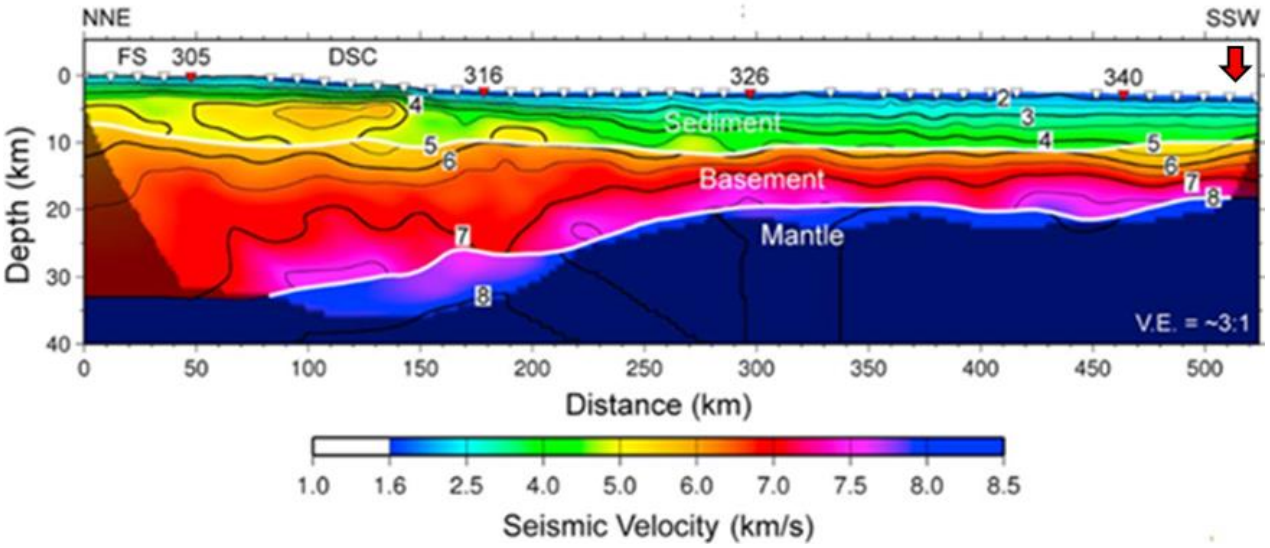

Figure 5. Seismic refraction profile GUMBO3 (modified from Eddy et al., 2014). The location of the profile is shown in Figure 1. Numbers within the layers indicate the seismic velocities in km/s. White lines represent the top of basement and Moho boundaries. Inverted triangles show ocean bottom seismometers locations. FS-Florida shelf; DSC-De Soto Canyon. The red arrow at the end of the profile indicates the crossing point with the profile from Horn et al. (2017).

Profile GUMBO4 is located to the southeast of GUMBO3. It extends from the northwestern Florida Peninsula, across the continental shelf, Florida Escarpment, and into the central GoM (Figure 1). Profile GUMBO4 has a total length of 507 km. Figure 6 (modified from Christeson et al., 2014) shows a similar three-layered interpretation: sediments, crust, and mantle. A carbonate platform is interpreted at the northeastern end of the line.

The top of the continental crust is very shallow at a depth of ~5 km. The continental crust is ~29 km thick at the beginning of the line, while the oceanic crust is only ~5 km thick along the GUMBO4, which is about 4 km thinner than GUMBO3. Near the OCB, the oceanic crust has a uniform velocity of 7.0 km/s.

Toward the end of the profile, the velocity of the top 2.5 km of the oceanic crust drops to 6.0 km/s and to 6.8 km/s in the lower portion of the oceanic crust. Notably, these two profiles are ~125km away from each other, but they show dramatic variations in the oceanic crust, namely in the crustal thickness and the velocity of compressional seismic waves.

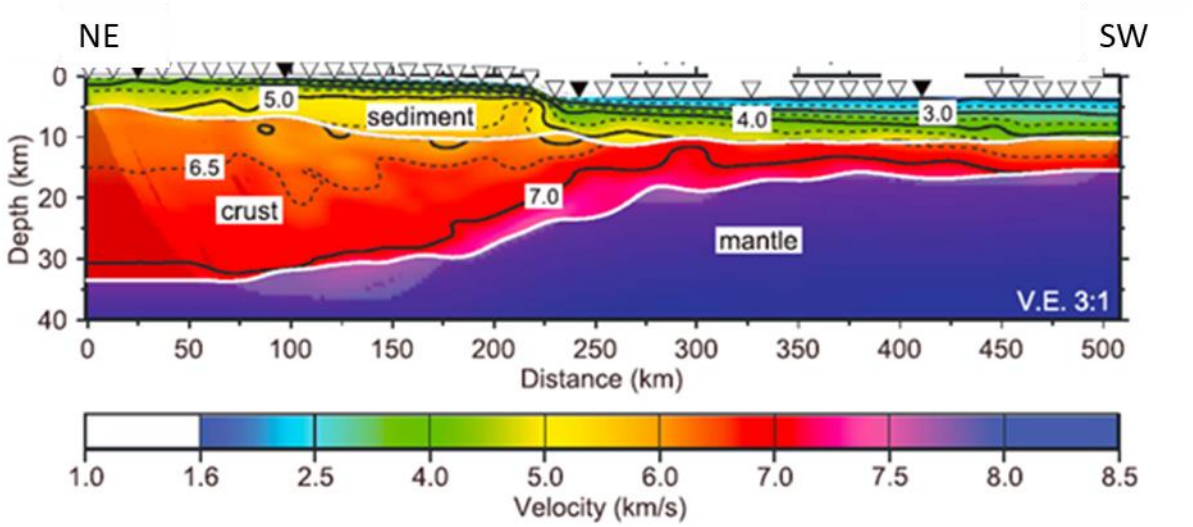

Figure 6. Seismic refraction profile GUMBO4 (modified from Christeson et al., 2014). The location of the profile is in Figure 1. Refer to Figure 5 for description.

Several vintage seismic refraction points from Ibrahim et al. (1981) were used to validate the depth of basement and the Moho (Table 2) in the study area. The distribution of seismic refraction points is shown in Figure 7.

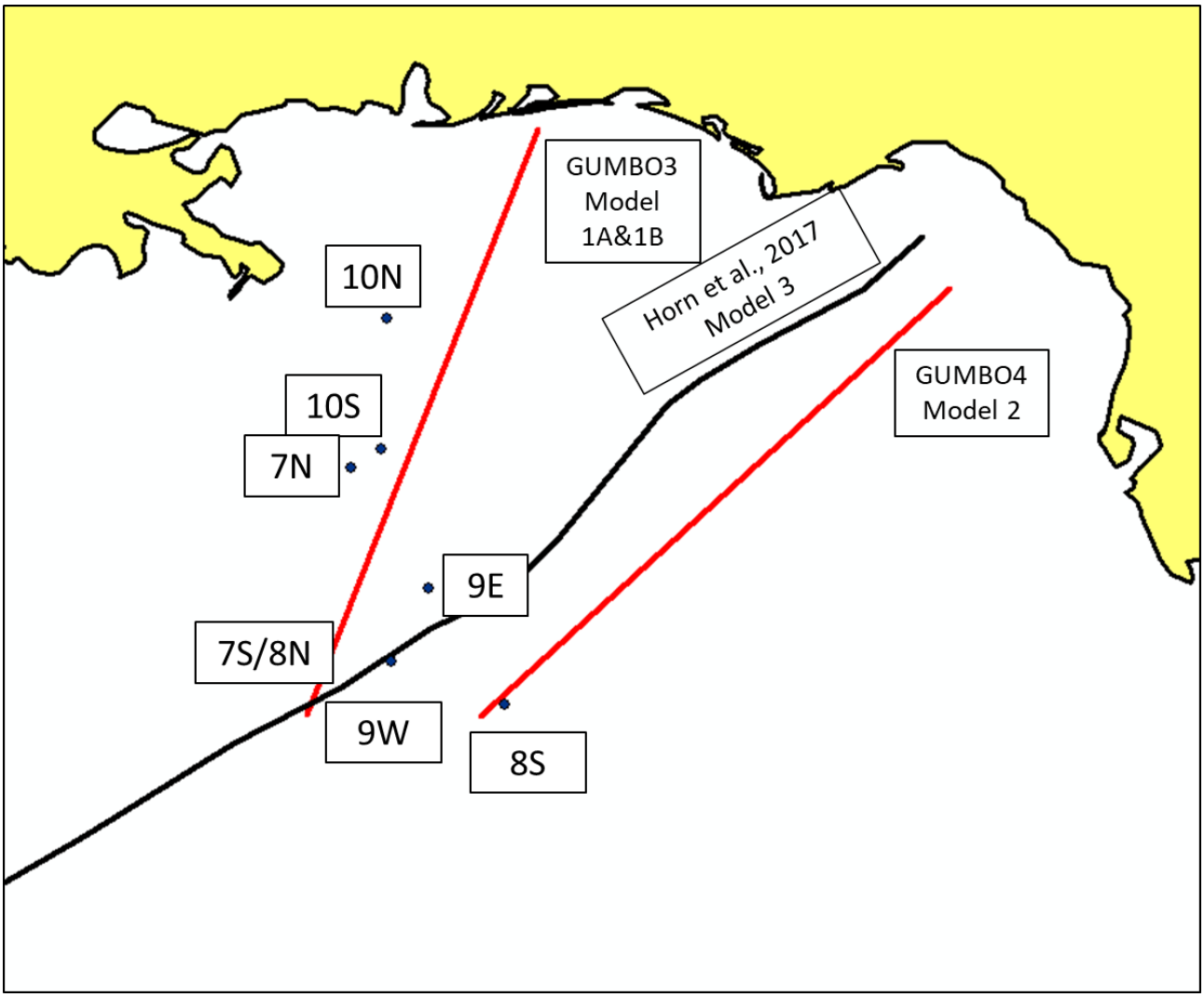

Figure 7. Location of seismic refraction points from Ibrahim et al. (1981) in the study area. The data are listed in Table 2. The three profiles were used to build 2D subsurface models.

Table 2. Seismic refraction data from Ibrahim et al., 1981. See Figure 7 for location of these refraction profiles.

Profile	Position (°N Long. °W Lat.)	Velocity of compressional seismic waves for different layers, km/s							Interpreted layers' thicknesses, km						
		Unconso-lidated sediments	A	B	C	D	E	F	Water	Unconso-lidated sediments	A	B	C	D	E
10N	28.71 87.88	1.8 2.2		3.2	4.8	6.3		7.6	2.17	0.16 2.25		2.68	1.81	11.94	
10S	27.72 87.98								2.50	0.98 0.93		3.22	4.63	3.32	
7N	27.46 88.24	1.9 2.1		3.0	4.7		7.0	7.9	2.23	0.87 1.65		3.13	3.54		5.34
7S	26.63 87.69								2.70	0.08 2.16	3.32	3.75			6.49
8N	26.63 87.69	1.8 2.0		2.9	5.1		6.9	7.8	2.70	0.12 1.89		3.79	2.39		7.71
8S	25.77 87.10								3.21	0.12 1.56		3.94	3.40		2.55
9E	26.73 87.18	1.8 2.0		3.1	4.8		6.8	8.0	2.79	0.42 2.11		3.12	2.78		5.05
9W	26.04 87.9								2.95	0.57 1.62		3.76	2.17		6.5

2.2 Seismic reflection data

There are seismic reflection profiles along GUMBO3 and 4 transects. Profile Fugro533 (Figure 8) overlaps with GUMBO3 (Eddy et al., 2014). The top of the basement and Moho (blue and black lines in Figure 8) are interpreted from the GUMBO3 refraction experiment. Salt structures are located at the model distance of ~170 to 310 km in the sedimentary unit (Eddy et al., 2014). Reflectors in the basement beneath the salt structures are observed with seaward dips of ~25°-30°, which are interpreted as volcanic seaward dipping reflectors (SDRs) (Eddy et al., 2014). The SDR layer under the Apalachicola Basin has a width of 100 km and a depth of ~10 km.

Toward the end of the line, an extinct spreading ridge (ESR) is interpreted to be coincident with the observed half-graben structure from Eddy et al. (2014). Near the OCB, at the distance of 300-400 km along the model, the Moho from GUMBO3 is interpreted at depth of 23 km. However, there are strong reflectors at a depth of ~17.98 km in the refraction seismic that could also be interpreted as the Moho (shown with arrows in Figure 8).

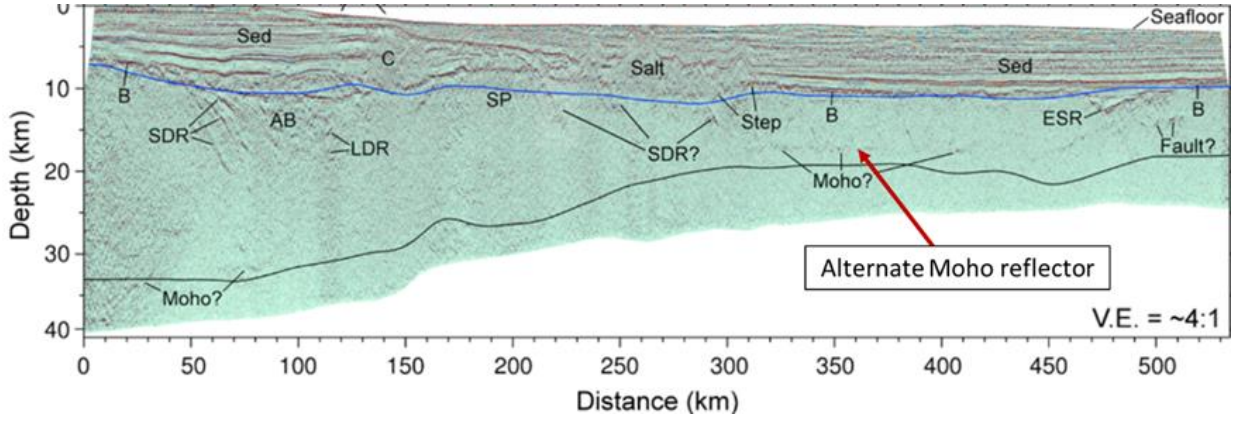

Figure 8. Seismic reflection profile Fugro533 (modified from Eddy et al., 2014). The location of this profile is the same as GUMBO3. The blue line and black line denotes the top of the basement and Moho interpreted from GUMBO3 respectively. The red arrow indicates an alternative Moho reflector. AB-Apalachicola Basin; B-MCS Basement; C-carbonate platform; DSC-De Soto Canyon; ESR- extinct spreading ridge; LDR- landward dipping reflector; SDR-seaward dipping reflector; SP-Southern Platform.

Seismic reflection profile Fugro642 (Figure 9) overlaps with GUMBO4. The top of the basement seismic reflectors is not associated with strong contrast due to the thick carbonate platform, which tends to attenuate the signal of deep reflectors (Christeson et al., 2014). In the deep-water region, there are no significant basement reflections observed, nor is there a clear landward dipping basement ramp as in GUMBO3 (Christeson et al., 2014).

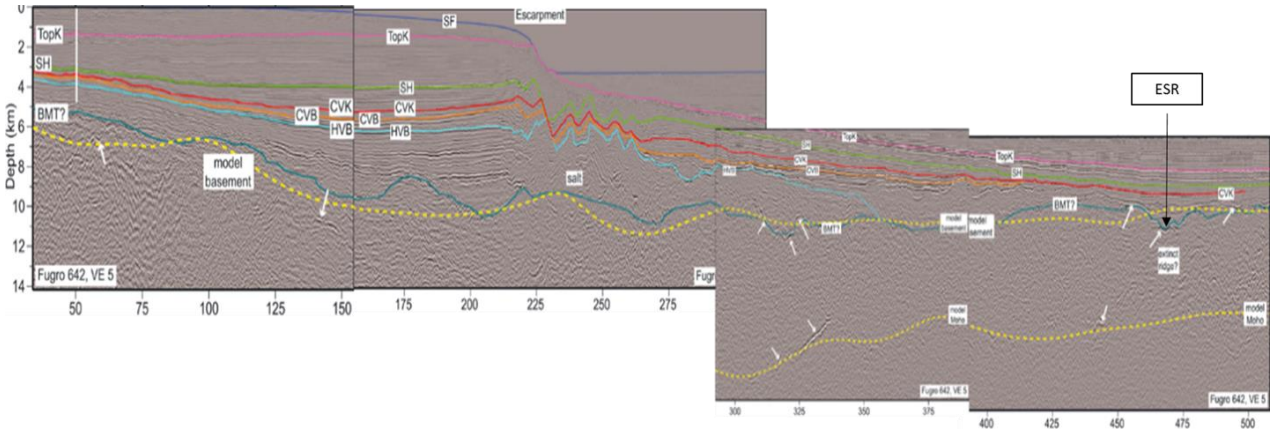

Figure 9. Seismic reflection profile along Fugro642 (Modified from Christeson et al., 2014). The dark blue denotes the top of the basement. White arrows mark strong reflectors. ESR—extinct spreading center. ESR is detected from potential fields and Vp (~6 km/s). Close-up of MoR1is shown in Figure 26.

Table 3 shows the comparison of depths to basement and Moho from different sources. The vintage refraction data (location is in Figure 7) suggest ~3-4 km shallower basement than both GUMBO3 and Fugro533 (Table 3). In terms of Moho depth, Fugro533 is in agreement with seismic refraction points (Table 3), while GUMBO3 suggests a ~2 km deeper Moho interpretation. Thus, the vintage refraction data agrees better with seismic reflection data (Fugro533) than with the seismic refraction line (GUMBO3). These two alternative Moho interpretations led to two subsurface models developed for profile GUMBO3: Model 1A for seismic refraction data (deep Moho), and Model 1B for seismic reflection data (shallow Moho). Since the basement and Moho

interpretations are in agreement between GUMBO4 and Fugro642 profiles, only one subsurface model was developed for that line - Model 2.

Table 3. Depth to different geological boundaries in km from different seismic experiments.

Profile	Basement depth, km					Moho depth, km				
	Ibrahim et al., 1981	GUMBO3	GUMBO4	Fugro533	Horn et al, 2017	Ibrahim et al., 1981(Ibrahim et al., 1981)	GUMBO3	GUMBO4	Fugro533	Horn et al, 2017
10N	7.26	10.3		9.9		21.01	26.79		26.45	
10S	7.63	11.79		11.6		15.58	19.91		19.67	
7N	7.88	11.18		10.8		16.76	19.54		19.28	
7S	12.01	11.18		11.21		18.5	20.15		17.98	
8N	8.5	11.18		11.21		18.6	20.15		17.98	
8S	8.83		10.16			14.78		15.53		
9E	8.44				9.56	16.27				16.87
9W	8.9				10.39	17.57				17.93

Several additional 2D and 3D seismic reflection surveys were used to validate the basement structures and to constrain subsurface modeling. The locations of those are shown in Figure 10.

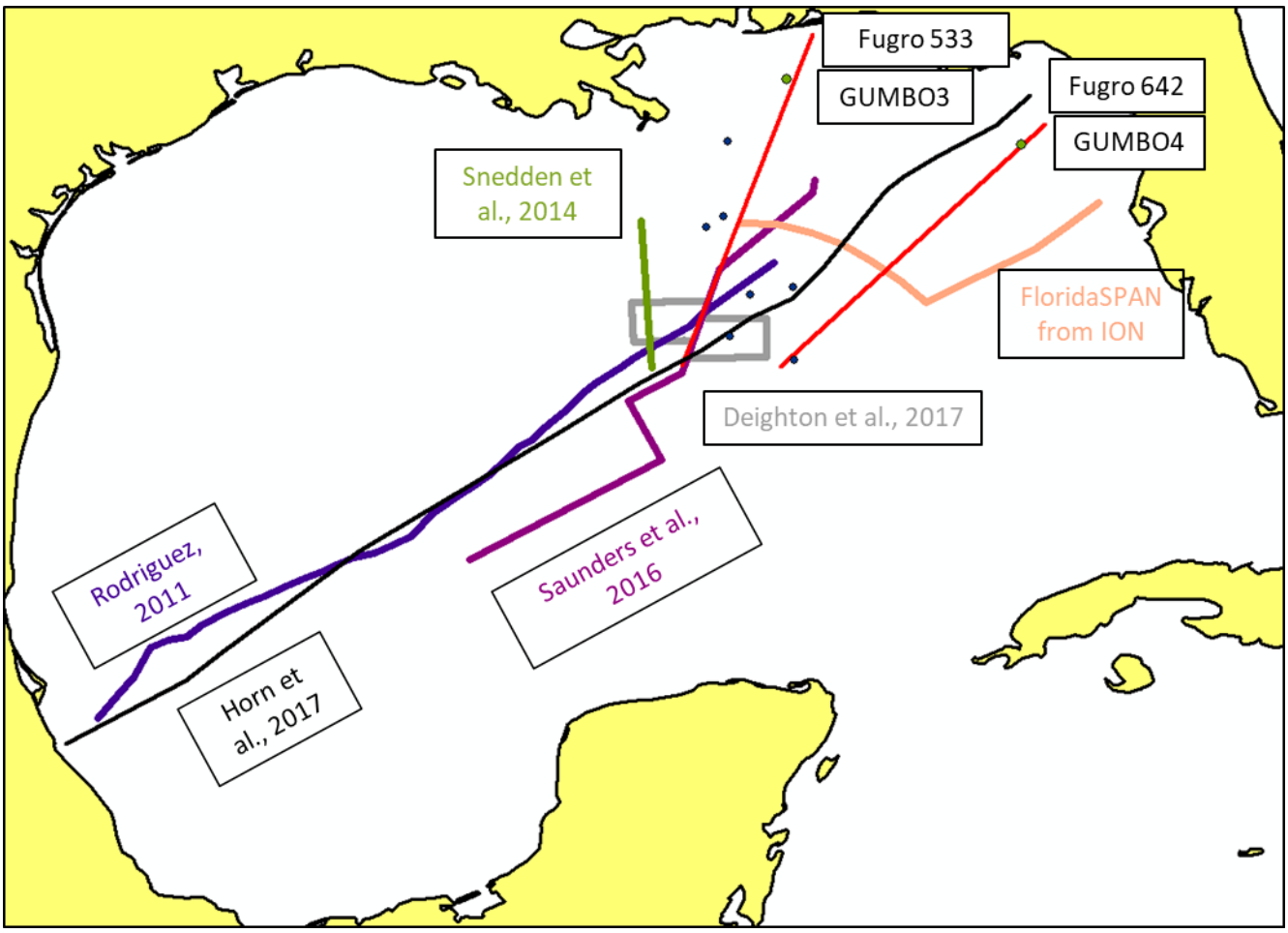

Figure 10. Seismic data used in this project. G3 and G4 are two GUMBO profiles from the Gulf of Mexico Basin Opening project. Gray box outlines 3D seismic reflection survey from Deighton et al., 2016. Two green dots indicate the well locations from the Bureau of Ocean Energy Management website (BOEM). Well No Logs G2468 is next to GUMBO3 and well No. 1 O.C.S.-G-2516 is located on GUMBO4. Several blue dots indicates the seismic refraction database from Ibrahim et al., 1981.

The line from Saunders et al., 2016 (thin purple line in Figure 10) partially overlaps GUMBO3. The seismic reflection image for that line is shown in Figure 11. The basement

structures are well imaged in this profile. It was used to validate the location of the extinct spreading center (mid-ocean valley).

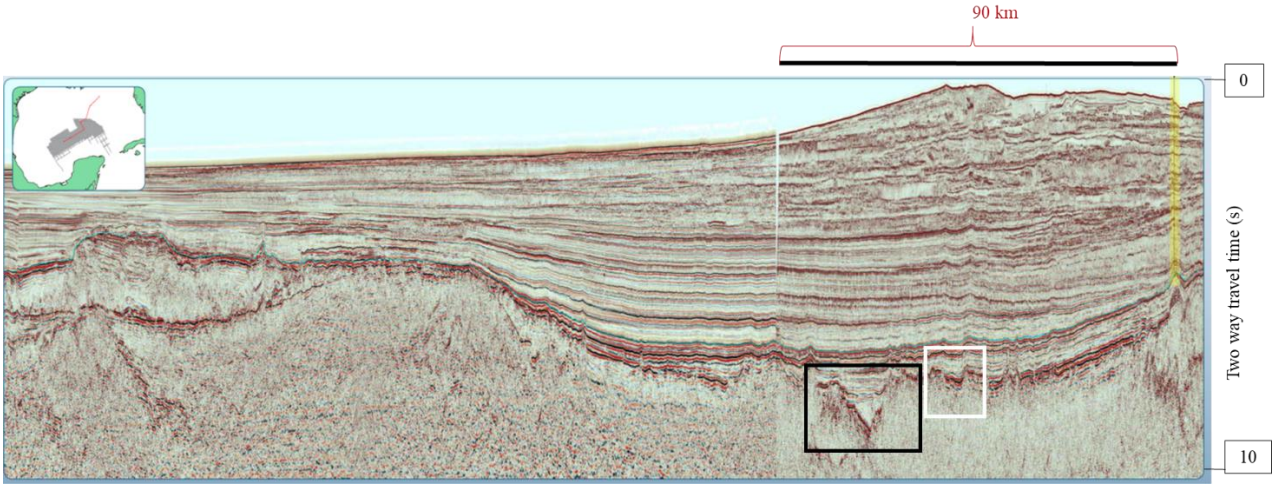

Figure 11. Seismic reflection profile from Saunders et al., 2016. The vertical scale is two-way travel time in seconds. The yellow line on the right side of the profile is the well in the block Lloyd ridge 399. The horizontal line bar on the top indicates part of the profile that overlaps with GUMBO3 profile (Figure 5). The black box outlines the extinct spreading center.

Figure 12 shows another 2D seismic reflection line used for subsurface modeling. Model 3 was developed along the line acquired by ION in 2015 (Horn et al., 2017). This line starts near GUMBO4, and it crosses GUMBO3 near the end of GUMBO3 (Figure 9). Therefore, this profile can be used to study the variations between the crustal structures observed between GUMBO3 and GUMBO4.

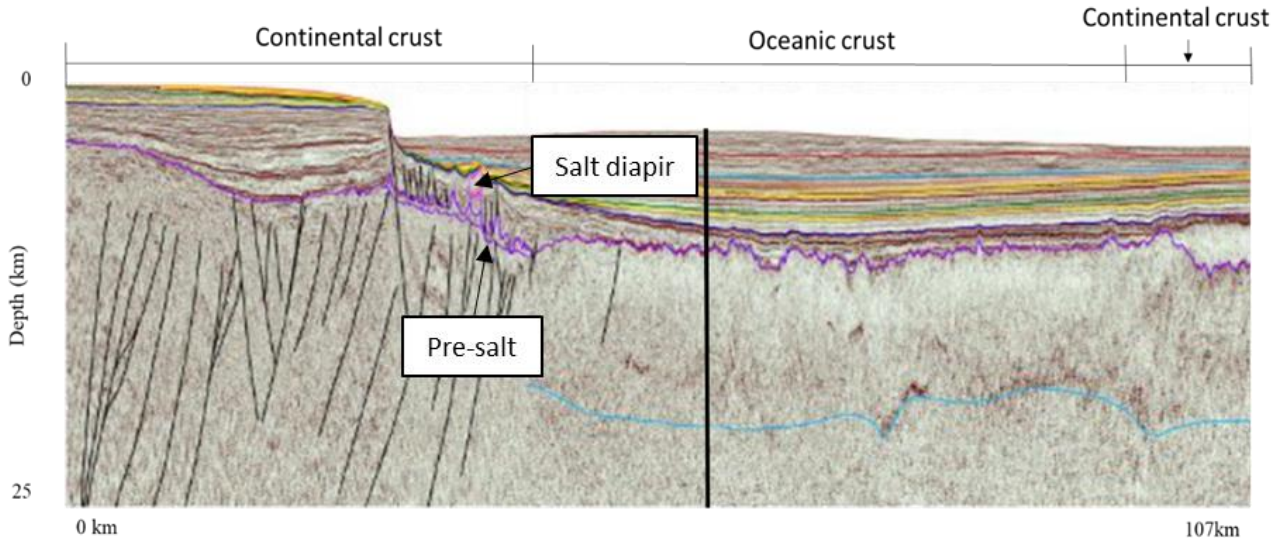

Figure 12. Seismic reflection profile from Horn et al., 2017. The vertical axis is depth in km. The black vertical line indicates the crossing point with GUMBO3.

Figure 13 shows 2D seismic reflection profile from Rodriguez (2011). This seismic section crosses GUMBO3. As the seismic imaging of the crust is not clear, no subsurface model was developed for this line. Instead, these data were used to constrain the thickness of individual sedimentary layers in Models 1A and 1B (aligned with GUMBO3).

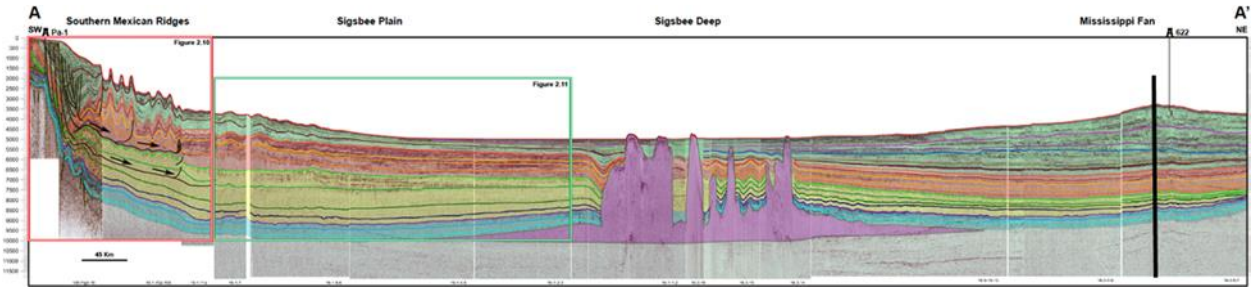

Figure 13. Seismic reflection profile from Rodriguez, 2011. This vertical scale is two-way travel time in seconds. The black line close to A' indicates where this profile crosses GUMBO3. This crossing point was used to constrain the thickness of sedimentary layers for GUMBO 3.

The 3D seismic reflection survey recorded by TGS (Deighton et al., 2017) was used to validate the location of extinct spreading centers. The location of this survey is shown as a gray box in Figure 10. Figure 14 shows the depth to basement interpretation from Deighton et al., 2017,

featuring the mid-ocean valleys (red color) and interpreted transform faults within the 3D seismic survey area.

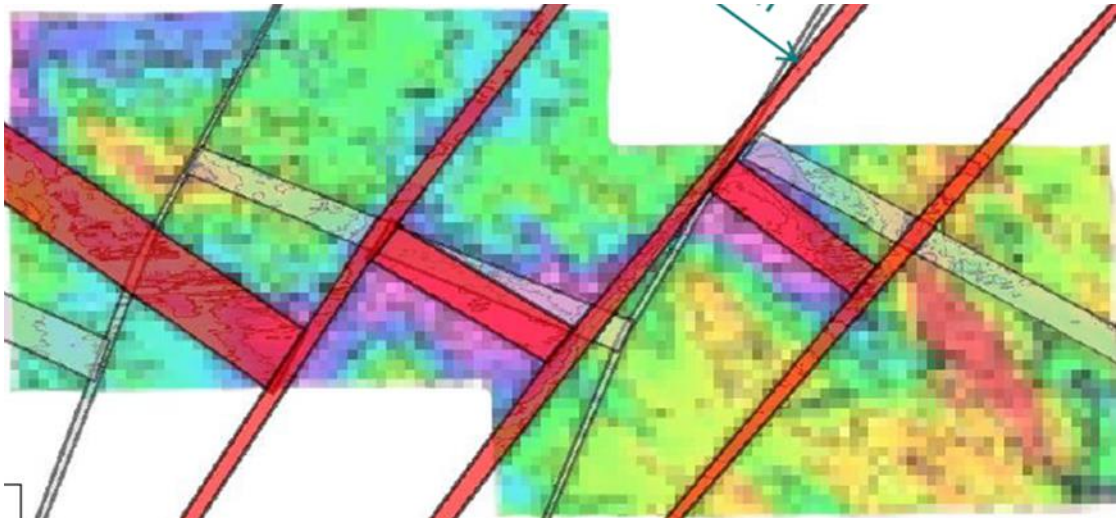

Figure 14. Interpretation from 3D seismic reflection data (Deighton et al., 2017). The location of the survey is shown as gray box in Figure 10. The background shows depth to basement in time; red are lows, blue are highs. The red color is TGS's interpretation of extinct spreading centers and transform faults. The grey lines show the earlier interpretation from Sandwell et al., 2014.

The profile from FloridaSPAN seismic reflection survey recorded by ION (https://www.iongeo.com/content/documents/Resource%20Center/Brochures%20and%20Data%20Sheets/Data%20Sheets/Data%20Library/DS_GEO_FloridaSPAN.pdf) is shown in Figure 15. This line extends from offshore Florida and crosses GUMBO3 in the continental domain (see Figure 10 for location). This profile has been used for validating the extent of the pre-salt basin. According to the interpretations from ION (Figure 15), the pre-salt section ranges in thickness between 1 and 4 km. The pre-salt thickness is ~3 km in the crossing point with GUMBO3.

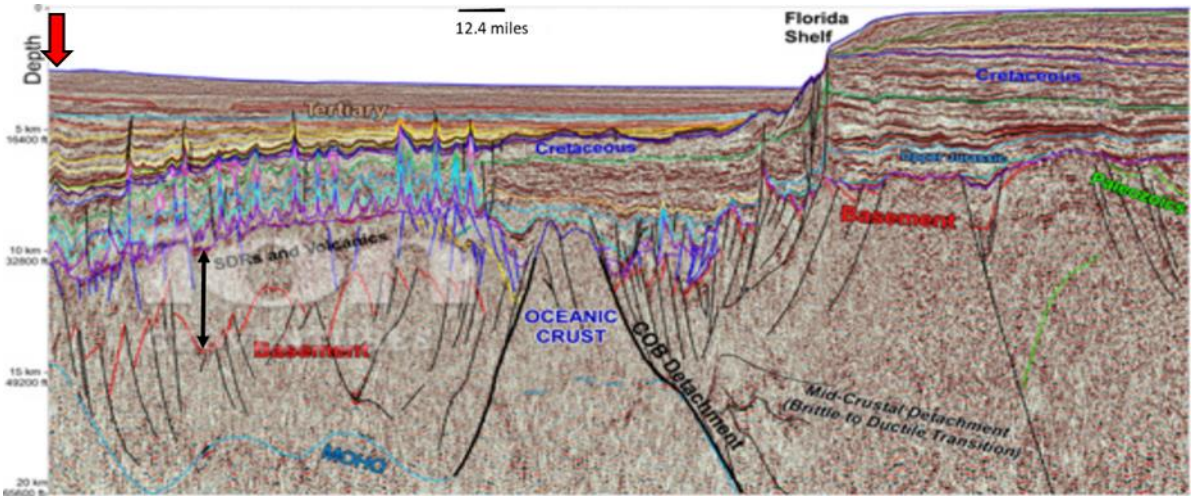

Figure 15. The profile from FloridaSPAN survey captioned from ION'S website (https://www.iongeo.com/content/documents/Resource%20Center/Brochures%20and%20Data%20Sheets/Data%20Sheets/Data%20Library/DS_GEO_FloridaSPAN.pdf). Pre-salt sedimentary section (indicated by a black arrow) is in between top of basement (red) and salt (purple). Red arrow marks where it crosses GUMBO3 in the continental region.

The profile from Snedden et al. (2014) extends from the Florida Platform margin to the edge of the Sigsbee Escarpment (Figure 10). It crosses the extinct spreading center, imaged in seismic data as a 45-km wide and 2 km deep valley. This profile was used to validate the location of one extinct spreading center. Figure 16 shows an axial graben in the basement that corresponds to the extinct spreading center.

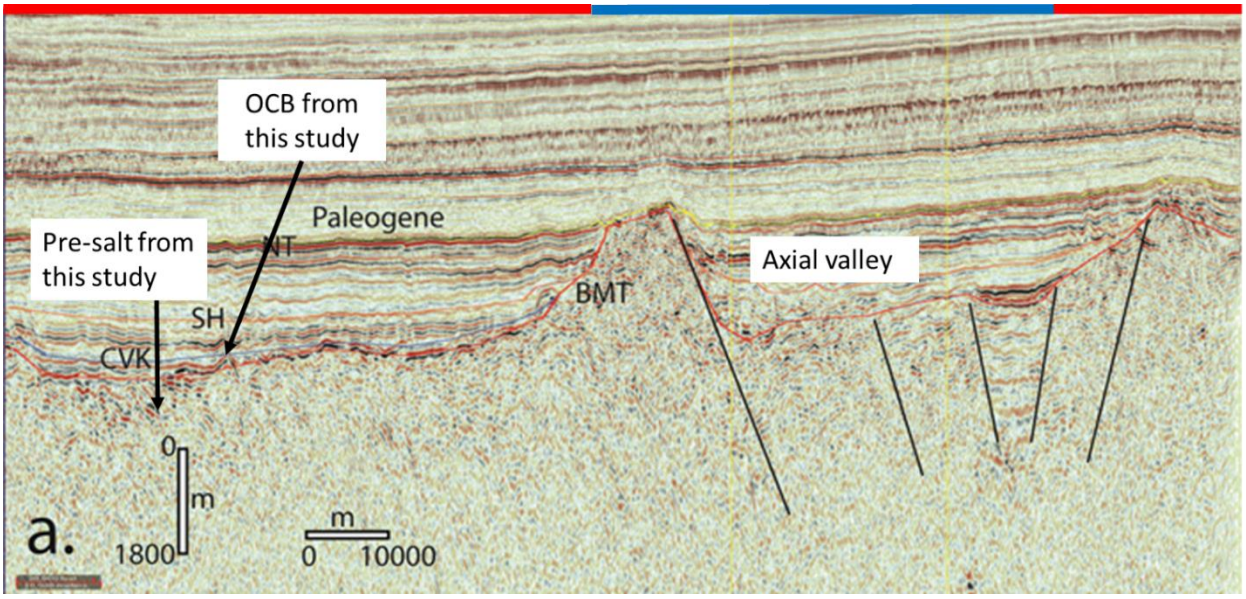

Figure 16. The profile from Snedden et al. (2014). The vertical scale is depth in meters. The graben-like structure in the basement is interpreted as an extinct spreading center. Color bar at the top of the figure indicates the gravity signal from filtered Bouguer anomaly map (Figure 30 a). The pre-salt section and the OCB from this study is marked in the figure. Red bar indicates gravity high and blue bar indicates gravity low. The correlation with gravity will be discussed later in Spatial Analysis and Discussion chapters. Notably, the location of the profile is not well constrained. CVK- Cotton Valley-Knowles. SH- Sligo-Hosston. NT- Navarro-Taylor. BMT- Oceanic basement.

2.3 Gravity data

Free-Air gravity field data collected by satellite (Sandwell et al., 2014) were used for this project (Figure 17). The reported accuracy of the gravity field is about 2 mGal (Sandwell et al., 2014).

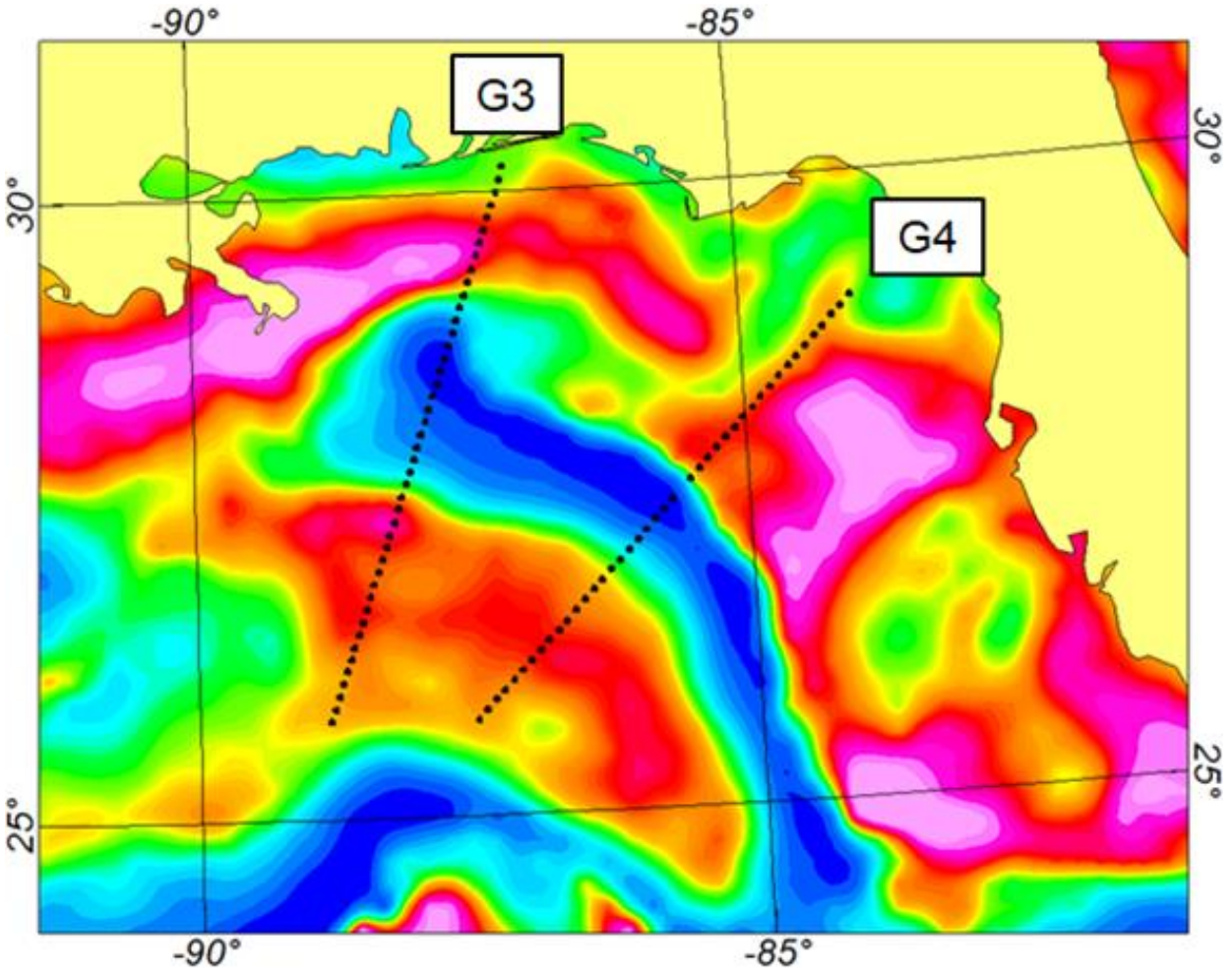

Figure 17. Free-air gravity field of the northeastern Gulf of Mexico. The dataset is from Sandwell et al., 2014. The warm color represents gravity highs and cool colors are gravity lows.

Gravity data are sensitive to the lateral density variations with the subsurface rocks. The original Free-Air data were used to build potential field models, while the Bouguer gravity anomaly (Figure 18) was computed for further spatial analysis. The Bouguer correction takes into account the gravity effect caused by the density contrast between water (density of 1g/cc) and subsurface rocks with assumed density of 2 g/cc. Equations 1 and 2 were used to calculate the Bouguer correction. The bathymetry data from Weatherall (2015) were utilized as h in Equation 2.

Bouguer anomaly=Free-Air gravity – Bouguer correction (Equation 1)

Bouguer correction= $2*\pi*G*\Delta\rho*h$ (Equation 2)

G=Gravitational constant ($6.67 *10^{-11}$ Nm^2/kg^2)

$\Delta\rho$ = density contrast (assumed to be -1 g/cc or -1000 kg/m^3)

h = thickness of water (from bathymetry data in m)

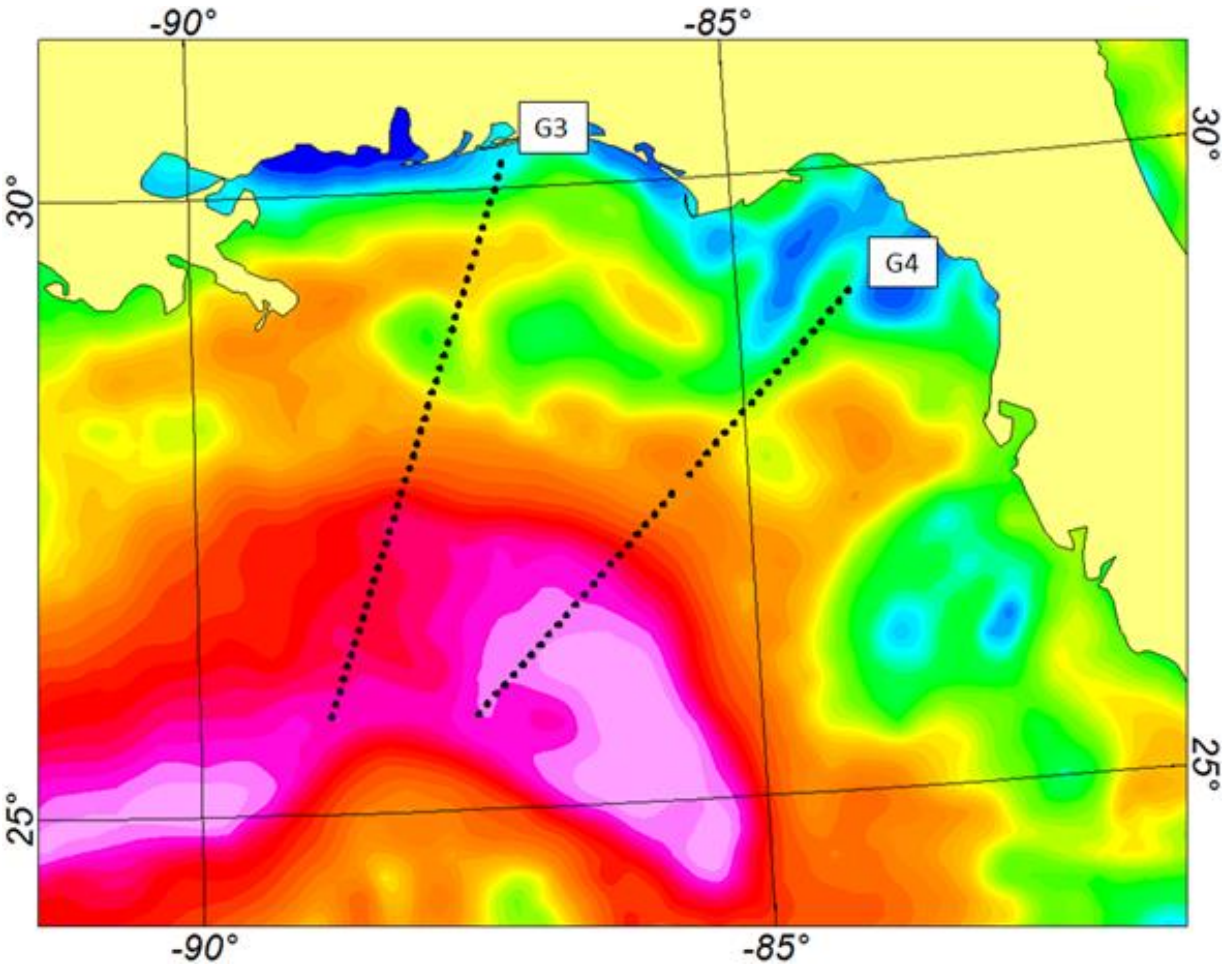

Figure 18. Bouguer Gravity anomaly of the northeastern Gulf of Mexico. The assumed Bouguer density is 2.0 g/cc. The bathymetry grid from Weatherall (2015) was used to compute the Bouguer correction.

2.4 Magnetic field

Two magnetic datasets were used for this project. The first one is EMAG2_V3 (Meyer et al., 2017; Figure 19a); it represents a compilation of satellite data with available airborne, marine and land surveys from the National Oceanic and Atmospheric Administration (NOAA). The spatial resolution of EMAG2_V3 is 2-arc-minute. This distance corresponds to approximately 3.6 km in the GoM region. As the most of this dataset is based on satellite measurements, its resolution is generally low. Nevertheless, EMAG2_V3 covers the entire study area. The second dataset comprises several USGS airborne and marine magnetic surveys (Bankey et al., 2002; Figure 19b), and thus has a better resolution than EMAG2_V3. The magnetic data from USGS has no coverage offshore Florida, which is within inside of the study area. Therefore, both datasets were used for different steps through this project. The USGS magnetic data were only used for subsurface modeling, while the spatial analysis was performed on the EMAG2_V3.

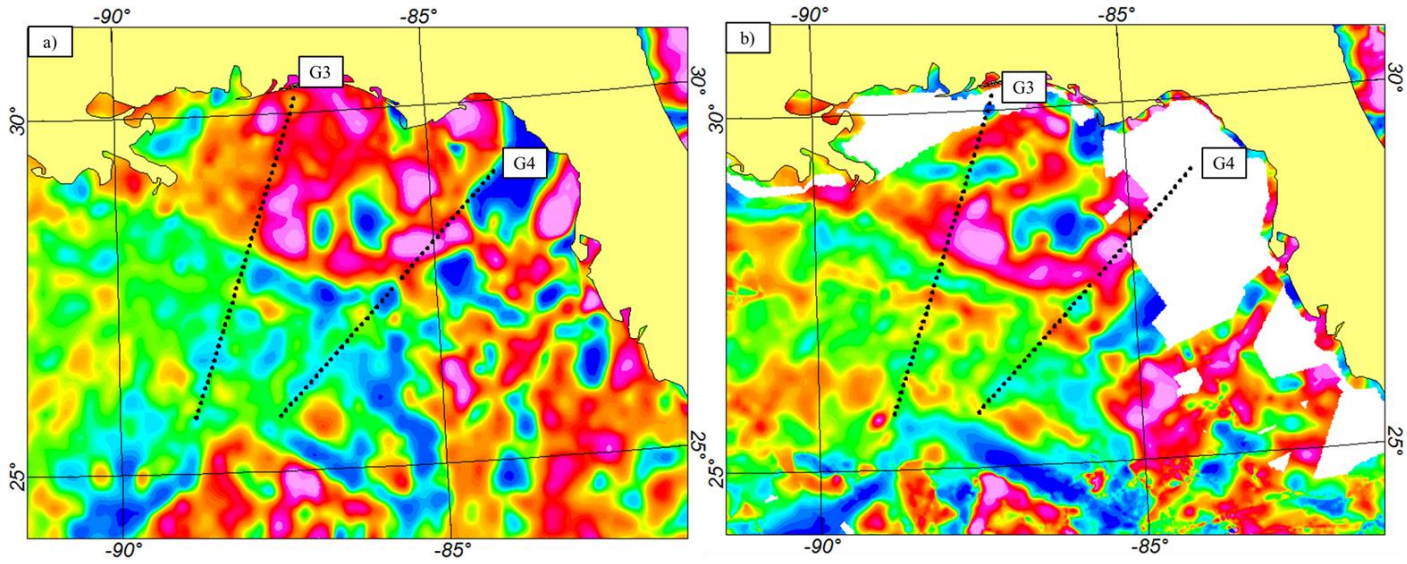

Figure 19. Total Magnetic Intensity of the northeastern Gulf of Mexico. a) The EMAG_V3 from Meyer et al., 2017. b) The USGS compilation from Bankey et al., 2002.

The EMAG_V3 dataset was reduced to the pole (RTP) to remove the skewness of magnetic anomalies due to non-verticality of an ambient magnetic field (Figure 20). According to NOAA, some grids and track line data collected from 1946 to 2014 have been included in EMAG2_V3. Most of the USGS magnetic data were collected in the year of 1985 in the northeastern GOM, so the following parameters were chosen for the reduction to the pole: inclination of 55.77 degrees, declination of 4.21 degrees, and total intensity is 48785 nT.

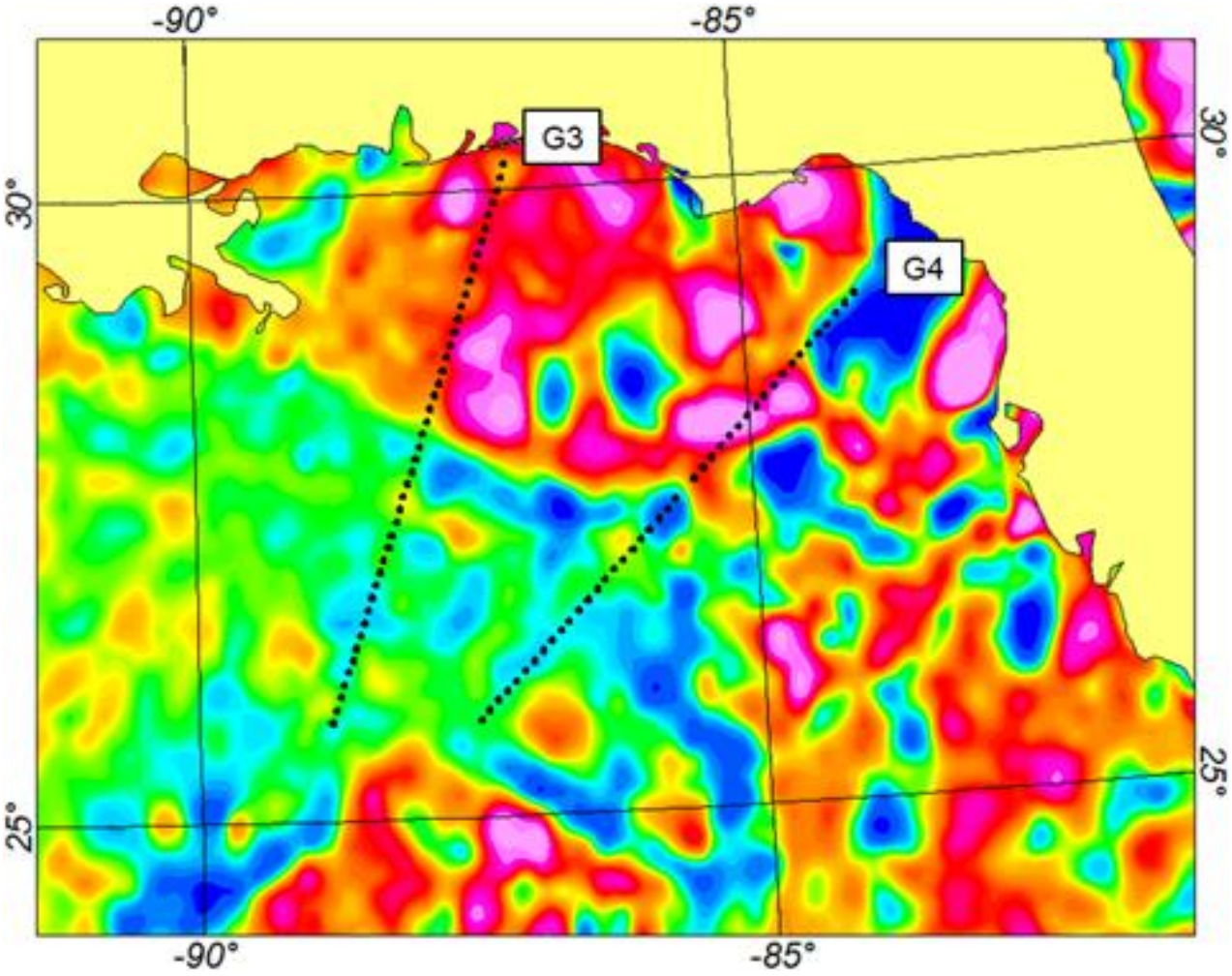

Figure 20. Reduced to the Pole (RTP) Magnetics of EMAG2_V3. The RTP parameters are: inclination of 55.7 degrees, declination of 4.21 degrees, and total magnetic intensity is 48785 nT (1985/01/01).

2.5 Bathymetry

The bathymetry data used in this study are from British Oceanographic Data Center (BODC)'s latest satellite data (Weatherall, 2015). The dataset has been gridded with a cell size of 1 km yielding a high resolution of bathymetric features in the basin (Figure 21). The bathymetry data were used for calculating the Bouguer correction and for validating the locations for seismic reflection profiles. Since the lines for modeling came from publications, the locations of the lines were georeferenced from maps. To validate the location, the match between seismic seafloor and real bathymetry was used. The good match in bathymetric features increases confidence in the correct location of lines.

2.6 Earthquakes in the northeastern GoM

The earthquake parameters were downloaded from a USGS earthquake catalog (https://earthquake.usgs.gov/earthquakes/search/). The locations of the earthquakes are plotted on the bathymetric map (Figure 21). The earthquakes in the study area occurring in the period from 01/01/1800 to 05/06/2018 are listed in Table 4. The majority of the earthquakes in the northeastern GoM have rather shallow focal depths, i.e. occurred within the sedimentary section. These shallow earthquakes are caused either by sedimentary slumps (gravity driven slope failure), or by salt tectonics. The magnitude of these shallow earthquakes is usually low. Although there are only three deep crustal events (with the focal depth > 14 km) recorded in the USGS catalog, they were more powerful than all earthquakes that occurred within the sedimentary section. Only two of these deep events have focal mechanisms reported by the USGS. Both of them are located in the oceanic region; their focal depth suggests the source in the crust or in the upper mantle. They both

show very similar stress distribution, suggesting compression forces oriented NE-SW. One of the focal mechanisms has a minor strike-slip component (although this is within error).

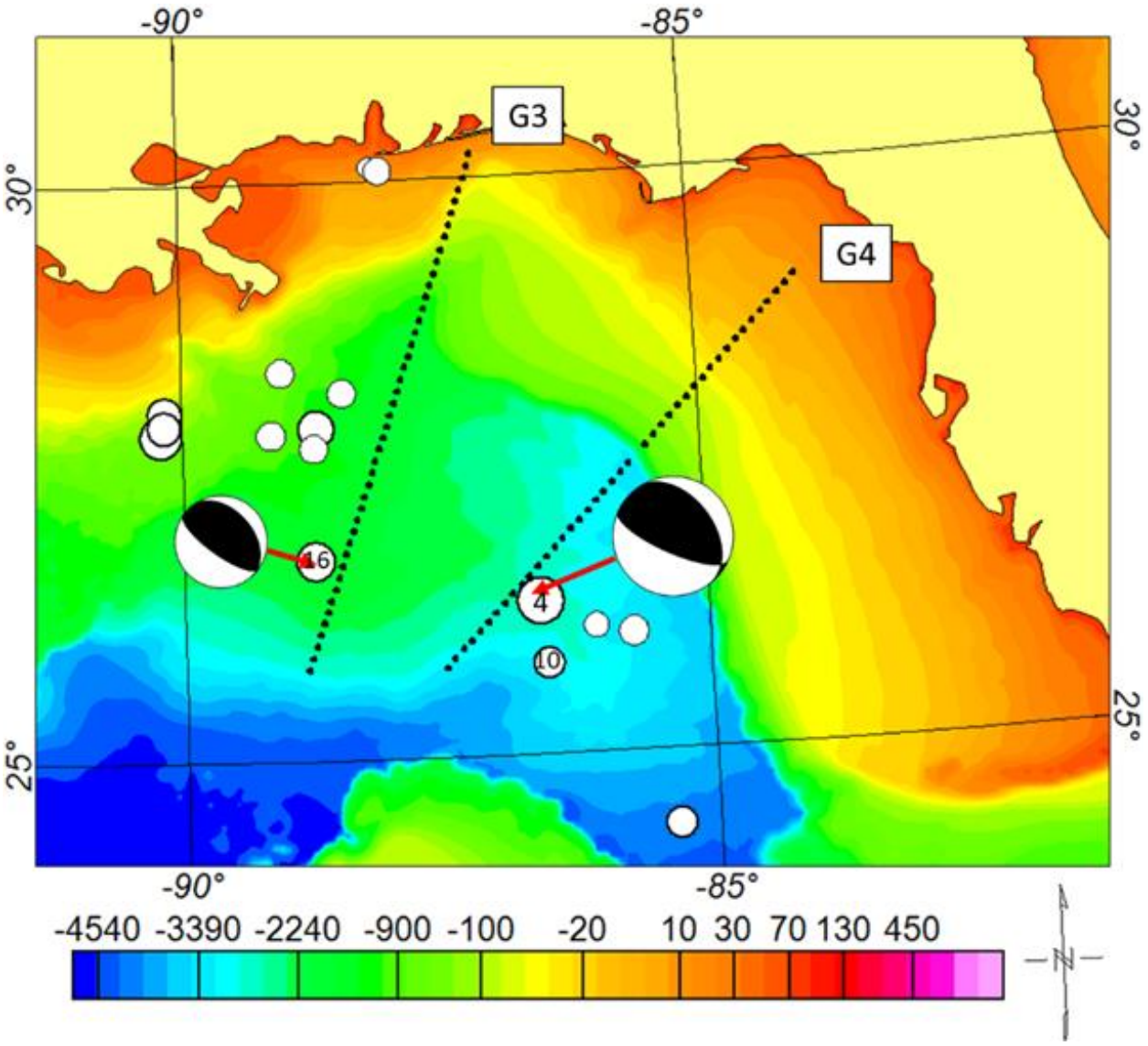

Figure 21. Bathymetric map of the northeastern Gulf of Mexico from British Oceanographic Data Center (BODC) from Weatherall, 2015. White dots are earthquake events occurred in the northeastern GOM since 1800 from the USGS earthquake catalog. The magnitude of the earthquake is proportional to the size of the circle with the largest 5.9 and the smallest 2.6. The majority of these occurred within sedimentary section and are related to the margin stability or salt tectonic processes. The three events with the focal depth >14km are highlighted by yellow. The focal mechanisms from USGS are shown for two of these deep crustal events. The numbers correspond to the earthquakes listed in Table 4.

One of these crustal events is located next to GUMBO3 (Figure 21; earthquake 16 in Table 4); it happened in 1978 and had a magnitude of 4.9. The depth of the earthquake was 33 km according to the USGS earthquake catalog. The strike of the fault is aligned with the orientation of the ridge segments (Figure 2b), however the earthquake is ~ 60 km to the north of interpreted extinct spreading centers. USGS lists two possible nodal planes: one with a strike of 319°, dip of 26°, and a rake of 102°, and another one with a strike of 126°, dip of 65°, and a rake of 84°. Another deep earthquake with magnitude of 5.9 occurred in near the line GUMBO4 (Figure 21; earthquake 4 in Table 4). This was the largest earthquake since 1800 in the eastern GoM. The location of earthquake 4 is in Figure 21. The depth of the earthquake was 14 km. The strike of the fault is also parallel to the ridge segments. The two suggested nodal planes are: strike of 324°, dip of 28°, and a rake of 117° or strike of 114°, dip of 65°, and rake of 77°. One more crustal earthquake (number 10 in Table 4) occurred in 1997 at the depth of 33 km in the oceanic region of the northeastern GoM. There is no information about focal mechanisms of this earthquake.

Table 4. Earthquakes occurring in the study area since 1800. The earthquake data are from USGS earthquake catalog (https://earthquake.usgs.gov/earthquakes/search/). The locations are shown in Figure 21. The earthquakes with the focal depth >14km are highlighted.

Earthquakes	Date	Latitude	Longitude	Depth (km)	Magnitude	Horizontal error	Depth error	Magnitude error	Focal mecha-nism
1	2018-05-06	27.871°N	88.678°W	10	4.6	7.1	1.9	0.042	None
2	2012-11-10	30.111°N	88.097°W	11	2.6	None	11.1	None	None
3	2011-02-18	30.080°N	88.001°W	5	3.5	None	None	None	None
4	2006-09-10	26.319°N	86.606°W	14	5.9	None	None	None	Yes
5	2006-02-10	27.828°N	90.210°W	5	5.3	None	None	None	No
6	2003-04-13	26.087°N	86.085°W	10	3.2	None	None	None	None
7	2002-09-19	27.822°N	89.135°W	10	3.7	None	None	None	None
8	2001-03-16	28.361°N	89.029°W	10	3.6	None	None	None	None
9	2000-12-09	28.027°N	90.171°W	10	4.3	None	None	None	None
10	1997-04-18	25.782°N	86.552°W	33	3.9	None	None	None	None
11	1994-06-30	27.911°N	90.177°W	10	4.2	None	None	None	None
12	1992-09-27	28.172°N	88.438°W	10	3.6	None	None	None	None
13	1992-03-31	26.019°N	85.731°W	5	3.8	None	None	None	None
14	1986-05-12	27.700°N	88.727°W	10	3.6	None	None	None	None
15	1980-01-10	24.353°N	85.380°W	10	3.9	None	None	None	None
16	1978-07-24	26.729°N	88.743°W	33	4.9	None	None	None	Yes

2.7 Well data

Well data were obtained from the Bureau of Ocean Energy Management website (BOEM). Two well reports were used to constrain the depth to the top of the carbonate platform along GUMBO3 profile and GUMBO4 profile. The locations of these two wells are shown in Figure 10. Well No Logs G2468, which was operated by Gulf Oil Corporation in 1975. The API number of the well is 608224001200. The top of the carbonate platform is at a depth of 300 ft (Figure 22a). This well is close to GUMBO3 profile and was used to constrain the model. Well No. 1 O.C.S.-G-2516, which was operated by Texaco Inc, sampled the cores in 1975. The API number of this well is 608284000000. The top of the carbonate platform is located at 1250 ft along GUMBO4 profile (Figure 22 b). According to the biostratigraphy information provided in the well report, the top of the carbonate platform is younger than upper Cretaceous.

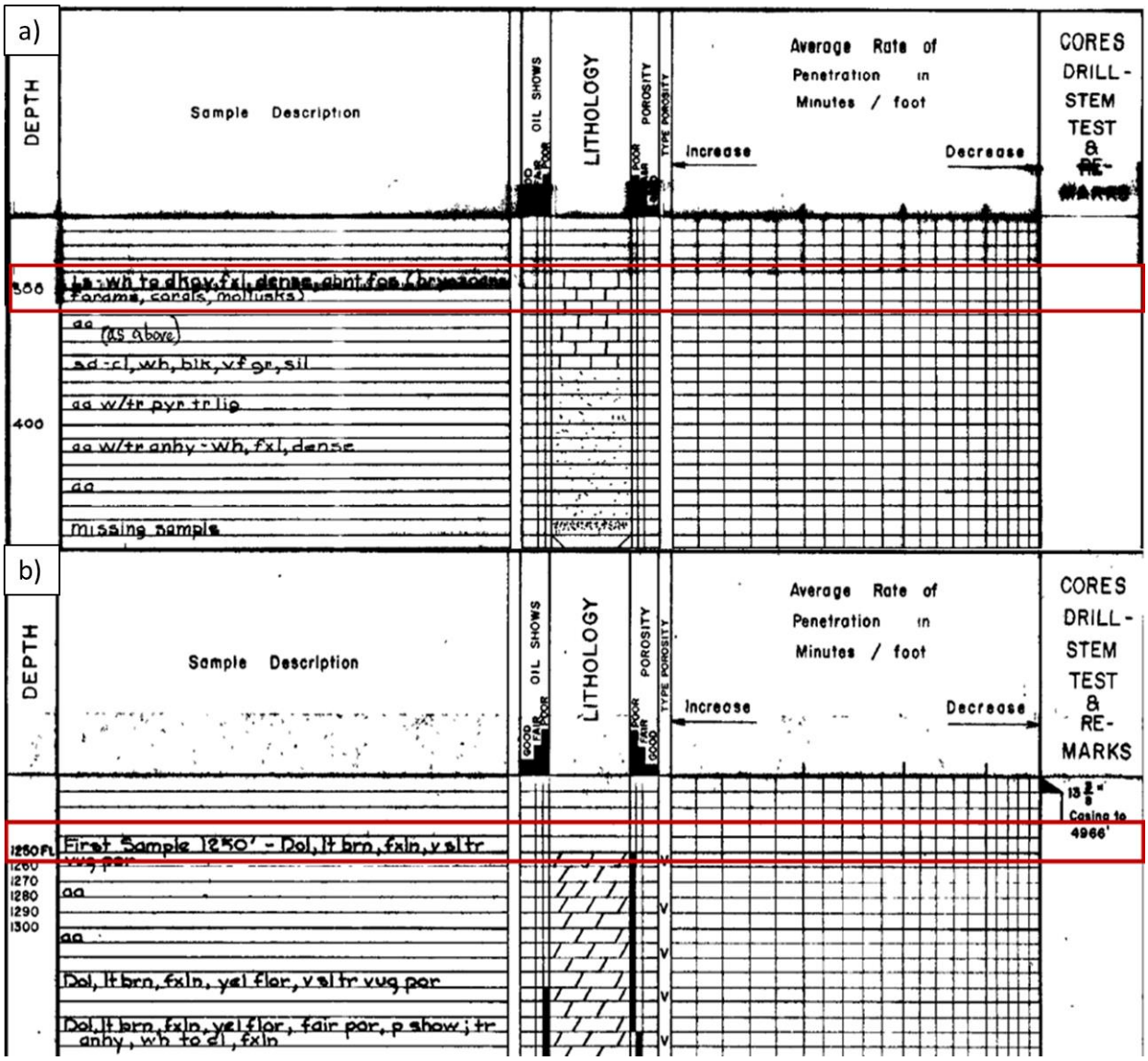

Figure 22. a) Well log report of well No Logs G2468. The top of limestone is at 300 ft (red box). b) Well log report of well No. 1 O.C.S.-G-2516. The top of dolomite is at 1250 ft (red box).

The basement penetration from DSPD Leg 77 Site 537 allowed scientists to calculate the bulk density of the upper continental crust by using the Gamma Ray Attenuation Porosity Evaluator (GRAPE) (DSDP LEG 77, Volume LXXVII). The bulk density of the upper continental crust is ~2.75 g/cc, (DSDP LEG 77, Volume LXXVII)

which was used as the constraint for the two-dimensional subsurface modeling in the following chapter.

The multiple velocity-density pairs from 447 deepwater wells in GoM from Hiltermann et al. (1998) were used by Filina et al., (2015) to determine the general density-velocity trend. Although the well data from Hilterman et al. (1998) were not explicitly used in this study, the derived densities for individual sedimentary layers from Filina et al. (2015) and Filina (2017) were utilized during the modeling of the gravity data.

CHAPTER 3. Integrated Geophysical Modelling

Three 2D subsurface models were built for this project along published seismic profiles (Figure 7). The first model was aligned with seismic transect GUMBO3 (Eddy et al., 2014). As the seismic reflection and refraction data for this line show some disagreement in Moho interpretation (Figures 5 and 8), two versions of Model 1 were developed. Model 1A followed seismic refraction data (Figure 5), and Model 1B was built on seismic reflection data, suggesting shallower Moho (Figure 8). The second model was aligned with line GUMBO4 from Christeson et al., 2014 (Figure 6). The third model was developed along a seismic reflection line from Horn et al., 2017 (Figure 12).

Generally, the first step in the modeling is to split the subsurface into a number of layers and then assign the physical properties (density and magnetic susceptibility) of each layer based on additional constraints, such as well data or published values for various types of rocks. The potential fields' response was computed for each model and compared with the observed signal. The model was then adjusted in order to ensure a good match between observed and computed signals in both gravity and magnetic data. Thus, the resultant model should remain geologically valid and agree with all available data – seismic, gravity, magnetics and wells.

3.1 Models 1A and 1B

Profile GUMBO3 has a total length of 534 km. Both models 1A and 1B were composed to a depth of 40 km (Figure 23), comprising 19 layers with various densities and

magnetic susceptibilities. The top ~10 km consists of seven sedimentary layers with their modeled densities, respectively: Pleistocene (2.25 g/cc), Pliocene (2.35 g/cc), Miocene (2.4 g/cc), Paleogene (2.45 g/cc), Mesozoic (2.55 g/cc), salt (2.15 g/cc), carbonates (2.6 g/cc), and pre-salt (2.55 g/cc). The density values of sediments (excluding the pre-salt deposits) were converted from velocity from 447 deepwater wells by Hiltermann et al. (1998) and from Filina (2017). The multiple velocity-density pairs from 447 deepwater wells in GoM from Hiltermann et al., 1998 were used by Filina et al. (2015) to determine the general density-velocity trend. All sedimentary layers are assumed to be non-magnetic, i.e., their magnetic susceptibility is 0 cgs. The profile from Rodriguez (2011) crosses GUMBO3 (see Figure 10 for location). It was used to constrain the thickness of the sediments in the first model. The seismic reflection data in the crossing point (Figure 13) was converted from two-way travel time to depth by using the GUMBO3 seismic velocities at the same point. The well G2468 (Figure 22) located 8 km away GUMBO3 was used to constrain the top of the carbonate platform (91.44 m or 300 ft).

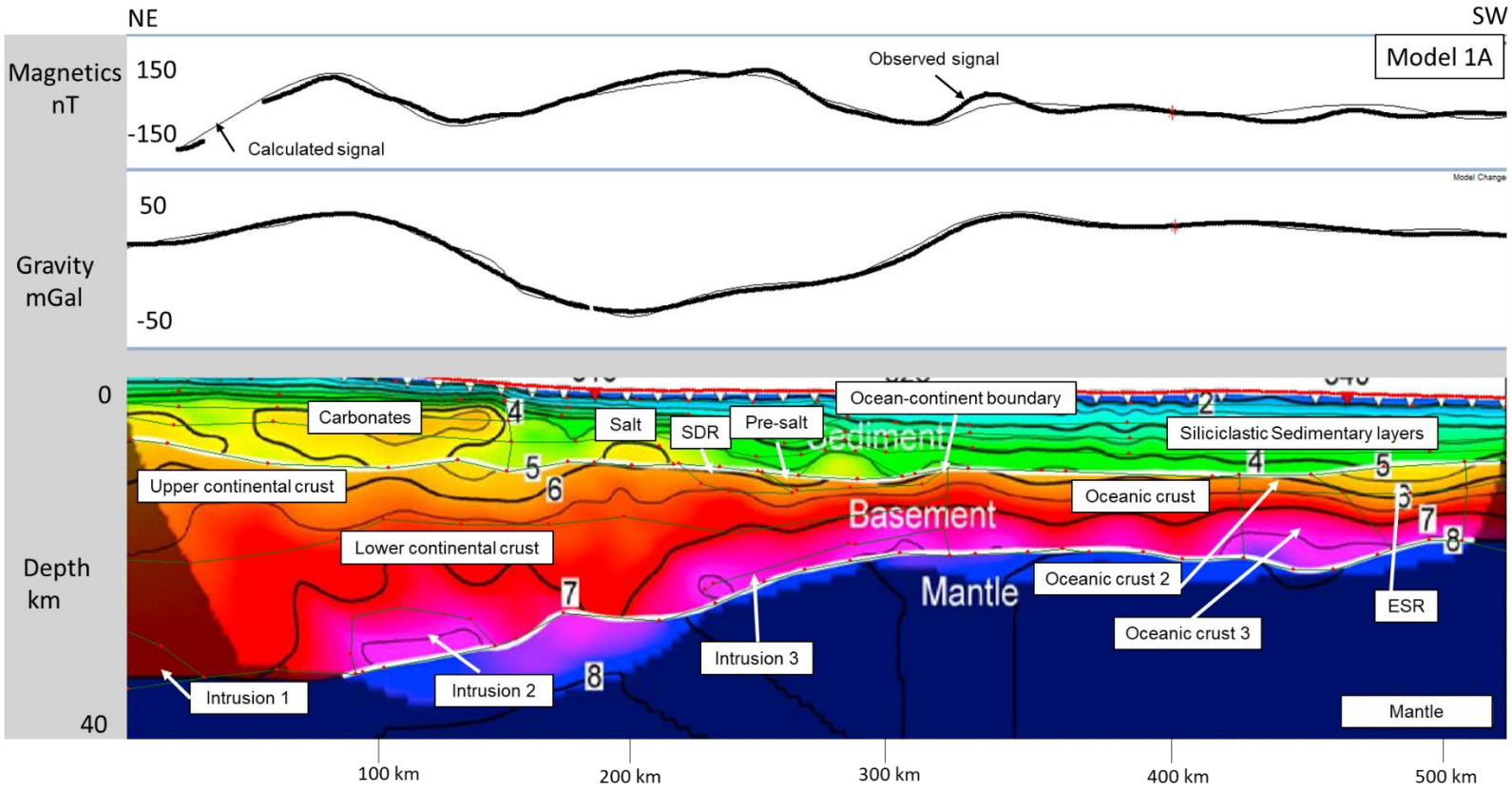

Figure 23. Integrated subsurface Model 1A. This model is aligned with the line GUMBO3; it was built based on seismic refraction data from Eddy et al., 2014. The top two panels are potential fields: the dots are observed data; the solid black lines are computed ones for the model shown in the bottom panel. Different colors in the bottom panel are seismic velocities. SDR-Seaward dipping reflector. ESR- Extinct spreading ridge

The crust along this profile changes from a barely stretched continental one in the beginning of the line to a much thinner oceanic one at the end of the line. The bottom layer of the model is mantle with a density of 3.3 g/cc and 0 cgs magnetic susceptibility (Filina, 2017). In a continental domain, the crust is composed of two layers – the upper and the lower continental crust units. The upper continental crust is ~6-~13 km thick. This layer has a density of 2.75 g/cc constrained by the only basement penetration in the Gulf of Mexico (DSDP LEG 77, Volume LXXVII) and magnetic susceptibility of 0.003 cgs (converted from Filina, 2017). The SDRs are modeled in the upper continental crust with a density of 2.75 g/cc and magnetic susceptibility of 0.005 cgs. The SDRs has a horizontal extent of 20 km from Eddy et al. (2014) and a depth of 3 km in the upper continental crust. The pre-salt sedimentary basin is bounded by SDRs in the north and by the OCB in south. The density of a pre-salt section is assumed to be 2.55 g/cc and magnetic susceptibility is assumed as 0 cgs. The crustal necking zone – the region in the continental domain where crustal thickness changes from ~17 km to ~10 km - is located from 200 to 310 km along the model.

The lower continental crust has not been drilled and was assumed to have a higher density of 2.9 g/cc (Carlson and Herrick, 1990) and a higher magnetic susceptibility of 0.008 cgs. The magnetic susceptibility is determined during the modeling, but this value is generally consistent with the range (6.9 +/- $2.0*10^{-3}$ cgs) published for the rocks of the lower continental crust (Schnetzler, 1985). The OCB is interpreted at the distance of 310 km, which is coincident with a prominent magnetic signature. The location of the OCB is very sensitive to the magnetic signal, so there is not much room to adjust the location for the OCB. The model suggests the presence of three anomalous bodies (intrusions 1 - 3) in

the lower continental crust that span approximately between the following distances: 0 - 29 km, 87 - 140 km and 219 - 310 km. The intrusive bodies are modeled with a density of 2.95 g/cc and magnetic susceptibility of +/-0.01 cgs. The presence of intrusive bodies is dictated by the magnetic signal. Potential field modeling does not have a unique solution. The signal calculated for a subsurface model depends on geometries and physical properties of the rocks in the subsurface. Thus, the depths of these intrusive bodies cannot be uniquely determined by magnetic data alone. However, several zones of fast seismic velocities (~7.5 km/s) are mapped in the refraction experiment (Figure5). Intrusion 2 and 3 are coincident with those fast Vp zones, which make them consistent with intrusive bodies – highly magnetic and fast Vp. Intrusion 1 is not covered by seismic data (shaded zone in Fiugre5), so it is the least constrained part on Model 1A, but its presence is suggested by magnetic signal. The first two intrusions require reverse magnetic susceptibility in order to match the observed magnetic signature.

Toward the center of the basin, oceanic crust was modeled from 310 to ~420 km along the line. Since the seismic data for this line show some disagreement in the crustal thickness (see Seismic Reflection Data section), two models were developed for the line GUMBO3. The first model, shown in Figure 23 includes the oceanic crust composed of two layers based on seismic velocities (basaltic upper layer with Vp varying from 6 to 6.5 km/s and lower oceanic crustal layer composed of gabbro with velocities of 6.5-7.5 km/s). However, this crust appears to be thicker than normal from seismic refraction data. The density of upper oceanic crust is 2.65 g/cc (Carlson and Herrick, 1990) and magnetic susceptibility is assumed to be 0.007 cgs, which is consistent with the magnetic susceptibility of basalt (Clark and Emerson, 1991). The density of lower oceanic crust was

2.95 g/cc (Carlson and Herrick, 1990) and the derived magnetic susceptibility was 0.008 cgs, which agrees with the magnetic susceptibility of gabbro (Clark and Emerson, 1991). The extinct spreading center, which is observed as a seismic velocity decrease in the GUMBO3 profile (Figure 5), was also composed of two layers with the same density as oceanic crustal units, but the magnetic susceptibilities of 0.006 cgs and 0.0009 cgs for the upper and lower ridge respectively. These values were derived from magnetic modeling and are within the published range of Schnetzler (1985).

For the alternative model - Model 1B shown in Figure 24 - the seismic reflection data (Figure 8) were used as a constraint. The difference from the previous model is in the oceanic domain adjacent to the OCB. In the previous model, the oceanic crust was 10 km thick based on refraction data (Figure 5). In the seismic reflection data for the same line, the oceanic crust near the OCB appears to be 4 km thinner. In the alternative model, this crust was modeled as one layer with density 2.85 g/cc and magnetic susceptibility of 0.0075 cgs. These values were used to model a thinner oceanic crust for the adjacent Model 2.

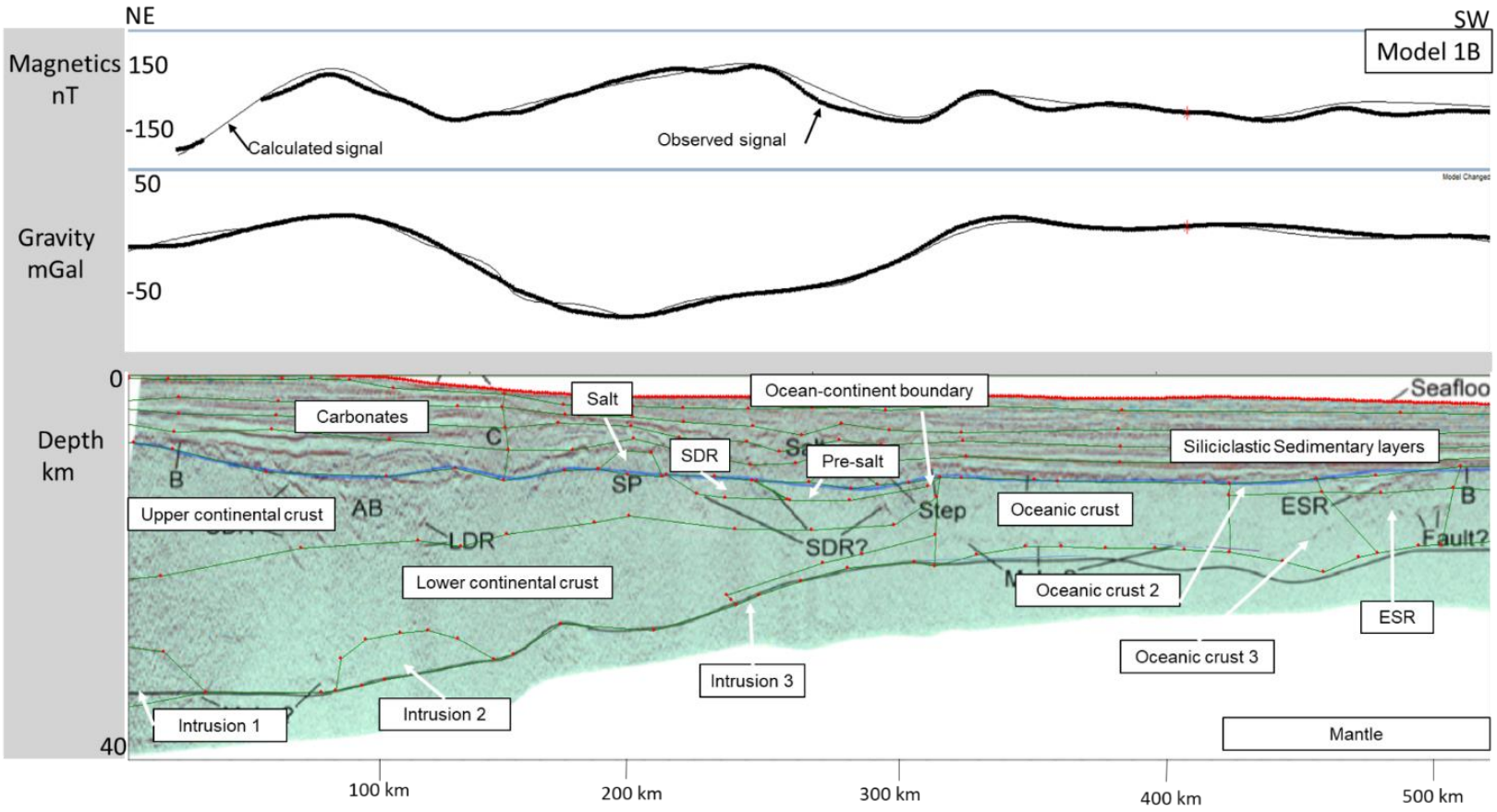

Figure 24. Integrated subsurface Model 1B (the location coincides with Model 1A). This model is based on Moho interpretation from seismic reflection line Fugro533. The Moho from previous model (Figure 23) is shown as a black line. To satisfy the observed potential fields signals, the thickness of the upper continental crust was adjusted (see text for details).

As already stated above, potential fields modeling does not yield a unique solution for the subsurface structures as it responds to a combination of geometry (thicknesses and geometric shapes of modeled layers) and physical properties (densities and magnetic susceptibilities). That is why every potential fields model requires some constraints to either geometries (from seismic data) and/or physical properties (from wells or from published values for different types of rocks, such as in Telford et al. (1990). Model 1B along Fugro533 (Figure 24) shares the same location as Model 1A and GUMBO3. It also comprises 20 different layers. Most of the structures and physical properties of the subsurface rocks are the same as in the previous model with the exception of the Moho interpretation near the OCB, which is imaged shallower in seismic reflection data (Figure 8) than in seismic refraction data (Figure 5). In order to accommodate the misfits in the gravity and magnetic signals generated due to changes in the crustal thickness and properties, the boundary between the upper continental crust and the lower continental crust has been adjusted geometry slightly in Model 1B. The mid-crustal boundary is the least constrained one, while the basement and Moho are constrained by seismic refraction database (Ibrahim et al., 1981). Both Model 1A and 1B are geologically valid with the same physical properties, so no conclusion can yet be drawn as to which model is more realistic at this stage. The density value of upper continental crust was adjusted to 2.77 g/cc and of lower continental crust was adjusted to 2.95 g/cc in order to compensate the gravity mismatch.

3.2 Model 2

Model 2 is aligned with GUMBO4 (Figure 6). This model has a total length of 510 km and thickness of 40 km (Figure 25). It comprises 17 layers with various densities and magnetic susceptibilities. Compared to GUMBO3, the model along GUMBO 4 does not have salt and SDR layers. The physical properties of all layers are the same as Fugro 533. Similar to GUMBO3, GUMBO4 has ~10 km thick sediments. The thickness of siliciclastic sedimentary layer was modeled the same as GUMBO3. The top of the carbonate platform at 381 m (1250 ft) was constrained from the well No. 1 O.C.S.-G-2516 (Figure 22). The necking zone along the line GUMBO4 is located from ~196 km to 295 km, and shorter than the one observed for GUMBO3.

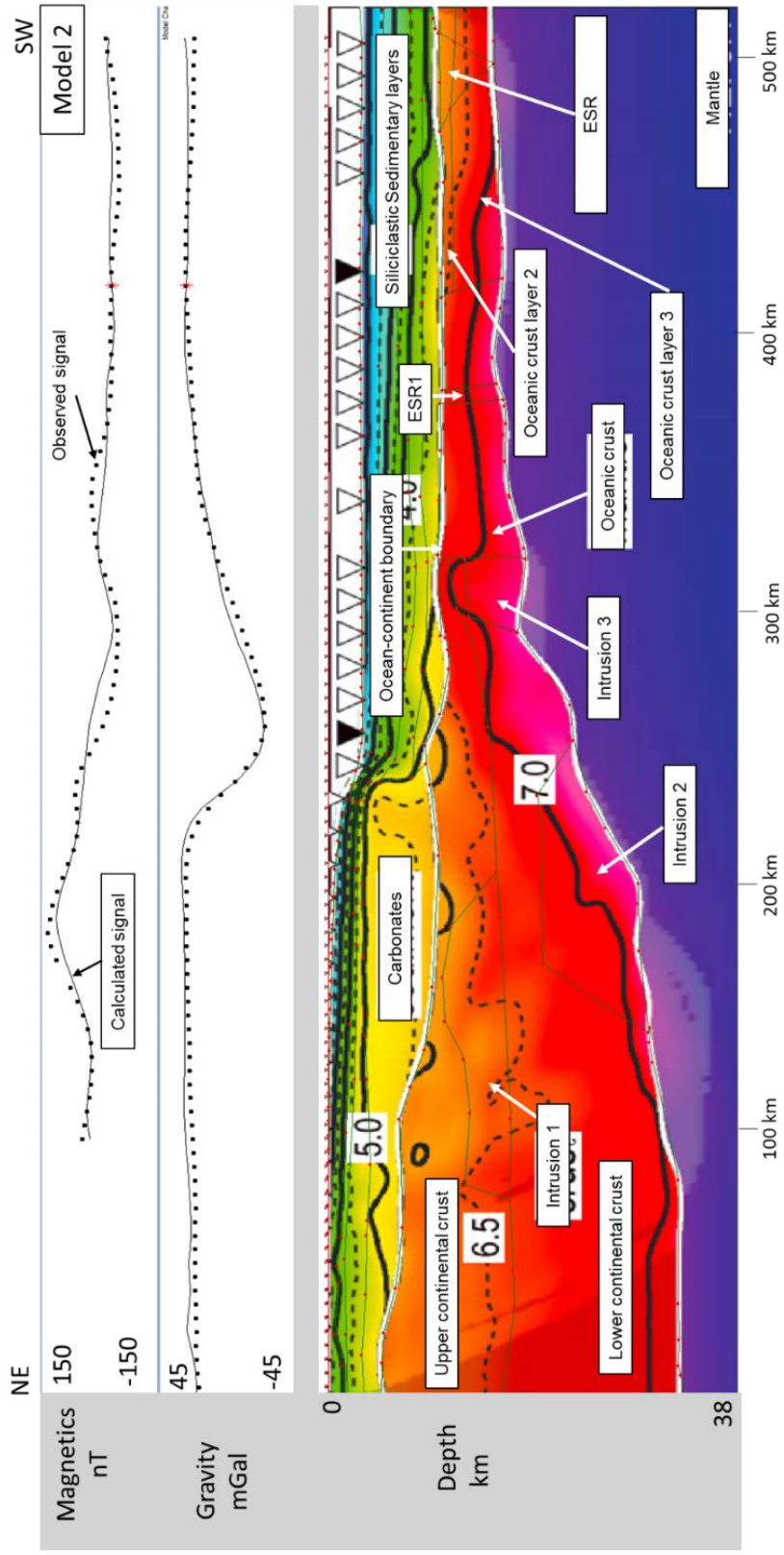

Figure 25. Model 2 aligned with profile GUMBO4 from Christeson et al., 2014. Refer to Figure 23 for description.

The OCB is located at 295 km. The oceanic crust close to OCB has been modeled as a single layer with a density of 2.85 g/cc and magnetic susceptibility of 0.0075 cgs. The one-layer structure is suggested by the distribution of seismic Vp velocities (Figure 6). Since the oceanic crust near the OCB does not show significant variations in Vp (7.0 km/s), only one layer of oceanic crust was used for the segment extending from 295 km to 399 km. From 399 km to the end of the profile, the oceanic crust has been modeled with two layers as guided by seismic refraction data. The physical properties of all subsurface rocks are the same as used for Models 1B. The extinct spreading center corresponds to the velocity decrease from 460 km-497 km. The extinct spreading ridge (ESR) is located at the end of the profile, which is consistent with Model 1A and 1B. An additional ESR1 structure was added in the center of the one-layer segment of the oceanic crust in order to match the observation from spatial analysis that will be discussed in Chapters 4 and 5. This additional ridge structure is located roughly in the center of the one-layered oceanic crust and is 5 km wide, too narrow to be detected from seismic refraction (the distance between the instruments was 12 km in GUMBO4).

Several intrusive bodies in the lower crust were included in the model, similarly to the ones shown in models 1A and 1B. However, some of them are slightly different from those in GUMBO3. The first intrusive body is located in the continental domain at distances of 73 to 192 km. Unlike GUMBO3, the seismic refraction data along GUMBO4 shows the velocity structure at the mid-crustal boundary is somewhat rugose, so the intrusive body 1 was placed between the upper and the lower continental crustal units based on the seismic refraction profile (Figure 6). The intrusion 2 starts at 73 km and ends at 241 km. The intrusion 3 was added based on the magnetic signal from 279 km to 295 km.

3.3 Model 3

Model 3 is located along Horn et al.'s (2017) profile (Figure 26). It has a length of 1071 km, extending from offshore Florida to the Yucatan margin (Figure 10). Model 3 consists of 19 layers up to depth of 36 km. The subsurface rocks were assigned the same physical properties as all four models (Table 5). At this line crosses GUMBO3, the thicknesses of individual subsurface layers were tied with GUMBO3 at the crossing point. The thickness of continental crust at the beginning of the line is restricted by GUMBO4 since the lines are only 47 km apart. In addition, the pre-salt deposits and several salt bodies were included in the model guided by seismic reflection images (Figure 12).

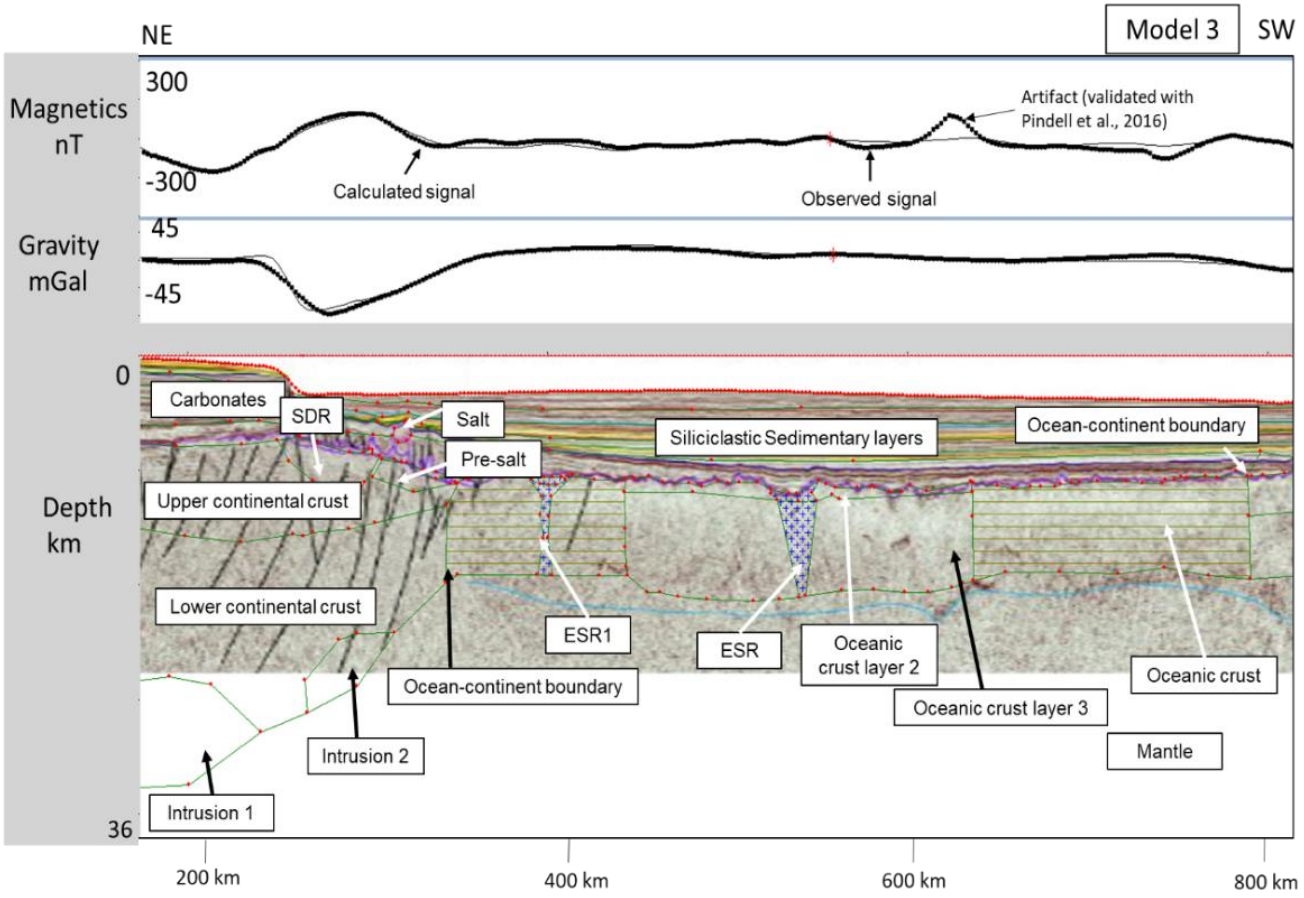

Figure 26. Integrated subsurface model 3. This model is aligned with a profile from Horn et al. (2017). The physical properties of modeled layers are listed in Table 5. ESR- Extinct spreading ridge. SDR-Seaward dipping reflector.

Model 3 crosses two OCBs. The first one is located in the northeastern GoM at ~346 km, which corresponds to a magnetic trough. The second OCB is located in the Mexican sector approximately 796 km along the line, which also is aligned with a trough in the magnetic signal. The pre-salt deposits are imaged on the stretched continental margins on both sides of the profile. The rifting necking zone in the northern part of this model (248 - 346 km) is comparable to GUMBO4 but shorter than GUMBO3. The continental crust on both sides of the line was modeled with two layers, i.e. the upper and lower continental crustal units with the same physical properties as in the other models (Table 5). Two intrusions were added to the continental crust in the northeastern GoM at the following distances: 107-246 km (intrusion 1) and 270-322 km (intrusion 2). Both of the intrusions are located in the lower continental crust in order to fit the gravity and magnetic signal. Intrusion 1 has a reverse magnetic polarity and is modeled with a magnetic susceptibility of -0.01 cgs, which is consistent with Model 1A, 1B. Intrusion 2 has a positive magnetic polarity and is modeled with a magnetic susceptibility of 0.01 cgs, which is also consistent with Model 1A, 1B, and 2.

As Model 3 is located in the region between GUMBO3 and GUMBO4 lines, it allows study of the transition zone(s) between two distinct crustal domains imaged by those profiles. GUMBO3 (Figures 5 and 8) shows generally thicker oceanic crust (9 km thick), while the oceanic crust along GUMBO4 is dramatically thinner (~5 km) and shows a different velocity profile (Figure 6). Model 3 (Figure 25) shows three distinct crustal zones in the oceanic domain. The first zone spans from the OCB in the northeastern part of the line (346 km) to 447 km; it is consistent with one-layered (gabbroic) thinner crust, similar

to the one imaged with Model 2 (GUMBO4) with a density and magnetic susceptibility of 2.85 g/cc and 0.0075 cgs. The extinct spreading ridge in the center of the one-layer crust (ESR1) was modeled with a density and magnetic susceptibility of 2.85 g/cc and 0.009 cgs. This distinct feature was observed as gravity low in spatial analysis (See Chapter 4), so it was added to be consistent with spatial analysis. Further, between 440 km and 638 km, the crust is consistent with thicker two-layered (basaltic and gabbroic) one, imaged by Models 1A and 1B (GUMBO3) with densities 2.65 g/cc and 2.95 g/cc respectively, and corresponding magnetic susceptibilities of 0.007 cgs and 0.008 cgs. From 638 km to 796 km (the OCB on the Yucatan side), the oceanic crust was modeled with single gabbroic layer again. The ESR was determined in a middle of a two-layered segment between 544 km and 612 km in order to match magnetic signal. The changes in the oceanic crustal structure observed along this line are consistent with the overall variations of oceanic crust observed for GUMBO3 and GUMBO4 and will be addressed in detail in the Discussion section below. Notably, the sharp bump at the model distance of 618-638 km has a magnetic signal that is an artifact in the public magnetic datasets. This bump was not observed in Pindell et al. (2016)'s regional aeromagnetic data.

From the three models described above, the density and magnetic susceptibility of subsurface rocks have been derived. They are listed in Table 5. The physical properties of the corresponding layers that are derived from these four models (Model 1A and 1B, 2, 3) are either constrained by the well data (sedimentary layers and upper continental crust) or with published values. The intrusions in the necking zone have consistent positive magnetic susceptibility. The OCB is located at model distance of 310 km in Model 1A and 1B, at model distance of 295 km in Model 2, and at model distance of 346 km in Model 3. The

derived OCB locations from the four models correspond to magnetic troughs with uncertainty within 7 km. The ~3 km thick pre-salt section from Model 1A and 1B is modeled in order to match the magnetic signal, but is not observed from seismic refraction data (Figure 5), nor can be confidently identified in the seismic reflection data (Figure 8). There is no pre-salt section in the Model 2 (GUMBO4) and it is only 1 km thick in Model 3. Several intrusions of various magnetic polarity (positive or negative) were modeled primarily based on the characteristics of Vp from refractions and based on magnetic anomalies. The depths of major modeled horizons are consistent between all the models as listed in Table 6.

Table 5. Physical properties of the subsurface layers for all three models.

Layer in the model	**Density (g/cc)**	**Magnetic susceptibility (cgs)**
Pleistocene	2.25	0
Pliocene	2.35	0
Miocene	2.4	0
Paleocene	2.45	0
Mesozoic (including the pre-salt sediments)	2.55	0
Carbonates	2.6	0
Salt	2.15	0
SDR	2.75	0.005
Upper continental crust	2.75 2.77 for Model 1B	0.003
Lower continental crust	2.9 2.95 for Model 1B	0.008
Intrusions1 and 2 in Models 1A and 1B Intrusion 1 in Model 3	2.9	-0.01
Intrusion 3 in Models 1A and 1B Intrusion 2 and 3 in Model2	2.9	0.01
Intrusion 1 in Model 2	2.75 (upper crust)	0.01
Oceanic crust layer 2	2.65	0.007
Oceanic crust layer 3	2.85	0.008
One layered oceanic crust	2.85	0.0075
ESR (upper layer)	2.65	0.006
ESR (lower layer)	2.95	0.009
ESR1 in one-layered crust	2.85	0.009
Mantle	3.3	0

Table 6. The depth to major layers boundaries in km measured at the beginning and the end of the modeled profiles.

	Depth at the beginning of the line, km			Depth at the end of the line, km		
	Models 1A and 1B, GUMBO3	Model 2, GUMBO4	Model 3, Horn et al., 2017	Models 1A and 1B, GUMBO3	Model 2, GUMBO4	Model 3, Horn et al., 2017
Top of carbonate	2.07	1.42	2.88	N/A	N/A	N/A
Top of basement	7.61	4.98	4.95	9.9	10.15	9.38
Mid-crust boundary	19.42	19.27	19.25	11.79	12.15	12.34
Moho	33.33	33.35	35.05	19.46	15.52	17.09

Chapter 4. Spatial Analysis of Gravity and Magnetic Fields

4.1 Filtering of potential fields

Potential fields (gravity and magnetics) are sensitive to lateral variations in physical properties of the rocks in the subsurface. Different rocks have different densities and magnetic susceptibilities (Telford, 1990). Major geological boundaries represent the contacts between the rocks of different type (OCB, SDR, basement faults). These contacts are associated with some signals in the potential fields and these signals may be different amplitude and wavelength depending on the magnitude of the contrast in physical property, geometry, and depth of the contact between juxtaposed rocks. Hence, the recorded potential fields represent the superposition of all the signals due to various geological structures in the subsurface. In order to highlight the specific one that this study focused on, which is the crustal layer structures, the other signals need to be removed. A series of corrections were made to take into account the known sources of potential fields' signals, such as the Bouguer correction in gravity and reduction to the pole in magnetics. The effects of deeper sources (Moho and below) could also be removed by estimating and subtracting the regional trend from the observed potential field. Further, a series of filters (mathematical transformations) may be applied to highlight the crustal signatures that focus on the regions where the fields change the most.

The gravity effect of water contacting with unconsolidated sediments of the seafloor was calculated and removed from the observed Free-Air gravity anomaly (see Geophysical Data section for details). The resultant Bouguer gravity anomaly is shown in Figure 18. The regional gravity trend, representing the signal from the deep sources (Moho

and below), was computed via application of the upward continuation filter to the Bouguer gravity anomaly to the level of 40 km and then removed from the Bouguer gravity anomaly. The resultant residual Bouguer gravity anomaly is shown in Figure 27. It represents the gravity effects for all sources between the mudline and Moho, such as salt in the sedimentary cover and variations within the basement. As the salt is generally much shallower in the section, its signature is usually manifested by short-wavelength anomalies, while the basement and the rocks variations within the crust are usually associated with wider anomalies.

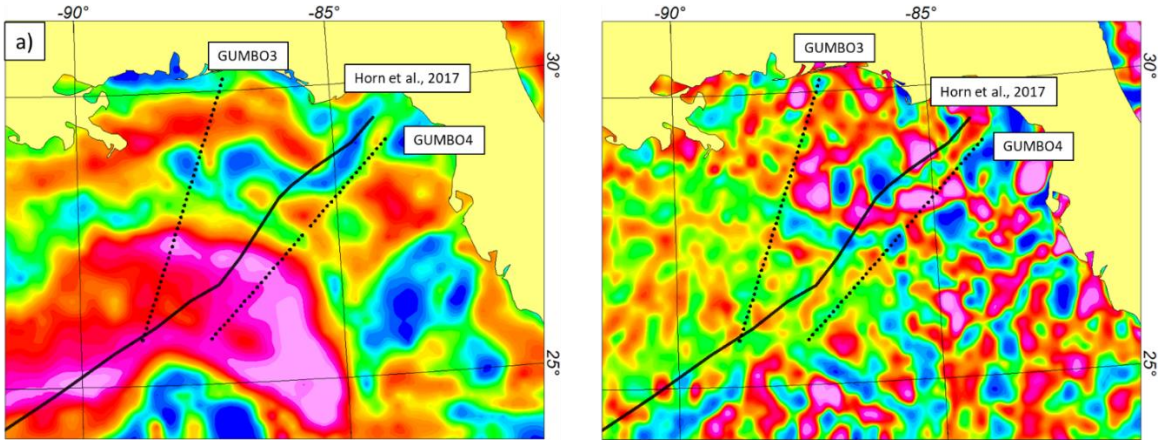

Figure 27. (a) Residual Bouguer Gravity of the northeastern Gulf of Mexico calculated for the satellite gravity data (Sandwell et al., 2014). This gravity anomaly represents the signal for all the sources between the mudline and the Moho. (b) Residual magnetic anomaly computed for the EMAG2_V3 dataset (Meyer et al., 2017). These magnetic anomalies represent the variations in magnetic susceptibilities within the crustal rocks (the sediments were assumed to be non-magnetic as their magnetic susceptibilities are several orders of magnitude lower than the igneous and metamorphic rocks).

In magnetic data, reduction to the pole was applied to un-skew the observed anomalies (see Geophysical Data section for details). The regional trend was calculated by applying an upward continuation filter with an elevation of 20 km as the magnetic field

decays much faster than the gravity field. The resultant residual magnetic anomaly is shown in Figure 27b.

Before intepreting the geological structures in the residual potential fields, a number of different filters were applied to test which one highlights them better: the first vertical derivative filter, various low and high pass filters, and the tilt derivative filter (Blakey et al., 2016). A tilt derivative of the residual Bouguer gravity map (Figure 28a) shows the lineaments better than the other tested filters; therefore, most of interpretations were based on tilt derivative transformation of the residual Bouguer gravity map. This map (Figure 28a) shows a strong pronounced high that surrounds a series of gravity lows in the center of the basin.

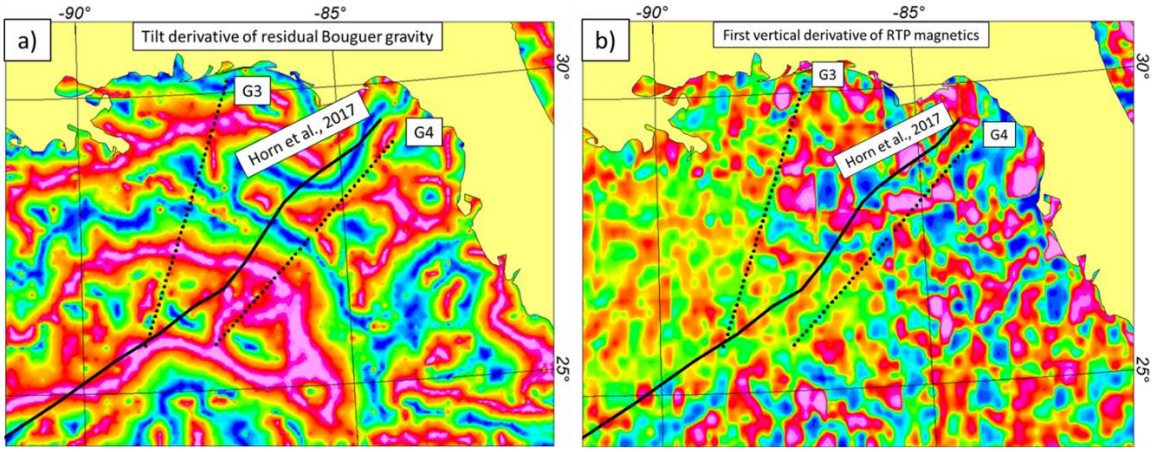

Figure 28. a) Tilt derivative of residual Bouguer gravity. b) First vertical derivative of the residual RTP magnetic map.

In magnetic data, the first derivative filter (Figure 28 b) highlights the structures better than the tilt derivative filter. The first vertical derivative of the residual RTP magnetic map shows a series of prominent magnetic highs in the center of the oceanic region that are surrounded by magnetic lows. In general, the magnetic anomalies appear to

be less pronounced than the gravity ones. However, some of magnetic high in the center of the basin correlate with gravity lows (Figure 28 a), while the surrounding magnetic lows generally coincide with the pronounced gravity high. As the anomalies are better highlighted in the filtered gravity field than in magnetic data, the spatial analysis was guided by a filtered gravity map.

4.2 Correlation with 2D subsurface models

As has been stated above, the tilt derivative of residual Bouguer gravity and the first vertical derivative of RTP magnetics show the clearest lineaments (Figure 28 a, b). The correlation of the observed lineaments with the geological structures interpreted from the three modeled profiles is illustrated in Figure 30.

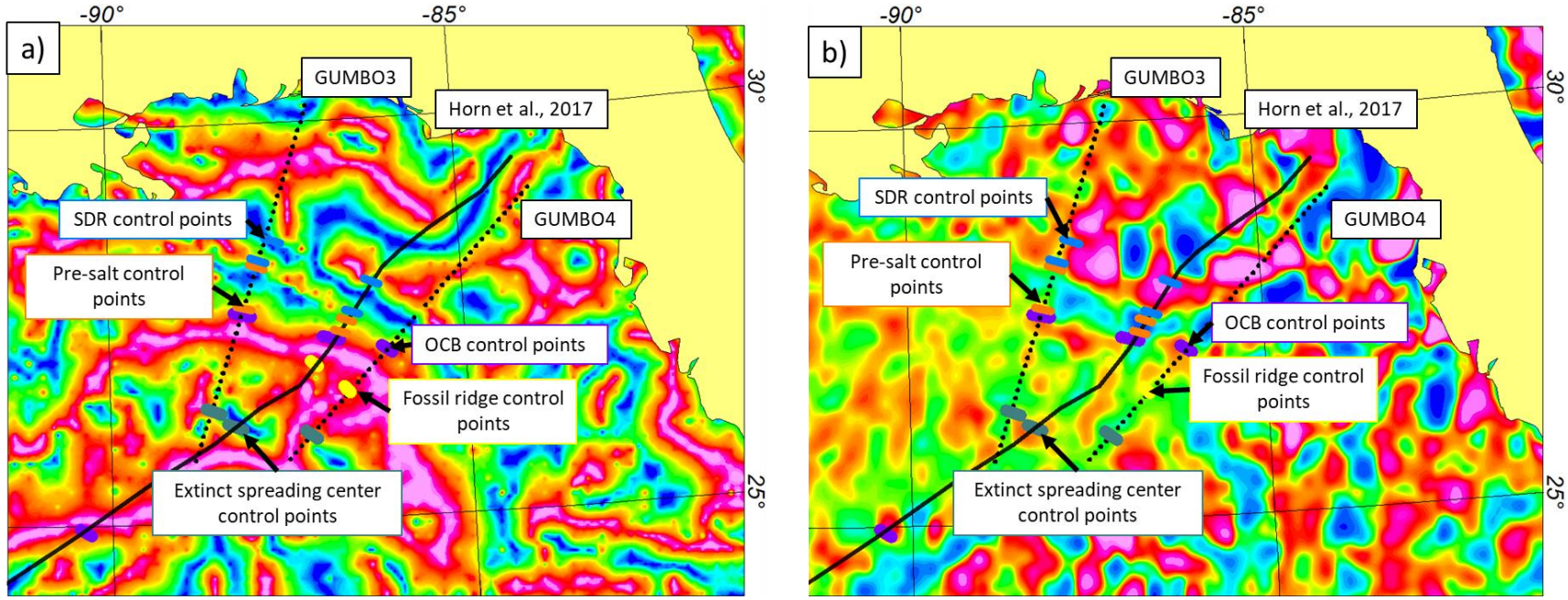

Figure 29. a) Tilt derivative filtered map of residual Bouguer Ggravity field. b) Vertical derivative filtered map of RTP magnetics. Lineaments are labeled in the maps. Blue line denotes the location of SDR. Orange line denotes pre-salt location. Purple line denotes the location of OCB. Dark green line denotes the location of young ridge. Yellow denotes the location of fossil ridge

The location of the OCB from the three models, i.e. ~310 km along Models 1A and 1B (GUMBO3), ~295 km along Model 2 (GUMBO4) and ~346 km along Model 3 (between Models 1 and 2) were marked on the tilt derivative of residual Bouguer gravity and vertical derivative RTP magnetic maps as purple lines (Figure 30). The OCB locations for all three models correspond to the same gradient in the filtered gravity (edge of a pronounced high). In magnetic data, they are consistent with linear magnetic low.

Interpreted extinct spreading centers are marked with bright yellow on the maps in Figure 29. The larger ones, correlating to gravity lows, are outlined by dark green color. The edge of the pre-salt basin from models 1 and 3 are also marked on both maps with orange color. These correlate with lows in both gravity and magnetics. The pre-salt section extends all the way to the edge of the continental domain marked by an OCB. The SDR province is marked with blue color along Models 1 and 3 as well as Model 2 (GUMBO4) does not cross either a pre-salt basin or the SDR region. All the locations from 2D subsurface models are described in the previous chapter.

4.3. Combined Interpretations of the Tectonic Structures in the Study Area

The correlation between the lineaments and interpreted geological structures allowed extension the interpretations to areas outside of seismic coverage by tracing along the gradients and lineaments in the filtered potential fields. Figure 30 shows the ocean-continent boundary, the extinct spreading centers and the extent of the pre-salt deposits mapped in the study area

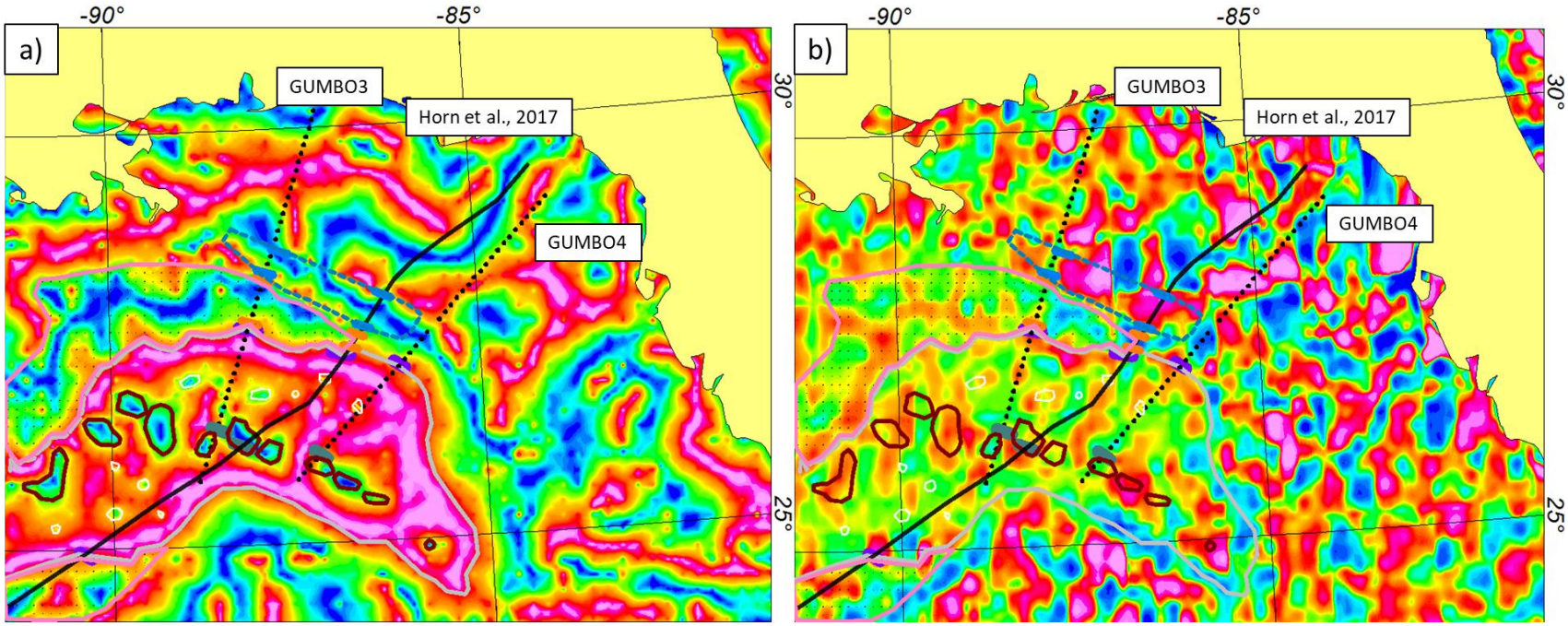

Figure 30. Mapped geological structures in the NE GoM on filtered gravity and magnetic maps. a) Tilt derivative of residual Bouguer gravity map. b) Vertical derivative of RTP magnetic map. Brown circles denote ESR. The white circles denote fossil ridges. Grey line is the OCB. Pink polygon outlines the pre-salt basin. Blue dash line indicates SDR

The OCB is characterized as a gravity high and magnetic low. A Gravity low and magnetic high refer to all segments of the fossil spreading center in the northeastern GoM. The northern edge of the SDR province corresponds to gravity low and magnetic low, while the pre-salt basin is marked by gravity low and magnetic high. The pre-salt basin wedges out to the east (as confirmed by model 2 (GUMBO4) and is bounded by an SDR province in the north and by the OCB in the south.

The pre-salt sedimentary basin is 64 km wide along Models 1A and 1B (GUMBO3) with a thickness of 3 km. The thickness is consistent with FloridaSPAN profile that images 3-4 km thick pre-salt section (Figure 15). There is only a minor amount of pre-salt basin along Model 3, with a lateral extent of 9 km and a depth of 1 km. No pre-salt was found along Model 2 (GUMBO4). Therefore, the pre-salt section wedges out to the east (Figure 30).

4.4 Validation of interpreted geological structures with the literature

Interpretations from this study have integrated seismic refraction, seismic reflection, gravity, and magnetic data compared to previous analyses. The interpreted geological structures were validated with several published seismic datasets, including the OCBs published by Bird et al. (2005); Hudec et al. (2013); Sandwell et al. (2014); Pindell and Keenan (2009); Christeson et al. (2014); Nguyen and Mann (2016) (Figure 31), the depth to basement map from 3D survey from Deighton et al. (2016) (Figure 33), and several seismic reflection profiles from Snedden et al. (2014), FloridaSPAN (2015), and Saunders et al. (2016) (Figure 33).

Figure 21 a shows defined OCBs from different studies. The OCB from this study is most close to Sandwell et al. (2014) with minor offset in the eastern side of GUMBO4 profile and southern GoM. Pindell and Keenan (2009) and Nguyen and Mann (2016) placed the OCB further north. Bird et al. (2005) placed the OCB closer to the center of the basin. Hudec et al. (2013) has a similar interpretation of the OCB where it is close to the GUMBO profiles but wider than the rest of the OCB from this study. The OCBs derived from those studies were based on only seismic interpretation or gravity method, while this study integrates both potential fields and seismic to constrain the location of the OCB.

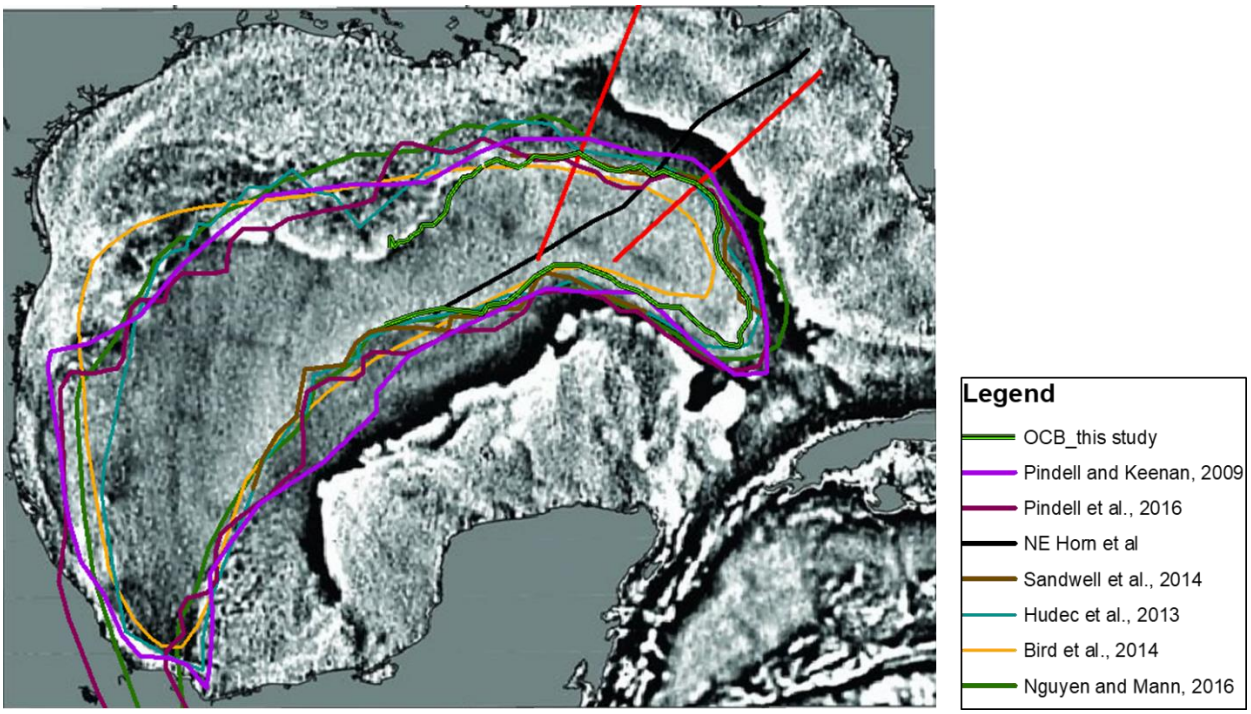

Figure 31. Comparison of different published OCBs with interpretation from this study. Three red lines are the integrated subsurface models developed in this study. The background is vertical gravity gradient from Sandwell et al., 2014.

The comparison between this study's interpreted extinct mid-ocean ridge segments generally agree with the interpretations of Sandwell et al. (2014). However, instead of three continuous spreading centers in the northeastern GoM, this study has interpreted the

spreading centers as short isolated segments from spatial analysis (Figure 32). Nguyen and Mann (2016) interpreted the spreading centers slightly offset to the south (Figure 32).

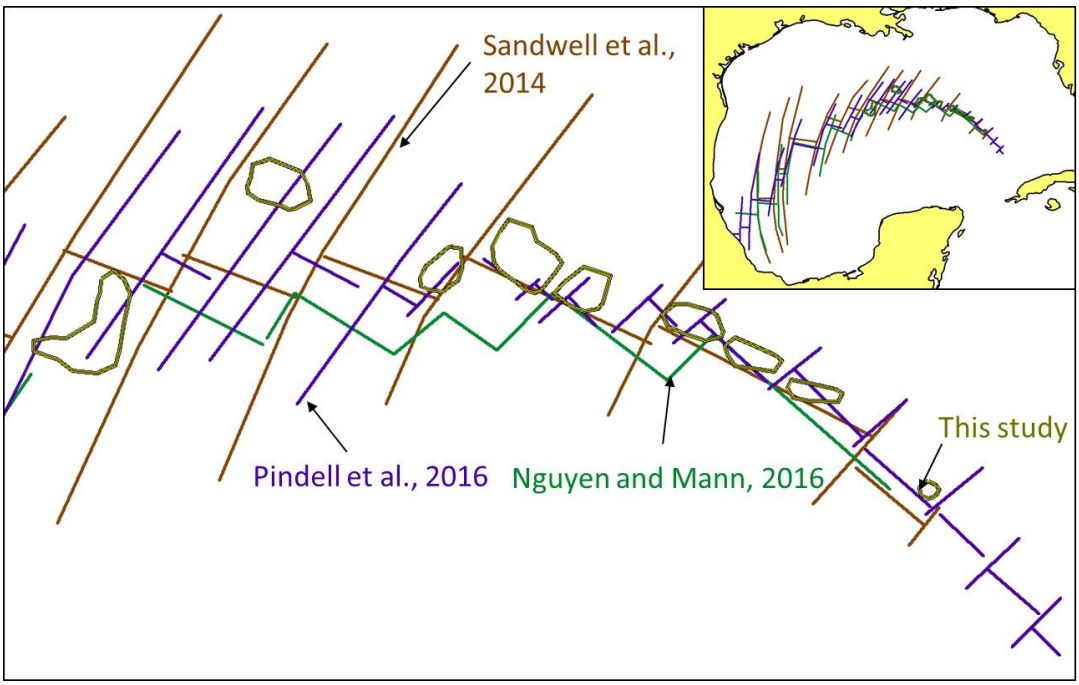

Figure 32. Comparison of different published spreading centers (Sandwell et al., 2014 and Nguyen and Mann, 2016) with this study's interpretation. The purple line is axial valley along interpreted ridge from this study.

The results of the recent 3D seismic reflection survey (Deighton et al., 2017) agrees very well with the interpretation herein of extinct spreading centers (Figure 33). The location of the 3D seismic survey is outlined in Figure 10. The background of this Figure 14 is depth to basement map from 3D seismic reflection survey. The ridges and transform faults from Deighton et al. (2017) are shown in red. The brown color is the interpretation of spreading centers from this study. The interpreted spreading centers show good correlation with mid-ocean valleys. From this 3D survey, at least three segments of mid-ocean valleys were validated as well as three transform faults (Figure 33).

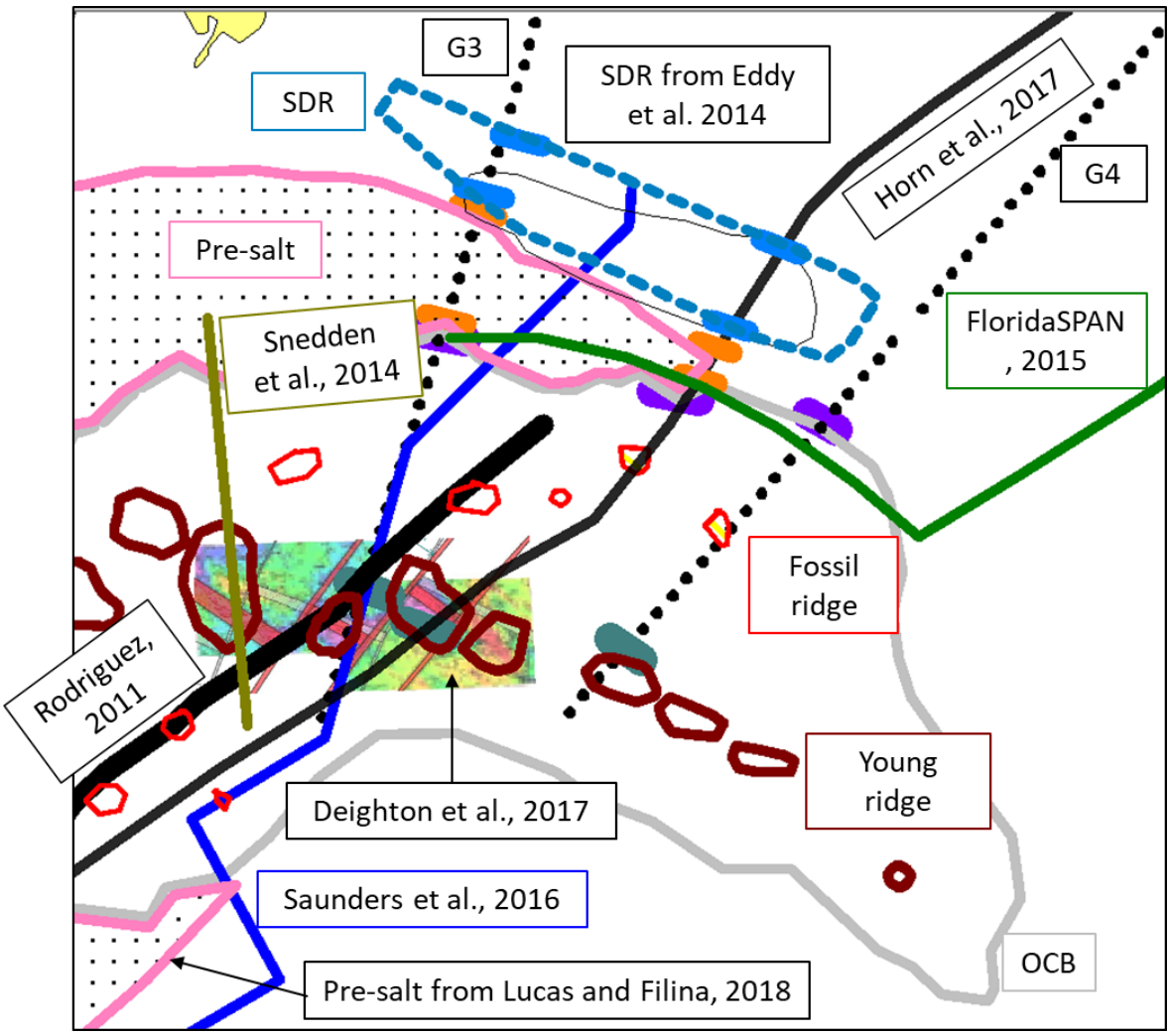

Figure 33. Comparison between TGS's map (Deighton et al., 2016) of extinct spreading centers with the ones interpreted in this study from integrated analysis of various geophysical datasets.

The interpreted SDR province is ~54 km wide and 335 km long. It is ~ 59 km longer that the one outlined by Eddy et al (2014). The NW edge of the Eddy at al. (2014) SDR province is coincident with GUMBO3 and appears to be limited by availability of seismic data. The interpretation from this study is based on the signals in filtered potential fields data (Figure 30) and the constraints from Models 1 and 3 (Figure 29). Moreover, a similar SDR province is imaged by multiple seismic reflection profiles in the southern GOM (Williams-Rojas et al., 2011, Saunders et al., 2017; O'Reily et al., 2017, Horn et al., 2017).

Similar integrated geophysical analysis performed in the southern GoM by Hartford and Filina (2018) outlined an SDR province that is 55 km wide and 360 km long. To be consistent with the interpretation on the conjugate margin, the SDR province in the study area was extended to NW of Eddy et al.'s (2014) outline.

The profile from Snedden et al. (2014) crosses the extinct spreading center. The extent of the gravity low is shown as a horizontal bar on top of the seismic image in Figure 16, thus validating the interpretation that the extinct spreading ridges are characterized as gravity lows. This profile also crosses the OCB and the pre-salt basin that are also marked in Figure 16.

Another seismic reflection profile – the one from Saunders et al. (2016), shown in Figure 11 - can be used to validate interpreted extinct spreading centers. This profile partially overlaps the line GUMBO3. The 'valley' feature (black box in Figure 11) corresponds to pronounced gravity low and magnetic high that are interpreted as an extinct spreading center.

CHAPTER 5 Discussion

5.1 Observations from this study

As a result of the potential fields modeling along three seismic lines, the densities and magnetic susceptibilities of the subsurface rocks were determined (Table 5) and the location of the key tectonic structures were constrained (Figure 30). The joint spatial analysis of gravity and magnetic fields, calibrated with three subsurface models, allowed us to determine the lateral extent and the thickness of the pre-salt sedimentary section, as well as to characterize the crustal architecture. The location of the OCB, correlated to a gravity high and magnetic low, was also determined from the integrative analysis of potential fields.

The width of the necking zone in the continental domain decreases toward to the east in the study area from 110 km for Models 1A and 1B to 99 km for Model 2 and 98 km for Model 3. The width of the necking zone may be considered as an additional constrain for tectonic reconstruction, as it should match on both margins assuming symmetric continental rifting.

The extinct spreading centers are clearly mapped in gravity data as pronounced gravity lows. The locations of the spreading centers were confirmed by seismic data (Figures 11, 14 and 16) and generally agreed with published interpretations (Sandwell et al., 2014; Figures 32 and 33). However, several new spreading centers were identified in the Models 2 and 3 (Figures 25 and 26). These new identified features are observed as small gravity lows and magnetic highs. For example, the new spreading center identified along Model 3 at distance 394 km (Figure 26) correlates to a small gravity low (Figure

30a) and magnetic high (Figure 30b). The presence of these newly identified spreading centers lead to a hypothesis about ridge propagation in the northeastern GoM – the jump of the spreading center from the old location (small newly identified features in the northern part of the oceanic domain) to the south, where the more pronounced (younger) spreading center is mapped. The older spreading center in the north produced thinner one-layer crust, while the younger one in the south is associated with thicker, two-layered oceanic crust. This hypothesis about ridge propagation, suggesting two spreading centers in the history of the GoM, is also consistent with the observed asymmetry in seafloor spreading that was noted by some authors (Hudec et al., 2013; Nguyen and Mann, 2016).

5.2 The ridge jump in literature

Ridge jump in the East Pacific Rise (EPR) is clearly seen in bathymetry data (Figure 34). The East Pacific Rise is a fast-spreading ridge with spreading rate of 7-8 centimeter per year (Rea, 1977). This fast spreading rate agrees well with the overall ridge morphology represented as axial highs (Carbontte et al., 2000). The jump of the spreading center to the west led to the formation of a microplate in between the East Pacific Rise and the Galapagos Rise. The Galapagos Rise (fossil ridge) started spreading about 17-15 Ma (Eakins and Lonsdale, 2004). Early ridge propagation to the west occurred in 15 Ma (Eakins and Lonsdale, 2004). In Miocene (~8 Ma), the East Pacific Rise began actively spreading (Rea, 1976).

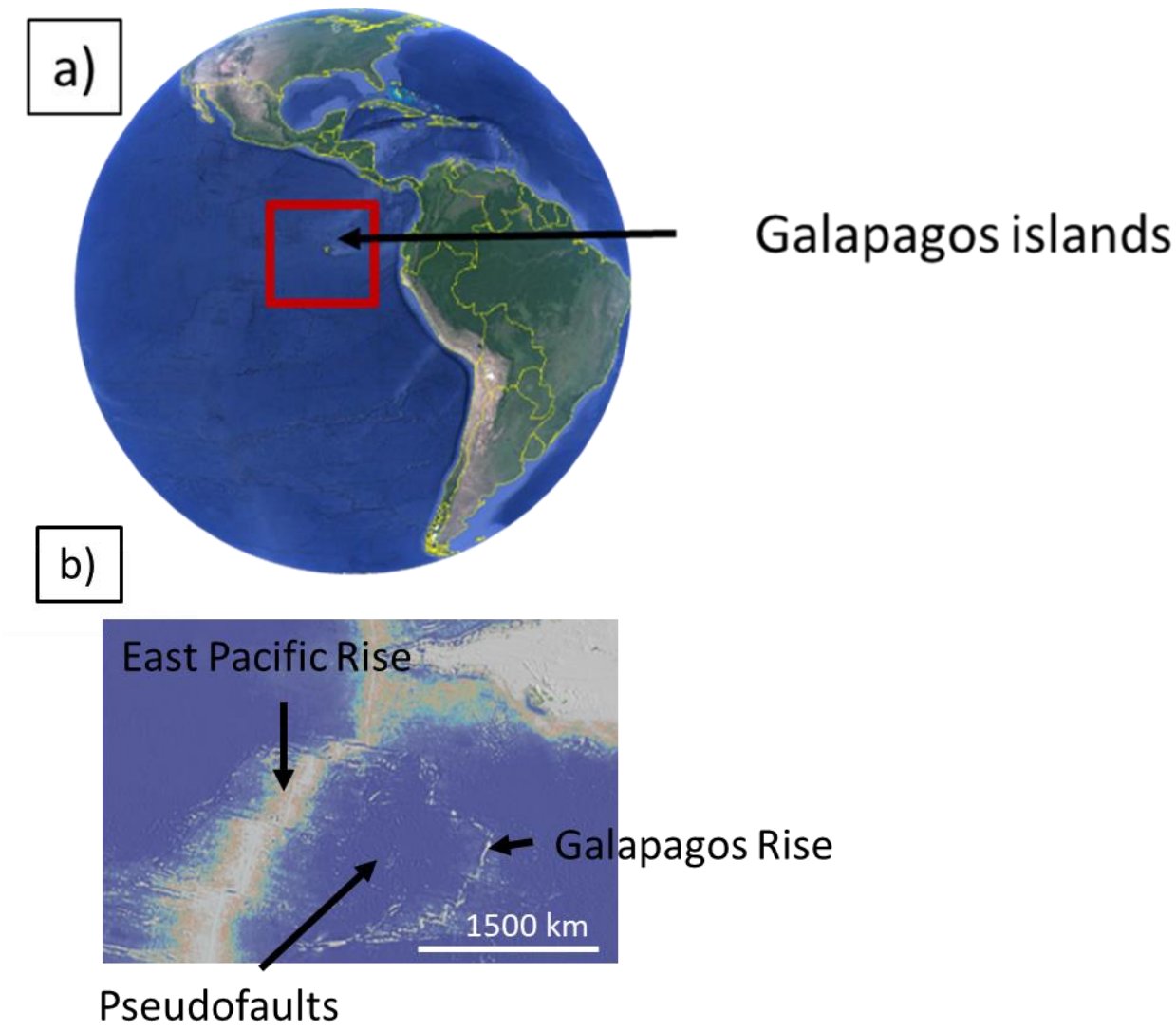

Figure 34. a) The East Pacific Rise from a global view of GoogleEarth. b) The bathymetry map of the East Pacific Rise from GeoMapApp. The ridge propagation is clearly seen with the older ridge segment on the east, and the younger one on the west.

In contrast, the GoM is believed to be a slow spreading system with an estimated spreading rate of 2.2 centimeters per year (Christeson et al., 2014). As there is an obvious difference in the spreading rates between GoM and EPR, the fast spreading EPR cannot be considered as a proper analog for the slow-spreading GOM. However, due to pronounced

structural ridges, the EPR bathymetry shows the overall geometry and organization of the propagation ridge very clearly, so it has been used in this study to illustrate the concept.

The crust in the center of the GoM is covered with over 8 km thick layer of sediments, so bathymetry data does not show the spreading centers, moreover any ridge propagation structures. Thus, the filtered gravity data were used to map the extinct spreading centers (Figure 28a). In order to test the hypotheses that gravity data may be used to map the ridge propagation, the gravity data over the East Pacific Rise were also filtered. The same mathematic transformations were applied to the Free-Air gravity over the East Pacific Rise, downloaded from Sandwell et al. (2014), with two exceptions. The upward continuation to an elevation of 15 km was applied to compute the regional trend (in contrast to 40 km for GOM) as the Moho is at a shallower depth over the EPR compared to the GoM. Then the residual gravity field over the East Pacific Rise was additionally continued upward to an elevation of 8 km to mimic the presence of the thick sedimentary layer in order to compare with the GoM.

Filtered gravity map of the EPR was rotated 90 degrees (Figure 35a, b) with the intention of having a better structural alignment with the features in the GoM (Figure 35c). The resultant Figure 35b shows both old and young ridges over the EPR as noticeable gravity lows. The young spreading segments appear to be larger and more pronounced than the old ones. The filtered gravity over the GoM appears to have a similar pattern of gravity anomalies, overall suggesting ridge reorganization.

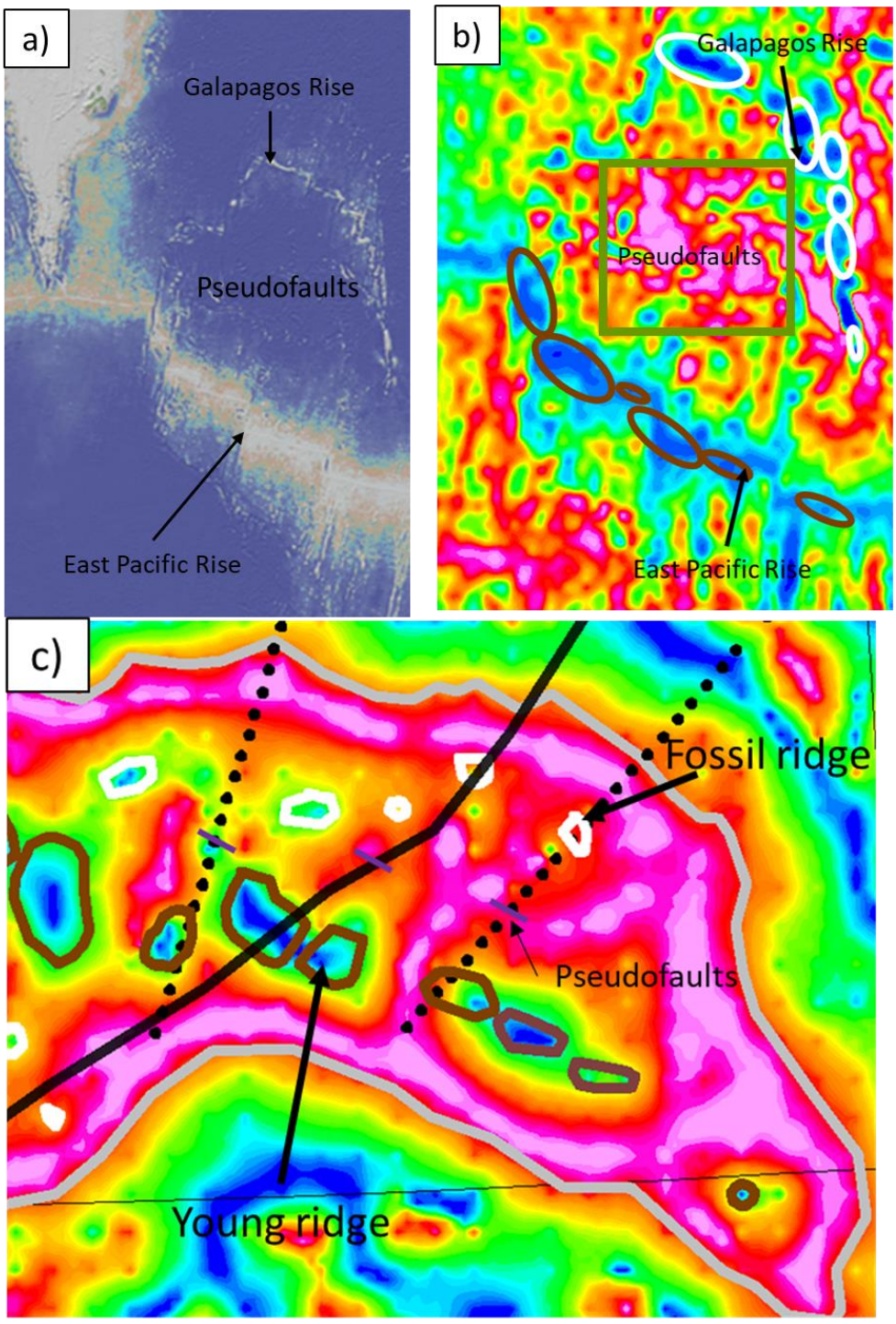

Figure 35. a) Bathymetry of the EPR rotated 90 degree counterclockwise in order to better illustrate the correlation of the propagating ridge segments with the ones in the GoM. b) Tilt derivative of residual Bouguer of the East Pacific Rise also rotated 90 degrees. Brown color outlines an active spreading ridge. White color outlines a fossil ridge. Green box shows pseudofaults – the boundary between old and new oceanic crustal domains, c) Tilt derivative of residual Bouguer of the GoM. Brown color indicates the younger spreading ridge. White color outlines fossil ridge. Pseudofaults are marked as purple lines.

Migration of the spreading ridge creates a wake of pseudofaults that are oblique to the ridge axis and point in the direction of offset migration (Kleinrock et al., 1997; Figure 36a). Pseudofaults form a V-shaped wake behind the propagating spreading ridge pointing in the direction of propagation, marking previous locations of the propagator tip (Screejith et al., 2016; Figure 36b). The V shape pseudofaults in the East Pacific Rise are observed from the Google Earth image (outlined with a green box in Figure 36a). In the filtered gravity map (Figure 35 b), the pseudofaults are characterized by gravity highs in the East Pacific Rise. The pseudofaults are associated with a vertical trough in the basement according to an integrative analysis of basement characteristics and gravity data from Screejith et al., 2016.

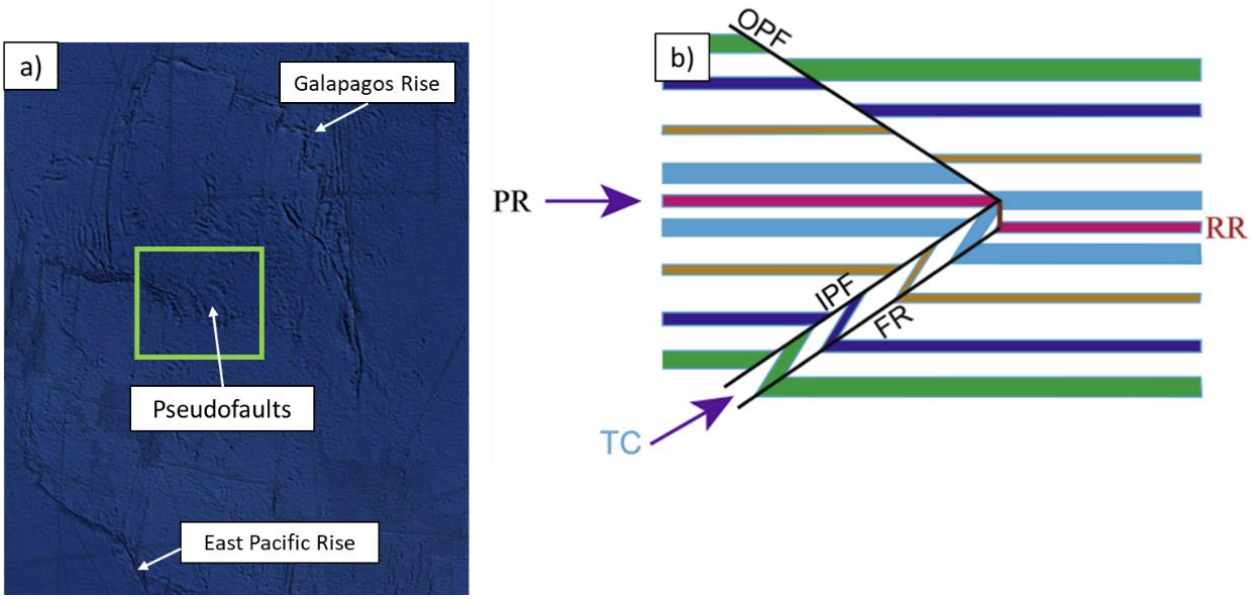

Figure 36. a) V shape pseudofaults in the East Pacific Rise from Google Earth. This picture has been rotated 90 degrees in order to corresponds to Figure 35 a. The pseudofaults are outlined by green box. b) The mechanisms of forming the V shape pseudofault (modified from Screejith et al., 2016). PR-Propagating Ridge. RR- Receding Ridge. TC-Transferred Crust. IPF-Inner Pseudofault. OPF-Outer Pseudofault. FR- Failed Ridge.

5.3 Propagating ridge in the GoM

The subsurface models developed for this study (Figures 23, 24, 25 and 26) mapped three locations that mark a change in the oceanic crustal structures, i.e. the location of pseudofaults (Figure 35c). Two of the locations along Model 2 and 3 correlate to pronounced gravity highs in the filtered gravity map. The one from Models 1A and 1B is characterized as a gravity low. This is because the location of that pseduofault appears to be overprinted with the transform fault mapped by Deighton et al. (2017) as troughs in the basement (Figure 14). Furthermore, this location along GUMBO3 was checked with 2D seismic reflection data, which suggests a valley (white box in Figure 11). This is consistent with observation from Deighton et al. (2017) that transform faults and extinct spreading centers are both characterized as axial valleys in the western GoM. Therefore, the superposition of these two structures - pseudofault (the contact zone between two distinct crustal domains) and the younger transform fault – complicates the interpretation of the gravity anomaly. By analogy with the pseudofaults observed over the EPR (Figure 35b), these three spots are interpreted to mark the pseudofault or a boundary between the old and new oceanic crustal segments.

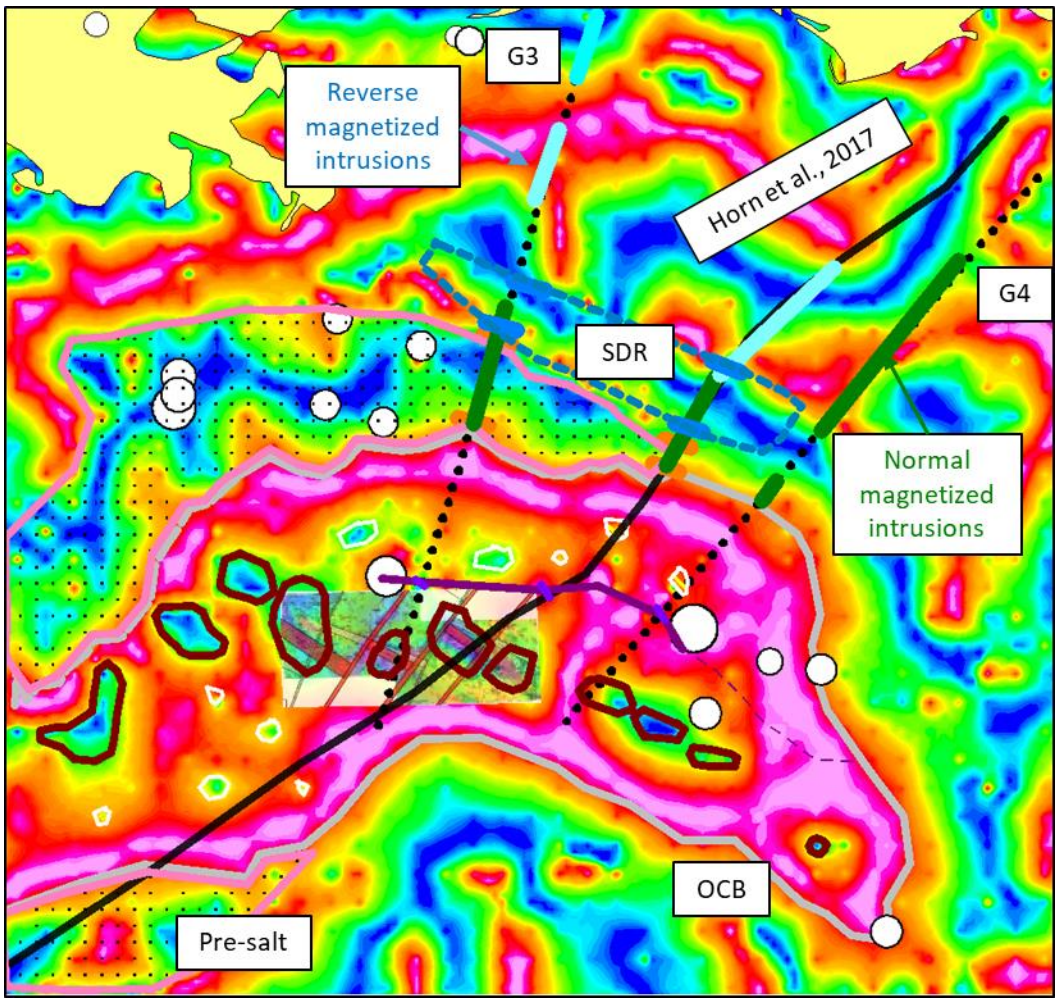

Figure 37. The location of a pseudofault in the northeastern GoM on the tilt derivative of residual Bouguer gravity map. The 3D seismic data interpretation from Deighton et al., 2017 is superimposed on the gravity map. The red transform fault close to GUMBO3 terminates at the pseudofault. The light purple marks show the points of contact between two distinct crustal domains from three modeled profiles. These correlate to gravity highs. The dark purple line shows the interpreted boundary between the old oceanic domain in the north and the young one in the south. Brown outlines denote the young spreading centers, while the white ones show the old spreading centers that identified from this study. Grey line shows the OCB interpreted in this study. The bright blue lines in the continental region overlap three models indicate the location of negatively polarized intrusion. The green lines overlap three models in the continental region indicate the location of positively polarized intrusion. The white dots are earthquakes from USGS Earthquake Catalog.

According to Reid and Jackson (1981), there is a positive correlation between oceanic crustal thickness and spreading rate. Slow spreading results in a thinner oceanic crust, while a fast-spreading forms the thicker crust. The example of the modern slow

spreading ridges is the Mid-Atlantic Ridge with the crust varying in thickness from 2 to 7 km at the Kane fracture zone (Chen, 1992). The fast-spreading systems result in a thicker crust, like the East Pacific Rise (5-8 km from Chen, 1992). Therefore, the thinner oceanic crust in the GoM (along the Model 2) appears to be produced by a slower spreading center than the thicker one from Models 1A and 1B. The thin and dense oceanic crust with fast seismic velocity (Vp ~7.0 km/s) and high magnetic susceptibility, presumably composed of gabbro, is most likely produced by ultraslow spreading. This crust was interpreted immediately to the south of the OCB in the Model 1B (Figure 24) and in the Model 2 (Figure 25); this segment was also modeled twice in the Model 3 (Figure 26) adjacent to both continental domains. In contrast, the thicker, two-layered crust suggests a faster spreading rate associated with a higher magma supply. However, the fact that the younger extinct spreading centers are imaged in seismic reflection data as valleys, rather than ridges, suggesting that the thicker, two-layered crust was still produced by a relatively slow spreading ridge (Figures 11, 14 and 16).

According to Snedden et al. (2014), the age of the oceanic crust may be constrained from the age of the oldest sediments overlying the crust tied to several onshore wells (Figure 39). That study concluded that the oldest oceanic crust in the northeastern GoM is 155 -160 Ma old and that oceanic crust ceased before 137 Ma ago. The pseudofaults location that derived from this study is align with the 150 Ma contour line in Figure 39. Thus, by measuring the width of the oceanic segments on each side of the pseudofault and using the age from Snedden et al. (2014), the spreading rate of each spreading event may be estimated. The oceanic segment associated with fossil ridge is 96 km wide on average, and the estimated spreading rate was 9 mm/yr (full spreading rate) by assuming the first

spreading episode lasted 10 Ma. The young crust zone is 146 km wide on average and the estimated spreading rate was 1.1 mm/yr by assuming the second spreading episode lasted 13 Ma.

The initial spreading rate for the oldest segment is consistent with an ultra-slow spreading. The younger spreading agrees with the slow spreading centers imaged in seismic data as valleys (Saunders et al., 2016, Figures 11). The faster spreading rate for the younger ridge with respect to the fossil ridge is consistent with the generally thicker crust and the presence of basaltic layer on top of the oceanic layer 3 (gabbro).

Before 150 Ma when the ridge reorganization occurred and the young ridge started spreading, the segments of the old ridge were aligned. Figure 38 shows the total extent of the oceanic crust produced by the first seafloor spreading event in the GoM.

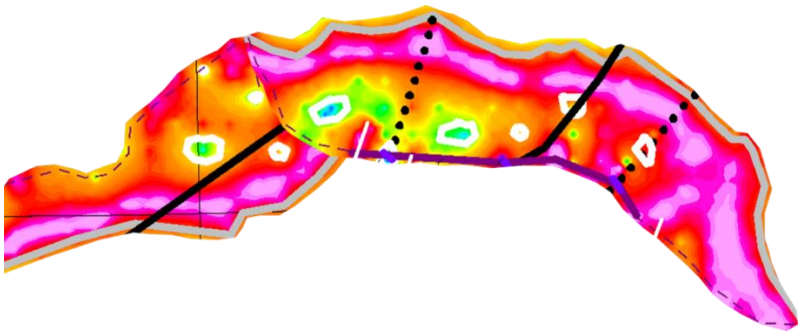

Figure 38. The distribution of old oceanic crust produced by a fossil ridge before the young ridge started spreading. The thick purple line indicates the boundary between the young crust and old oceanic crust in the northeastern GoM. The dashed purple line is extrapolated by tracing similar gravity signals (highs). White circles indicate the old extinct spreading centers.

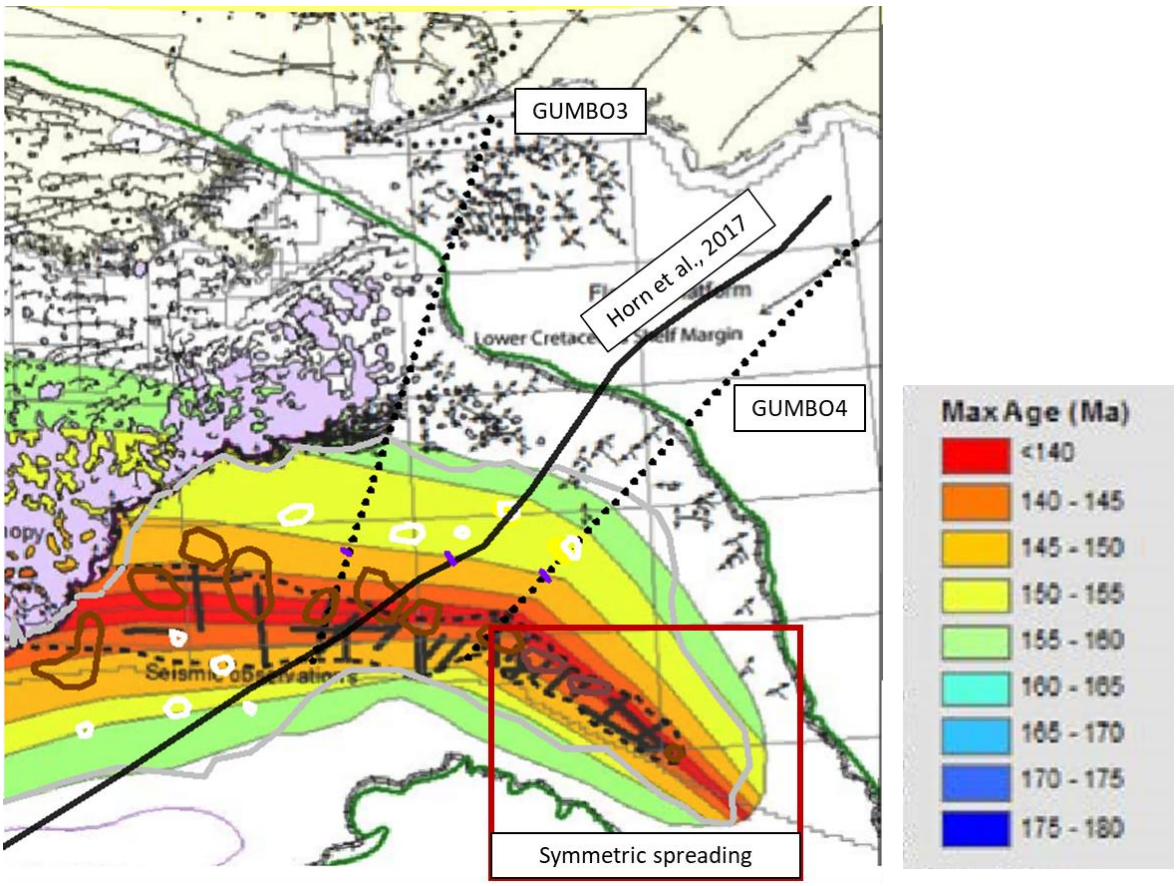

Figure 39. Plate tectonic reconstruction for the eastern GoM modified from Snedden et al., 2014. Different colors in the background indicate different ages of the crust. The solid black lines in the center are the proposed spreading centers from Snedden et al., 2014. The purple marks that overlap with age of 150 Ma indicate the boundary between old spreading event (brown outlines) and young spreading event (white outlines). Grey line indicates the OCB from this study.

This study infers that at 150 Ma (age from Snedden et al. 2014, Figure 39), a presumable change in tectonic stresses occurred leading to a change in the Euler pole. This resulted in a consequent ridge propagation to the south in the eastern GoM. At the same time, the ridge propagated to the north in the central GoM (Figure 38). The oceanic crust in the easternmost part was not spreading before 150 Ma (Figure 40). Thus, the easternmost part of oceanic domain is characterized by a symmetrical spreading. In contrast, the oceanic crust to the west appears asymmetric due to ridge propagation.

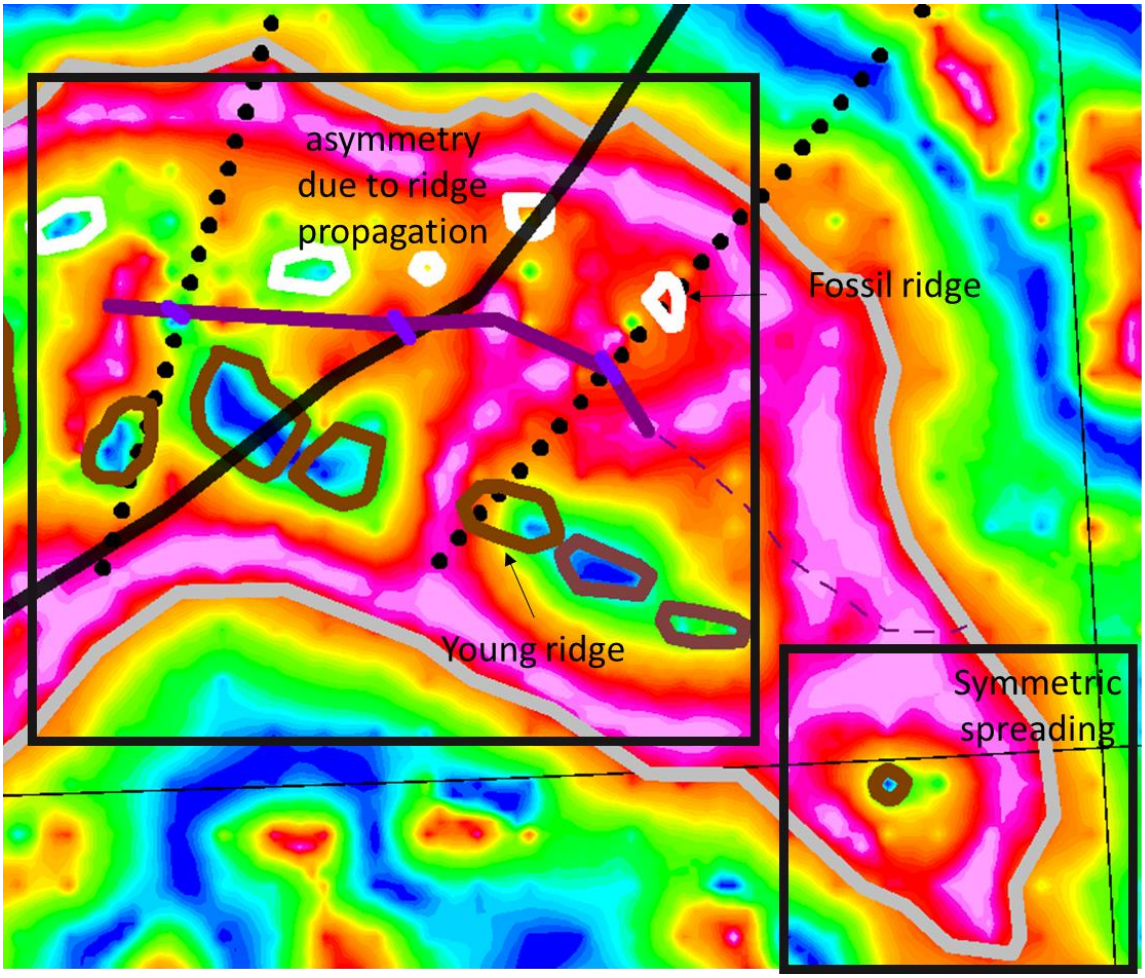

Figure 40. The formation of oceanic crust in the northeastern GoM. The crust in the center of the study area shows the evidence of ridge propagation to the south, presumably at 150 Ma (Snedden et al., 2014). Brown circles are young extinct spreading centers. White circles are fossil spreading centers. The crust in the easternmost part of the study area is symmetric as it initiated after ridge propagation at 150 Ma.

The younger crustal segments are thicker and have basaltic layer on the top, which was determined from the derived physical properties, namely Vp ranging from 5 to 6.5 km/s, and modeled density of 2.65 g/cc (Carlson and Herrick, 1990). This suggests an increase in magma supply from older to younger spreading events.

The interpreted ridge jump in the GoM is consistent with the finding of Pindell et al. (2016), who determined the change in the rotation pole between 152 and 145 Ma to the southeast. Figure 41 shows the boundary between different crusts (early oceanic crust and late oceanic crust) that was proposed by Pindell et al. (2016) aligns well with the pseudofaults interpreted in this study.

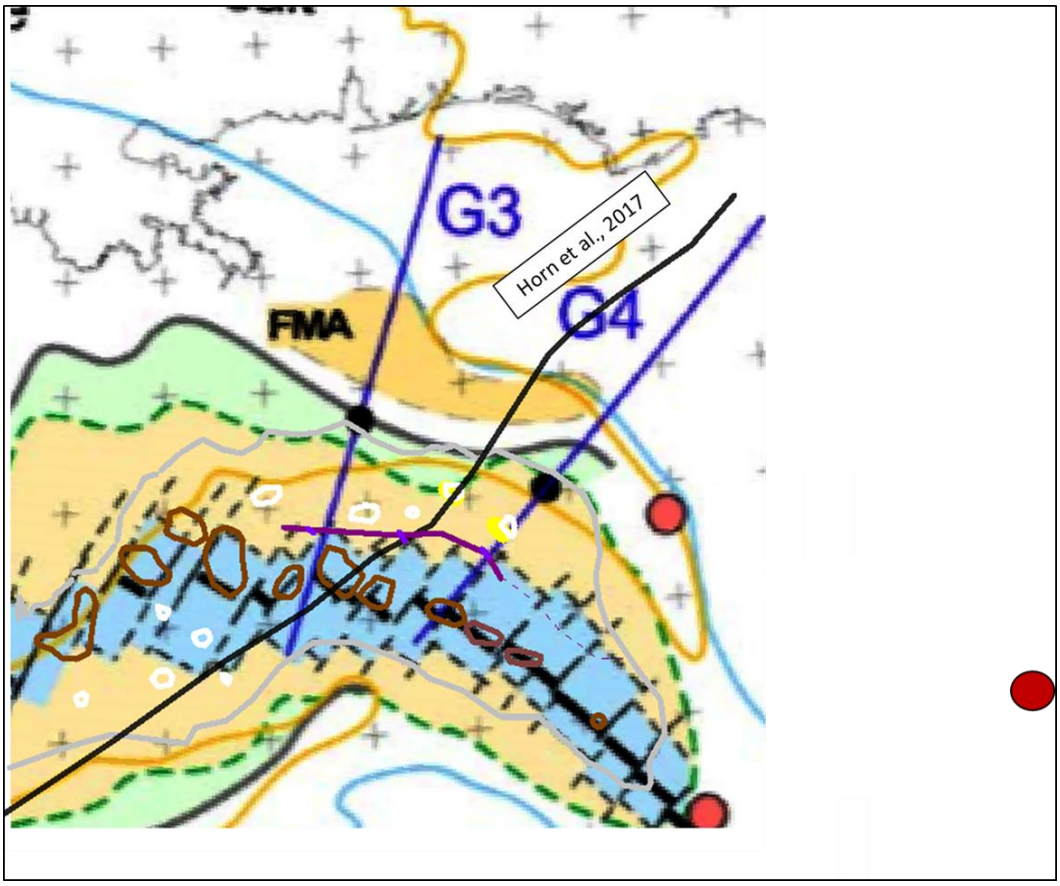

Figure 41. Map of four primary basement types modified from Pindell et al. (2016) with a pseudofault zone from this study superimposed (thick purple line). The green crust is hyper-extended crust/exhumed mantle interpreted by Pindell et al. (2016). The yellow crust is earlier oceanic crust (Oxfordian-Tithonian, 159-150 MA). The blue crust is later ocean crust (Tithonian-Top Berriasian, 150-139 MA). White crust is rifted continental margins in the GoM. See caption details in Figure 39. The red dot in the center is proposed pole1 from Pindell et al. (2016). The red dot at the bottom of the map is the proposed finite pole for the Yucatán restored from today's position to the Bathonian position from Pindell et al. (2016). The green dashes line is the ocean-continent boundary from Pindell et al. (2016).

However, the OCB between this study and Pindell et al. (2016) shows some dramatic discrepancies (Figure 41). The wider OCB from Pindell et al. (2016) resulted from assumed rifting symmetry that is forced in the model shown in Figure 41. Moreover, the exhumed mantle, suggested by Pindell et al. (2016), is not supported by this study. According to Pindell et al., 2016 (Figure 41), the reconstruction of the basin lead to changes of the Euler Pole three times. This study confirms at least one evidence of the change in the location of the Euler pole that is related to the ridge propagation, presumably at 150 Ma, that would relate to Pindell et al.'s jump from Pole 2 (159-150 Ma) to Pole 3 (150-139 Ma).

Furthermore, the pseudofault boundary derived in this study is aligned with the locations of several crustal earthquakes (Figure 37) that were described in Chapter 2. The earthquakes focal depth is over 14 km, suggesting they are lithospheric events. However, they were not aligned with any known tectonic structures. According to this study, they occurred in a zone of weakness between two distinct crustal domains due to two spreading episodes. This zone appears to be reactivated with the current compressional stress (identified from two identical focal mechanisms; Chapter 2). Therefore, the location of pseudofault is confirmed with the observed seismicity in the study area.

This study concludes that the oceanic crust in the GoM formed in two stages. The first spreading episode started ~155 to 160 Ma (Snedden et al., 2014) and resulted in thin, dense, and highly magnetic oceanic crust with a uniform seismic velocity profile (Vp ~7 km/s). The younger crust shows much thicker, two-layer structure (basaltic layer overlays gabbroic layer) suggesting an increase in the supply of magmatic material.

Two models were developed along the GUMBO3 as described in Chapter 3 (Figures 23 and 24). The difference between them is the Moho depth in the oceanic region

near the OCB. Model 1A assumes thicker oceanic crust consistent with seismic refraction data (Figure 5). Model 1B was based on reflection data (Figure 8), suggesting a 2 km thinner crust. Geophysical modeling along Models 1A and 1B did not allow to distinguish between them. However, Model 1B is more consistent with the ridge reorganization conclusion as it supports thinner crust associated with fossil ridge. Thus, the integration of geophysical modeling with tectonic analysis led to Model 1B being preferable than Model 1A.

The timing of ridge propagation (150 Ma) concluded from this study is coincident with a ridge reorganization suggested by Bird et al. (2007) in the Central Atlantic Ocean. According to Bird et al. (2007), this major reorganization between 164 Ma and 159 Ma can be related to plate interactions as North America separated from Gondwana. This is consistent with the conclusion from Van Avendonk et al. (2011), suggesting a ridge reorganization in the mid-Atlantic ocean at 153 Ma in order to explain the asymmetric spreading based on analysis of magnetic anomalies.

CHAPTER 6. Conclusion

The major conclusions from this research are:

1) Three integrated geophysical models were developed in the eastern Gulf of Mexico revealing a volcanic nature of the margin. A series of magmatic intrusions in continental crust were identified during the modeling that are necessary to explain the high magnetic anomalies. Some of the intrusions are coincident with zones of fast seismic velocities in the lower crust, while the others are located in the middle of the crust. Some of the intrusive bodies require reverse magnetic polarity.

2) This study utilizes multiple geophysical and geological datasets from the public domains (seismic, potential fields and well data) in order to map the tectonic structures in the northeastern GoM. The location of the ocean-continent boundary was derived from spatial analysis of both potential fields, calibrated with three subsurface models. The ocean-continent boundary is associated with gravity high and magnetic low in the filtered potential fields maps.

3) Pre-salt deposits accumulated in the northeastern GoM. Based on the subsurface models, the pre-salt basin is 64 km wide in the western part of the margin (along Model 1) and pinches out toward to east (absent along Model 2).

4) An SDR province is modeled along Models 1 and 3. The SDR province is absent along Model 2. The SDRs are aligned with the northern edge of the pre-salt basin. The average width of SDR province is 54 km, and the length is 335 km.

5) Extinct spreading centers correlate to topographic depressions (valleys) imaged in 2D and 3D seismic reflection data, suggesting a slow spreading rate. In potential field data, all

of them are associated with gravity lows; however, not all of them are related to magnetic highs in filtered maps. The relationship between magnetic data and extinct spreading centers is not well defined, presumably due to the low quality of magnetic data.

6) The ridge propagation occurred at 150 Ma (age from Snedden et al., 2014) due to change in tectonic stresses leading to a jump in Euler pole. The fossil ridge in the north produced a thinner crust with an ultraslow spreading rate of 0.9 cm/yr (full spreading rate). The younger ridge produced a thicker crust with standard oceanic structure (basaltic layer on top of the gabbroic one). The increase in magmatic material supply occurred at the time of ridge reorganization, leading to thicker than the normal oceanic crust. However, the estimated full spreading rate for the younger ridge is 1.1 cm/yr, which is characterized as slow spreading as well and is consistent with the mid-ocean valleys (not ridges) imaged in seismic reflection data.

7) The boundary between two distinct oceanic crusts (thin crust associated with fossil ridge and thick crust associated with young ridge), i.e., a pseudofault, corresponds to gravity high in filtered residual Bouguer gravity. It is well aligned with the strikes of several crustal earthquakes recorded in GoM, suggesting that the pseudofault represents a zone of weakness currently being reactivated.

8) The ridge propagation history in the northeastern GoM concluded by this study based on integrative analysis of seismic, gravity, magnetics, and well data provides a novel way to reconstruct the eastern Gulf of Mexico. The ridge propagation explains the presence of two distinct crustal zones in the oceanic domain, the observed asymmetry of the oceanic crust, and observed seismicity in the northeastern GoM.

Reference

Arbouille, D., Andrus,V., Piperi, T., and Xu, T., 2013, Sub-salt and Pre-salt Plays-How Much Are Left To Be Discovered, adapted from presentation at AAPG http://www.searchanddiscovery.com/pdfz/documents/2013/10545arbouille/ndx_arbouille.pdf.html.

Bankey et al., 2002, Digital data grids for the magnetic anomaly map of North America, USGS Open-File Report 02-414.

Bartok, P., 1993, Prebreakup Geology of the Gulf of Mexico-Caribbean: Its Relation to Triassic and Jurassic Rift Systems of the Region, Tectonics, Vol. 12, No. 2, p.441-459.

Bird, D. E., Burke, K., Hall, S.A., and Casey J. F., 2002, Gulf of Mexico tectonic history: Hotspot tracks, crustal boundaries, and early salt distribution, AAPG Bulletin, Vol. 89, No. 3, p. 311-328.

Bird, D. E., Hall, S.A., Burke, K., Casey, J.F., and Sawyer, D.S., 2007, Early Central Altantic Ocean seafloor spreading history, Geosphere, Vol. 3, No. 5, p. 282-298, doi: 10.1130/GES00047.1.

Blakely, R. J., Connard, G. G., Curto, J. B., 2016, Tilt Derivative Made Easy, http://www.geosoft.com/media/uploads/resources/tilt_derivative_made_easy_07-2016.pdf.

Buffler, R., and Sawyer, D., 1985, Distribution of crust and early history, Gulf of Mexico basin: Gulf Coast Association of Geological Societies Transactions 35, p. 333-344.

Bureau of Ocean Energy Management website, 2018, https://www.boem.gov/.

Carbotte, S. M., Solomon, A., and Ponce-Correa, G., 2000, Evaluation of morphological indicators of magma supply and segmentation from a seismic reflection study of the East Pacific Rise 15° 30´-17° N, Journal of Geophysical Research, V. 105, No. B2, p. 2737-2759.

Carlson, R. L. and Herrick, C. N, 1990, Densities and porosities in the oceanic crust and their variations with depth and age, Journal of Geophysical Researches, V. 95 (B6), p. 9153-9170.

Chen, Y. J., 1992, Oceanic Crustal Thickness Versus Spreading Rate, Geophysical Research Letter, Vol. 19, No. 8, p. 753-756.

Christeson, G. L., Van Avendonk, H. J. A., Norton, I. O., Snedden, J. W. , Eddy, D. R. , Karner, G. G., and Johnson, C. A., 2014, Deep crustal structure in the eastern Gulf of Mexico, *Journal of Geophysical Research: Solid Earth*, Vol.119, p. 6782-6801.

Clark, D.A. and Emerson, D.W., 1991, Note on rock magnetization characteristics in applied geophysical studies, Exploration Geophysics, Doi: 10.1071/EG991547.

Diaz, D. C., 2018, New Hydrocarbon Prospectively in Brazil, Geoexpro, V. 14, No. 6.

Duncan, M. H., 2013, The northeastern Gulf of Mexico: Volcanic or Passive MarginSeismic Implication of the Gulf of Mexico Basin Opening Project, [MS thesis]: The University of Texas at Austin.

DSDP Volume LXXVII, doi:10.2973/dsdp.proc.77.1984.

Deighton, I. C., Winter, F., and Chisari, D., 2017, Recent High Resolution Seismic, Magnetic and Gravity Data Throws New Light on the Early Development of the Gulf of Mexico, AAPG, oral presentation.

Eakins, B. W. and Lonsdale, P. F., 2004, Structural patterns and tectonic history of the Bauer microplate, Eastern Tropical Pacific, Marine Geophysical Researches, DOI 10.1007/s11001-004-5882-4, p. 171-205.

Eddy, D. R.,Van Avendonk, H. J. A, Christeson, G. L., Norton, I. O., Karner, G. D. Johnson, C. A. and Snedden, J. W., 2014, Deep crustal structure of the northeastern Gulf of Mexico: Implications for rift evolution and seafloor spreading, *Journal of Geophysical Research: Solid Earth Vol.* 119, p. 6802-6822.

Eddy, D.R., 2014, Mesozoic rifting along the eastern seaboard of North America: insights from the seismic velocity structure of the Newfoundland margin and the northern Gulf of Mexico, [Ph.D. dissertation], The University of Texas at Austin.

Erlingsen, E., 2017, US Back as Largest GoM Producer, Geoexpro, Vol. 14, No. 1.

Filina, I., Delebo, N., Mohapatra, G., Coble, C., Harris, G., Layman, J., Stickler, M., and Blangy, J., 2015, Integration of seismic and gravity data-A case study from the western Gulf of Mexico, Interpretation.

Filina, I., 2017, Crustal distribution in the central Gulf of Mexico from an integrated geophysical analysis, SEG.

Fisher, W. and McGowen, J., 1967, Depositional systems in Wilcox Group (Eocene) of Texas and their relation to occurrence of oil and gas, AAPG Bulletin. Available at: http://archives.datapages.com/data/doi/10.1306/5D25C591-16C1-11D78645000102C1865D.

Galloway, W. E., 2008, Depositional evolution of the Gulf of Mexico sedimentary basin, in Sedimentary Basins of the World, edited by A. Miall, p. 505-549.

Galloway, W. E., 2009, Gulf of Mexico, GEO ExPro, Vol. 6, No. 3.

Godinez-Urban, A., Lawton, T.F. , Garza, R.S. M. , Iriondo, A. I. , Weber, B. , and L-Martinez, M. , 2011, Jurassic volcanic and sedimentary rocks of the La Silla and Todos Santos Formations, Chiapas: Record of Nazas arc magmatism and rift-basin formation prior to opening of the Gulf of Mexico, Geosphere, V. 7, No. 1, p. 121-144.

Godo, T., 2017, The Appomattox field: Norphlet Aeolian sand dune reservoirs in the deep-water Gulf of Mexico. In: Merrill, R. K., Sternbach, C. A. (Eds.), Giant fields of the decade 2000-2010. AAPG Memoir 113, p. 29-54.

Goswami A., Pindell, E. H. J., and Horn, B.W., 2017, Pre-salt in the deepwater Gulf of Mexico: Evolution and play potential in the syn-rift and sag fill in offshore Mexico, AAPG Annual Convention and Exhibition, Houston, Texas.

Hall, D.J., 1990, Gulf Coast-East Coast magnetic anomaly I: Root of the main crustal decollement for the Appalachian-Ouachita orogeny, Geology, Vol. 18, p. 862-865.

Hartford, L. and Irina, F., 2018, Geophysical Analyses of Southern Gulf of Mexico, AAPG Annual Convention and Exhibition, Salt Lake City, Utah.

Henry, D., 2017, Offhsore drilling oppoenets gear up for Gulf fight, The hill, http://thehill.com/policy/energy-environment/332141-offshore-drilling-opponents-gear-up-for-gulf-fight.

Hiltermann, F., Rock property framework for comprehending deep-water seismic response: Presented at the 14th Annual Gulf Coast Technical Meeting, SEG

Horn, B. W., Hartwig, A. , Faw, J. , Novianti, I. , Goswami, A. , and McGrail, A. , 2017, Refining Exploration Opportunities in Mexico, Geoexpro, Vol. 14, No. 1.

Hudec, M. R., Jackson, M. P. A., and Peel, F. J., 2013, Influence of deep Louann structure on the evolution of the northern Gulf of Mexico, *AAPG Bulletin*, Vol. 97, No. 10, p. 1711-1735.

International Chronostratigraphic Chart, v 2016/12: www. Stratigraphy.org (accessed July 2018)

Kleinrock, M.C., Tucholke, B.E., Lin, J., Tivey, M.A., 1997, Fast rift propagation at a slow-spreading ridge, Geology, v. 25, no. 7, p. 639-642.

Kneller, E. A., and Johnson, C. A., 2011, Plate kinematics of the Gulf of Mexico based on integrated observations from the Central and South Atlantic, Trans. Gulf Coast Assoc. Geol. Soc., 35, p. 283–299.

Koning, T., 2014, Angola, West Africa: Oil & Gas Production from Pre-Salt Carbonates to Post-Salt Clastics, from Onshore to Deep Offshore, GeoConvention: Focus.

Lundin, E. R., 2017, The Gulf of Mexico and Canada Basin: Genetic Siblings on Either Side of North America, GSA Today, Vol.27, No. 1.

Marjanovix, M.S., Carbontte, M., Nedimovix, M.R., Canales, J.P., 2011, Gravity and seismic study of crustal structure along the Juan de Fuca Ridge axis and across pseudofaults on the ridge flanks, Geophys.Geochem. Geosyst. V. 12 N. 5.

Marton, G., and Buffler, R. T. , 1994, Jurassic reconstruction of the Gulf of Mexico Basin, Int. Geol. Rev., 36, p. 545-586.

Meyer, B., Saltus, R., and Chulliat, A., 2017, EMAG2: Earth Magnetic Anomaly Grid (2-arc-minute resolution) Version 3, National Centers for Environmental Information, NOAA. Model. Doi: 10.7289/V5H70CVX.

Mickus, K., Stern, R.J., Keller, G.R., and Anthony, E.Y., 2009, Potential field evidence for a volcanic rifted margin along the Texas Gulf Coast, Geology, v. 37, p. 387-390.

Mittelstaedt, E., Ito, G., Behn, M.D., 2008, Mid-ocean ridge jump associated with hotspot magnatism, Earth and Planetary Science Letters, p. 256-270.

Murad I., 2014, Tectonostratigraphic Stages in the Mesozoic Opening and Subsidence of the Gulf of Mexico Based on Deep-Penetration Seismic Reflection Data in the Salt-Free Eastern Part of the Basin, [MS thesis], The University of Houston.

Nguyen, L. C. and Mann, P., 2016, Gravity and magnetic constraints on the Jurassic opening of the oceanic Gulf of Mexico and the location and tectonic history of the Western Main transform fault along the eastern continental margin of Mexico, *Interpretation*, Vol. 4, No. 1, SC23-SC33.

Nwafor, 2013, Crustal structure of the eastern Gulf of Mexico, [Master thesis], The University of Alabama.

O'Reilly, C., Keay, J., Birch-Hawlims, A., Bate, D., and Halliday, J., 2017, Regional Play Types in the Mexican Offshore, Geoexpro, V. 14, No. 4.

Pascoe, R., Nuttall, P., Dunbar, D., Bird, D., 2016, Constraints on the timing of continental rifting and oceanic spreading for the Mesozoic Gulf of Mexico basin, Mesozoic of the Gulf Rim and Beyond: New Progress in Science and Exploration of the Gulf of Mexico Basin, 35TH Annual Gulf Coast Section SEPM Foundation Perkins-Rosen Research Conference, p. 81-122.

Padilla-Sanchez, R. J., 2017, The Late Triassic-Late Cretaceous Flooding of the Gulf of Mexico from the Pacific through Mexico, AAPG Annual Convention and Exhibition, Houston, Texas.

Pearson, O. N., 2011, Undiscovered hydrocarbon resources in the U.S. Gulf Coast Jurassic Norphlet and Smackover Formations. Gulf Coast Association of Geological Societies Transactions 61, p. 329-340.

Pilger, R. H., 1981, The Opening of the Gulf of Mexico: Implications for the Tectonic evolution of the Northern Gulf Coast, Transactions-Gulf Coast Association of Geological Societies, V.XXXI.

Pindell, J., 1985, Alleghenian reconstruction and subsequent evolution of the Gulf of Mexico, Bahamas, and Proto-Caribbean, Tectonics, vol. 4, No. 1, p. 1-39.

Pindell, J. L. and Keenan, L., 2009, Tectonic evolution of the Gulf of Mexico, Caribbean and northern South America in the mantle reference frame; an update, *Geological Society of London*, Vol. 328, p. 1-55.

Pindell, J., Ernesto, M.C. , Alejandro, C. , Leopoldo, H. , 2016, Aeromagnetic Map Constrains Jurassic-Early Cretaceous Synrift, Break Up, and Rotational Seafloor Spreading History in the Gulf of Mexico, Mesozoic of the Gulf Rim and Beyond: New Progress in Science and Exploration of the Gulf of Mexico Basin, V. 35.

Rea, D. K., 1976, Analysis of a fast spreading rise crest: The East Pacific Rise, 9° to 12° South, Marine Geophysical Researches 2, p. 291-313.

Rea, D. K., 1977, Local axial migration and spreading rate variations, East Pacific Rise, 31°S, Earth and Planetary Science Letters, Vol. 34, Issue 1, p. 78-84.

Reid, I., Jackson, H.R. , 1981, Oceanic spreading rate and crustal thickness, Marine Geophysical Research, No. 5, p. 165-172.

Rodriguez, A. B., 2011, Reginal structure, stratigraphy, and hydrocarbon potential of the Mexican sector of the Gulf of Mexico, [MS Thesis], University of Texas at Austin.

Salvador, A., 1987, Late Triassic-Jurassic paleogeography, and origin of Gulf of Mexico Basin: AAPG Bulletin, v. 71, p. 419-451.

Salvador, A., 1991, Triassic-Jurassic, in Salvador, A., ed., The Gulf of Mexico Basin: Boulder, Colorado, Geological Society of America, Geology of North America, v. J, p. 131-180.

Sandwell, D. T., Muller, R. D. , Smith, W. H. F. , Garcia, E. , Francis, R. , 2014, New global marine gravity model from CryoSat-2 and Jason-1 reveals buried tectonic structure, *Science*, Vol. 346, p. 65-67.

Saunders, M., Geiger, L., Rodriguez, K., and Hargreaves, P., 2016, The Delineation of Pre-Salt License Blocks in the Deep Offshore Campeche-Yucatan Basin, AAPG presentation.

Schnetzler, C.C., 1985, An Estimation of Continental Crust Magnetization and Susceptibility From Magsat Data for the Conterminous United States, Journal of Geophysical Research, V. 90, N. B3, 2617-2620.

Sharma, P. V., 1997, Environmental and Engineering Geophysics. Cambridge University Press, Cambridge, p. 1-475, http://dx.doi.org/10.1017/CBO9781139171168.002.

Smith, W. H. F., and Sandwell, D. T., 1997, Global seafloor topography from satellite altimetry and ship depth soundings, Science, v. 277, p. 1957-1962.

Snedden, J. W., Norton, I. O. , Christeson, G.L. , and Sanford, J.C., 2014, Interacting of Deepwater Deposition and a Mid-Ocean Spreading Center, Eastern Gulf of Mexico Basin, USA, Gulf Coast Association of Geological Societies Transactions, V. 64, 371-383.

Scrreejith, K. M., Chaubey, A. K., Mishra, A. , Kumar, S. , and Rajawat, A.S. , 2016, Pseudofaults and associated seamounts in the conjugate Arabian and Eastern Somali basins, NW Indian Ocean-New constraints from high-resolution satellite-derived gravity data, Journal of Asian Earth Sciences.

Steier, A., 2018, Jurassic-Cretaceous stratigraphic and structural evolution of the northern Yucatan margin, Gulf of Mexico basin, [MS thesis], The University of Houston.

Stern, R. J. and Dickinson, W. R., 2010, The Gulf of Mexico is a Jurassic backarc basin, Geosphere, Vol.6, No. 6, doi: 10.1130/GES00585, p. 739-754.

USGS search earthquake catalog: https://earthquake.usgs.gov/earthquakes/search/.

Van Avendonk, H., V., Lawver, L., and Norton, I, 2011, Kinematic reconstruction of the central US and conjugate northwest African margin, EarthScope-GeoPRISMS, Science Workshop for Eastern North America, available at (http://citeseerx.ist.psu.edu/viewdoc/download;jsessionid=29265751DB7815CD6B8F3718C847AB20?doi=10.1.1.712.7815&rep=rep1&type=pdf)

Van Avendonk, H. J.A., Christeson, G. L. , Norton, I. O. , and Eddy, D. R. , 2015, Continental rifting and sediment infill in the northwestern Gulf of Mexico: Geology, 43, p. 631-634, doi: 10.1130/G36798.1.

Warwick, P., 2017, Geologic Assessment of Undiscovered Conventional Oil and Gas Resources in The Lower Paleogene Midway and Wilcox Groups, and the Carrizo Sand of the Claiborne Group, of the Northern Gulf Coast Region, USGS open file report, https://pubs.usgs.gov/of/2017/1111/ofr20171111.pdf

Weatherall et al., 2015, A New Digital Bathymetric Model of the World's Oceans, Earth and Space Science, vol. 2, no. 8, p. 331–345.

Whaley, J., 2006, Huge Potential Still Waiting in the Gulf of Mexico, Geoexpro, Vol.3. No.4.

Williams-Rojas et al., 2012, Hydrocarbon Potential of the Deepwater Portion of the "Salina del Istmo" Province, Southeastern Gulf of Mexico, Mexico, p. 641-644.

Wilson L. Kevin, 2011, The Origin and Development of the Tampa Embayment Implications for the Tectonic Evolution of the Eastern Gulf of Mexico, [MS thesis], The University of Alabama.